Structural and Electronic Characterization of Single Crystals of Ambipolar Organic Semiconductors: Diindenoperylene and Diphenylanthracene

Von der Fakultät Mathematik und Physik der Universität Stuttgart zur Erlangung der Würde eines Doktors der Naturwissenschaften (Dr. rer. nat.) genehmigte Abhandlung

Vorgelegt von

Ashutosh Kumar Tripathi

aus Mirzapur, Indien

Hauptberichter:	Prof. Dr. J. Wrachtrup
Mitberichter:	Prof. Dr. H. Dosch
Tag der mündlichen Prüfung:	30.05.2008

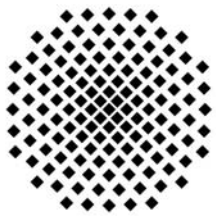

3. Physikalisches Institut der Universität Stuttgart

Table of contents

List of abbreviations

DIP	Diindenoperylene
DPA	Diphenylanthracene
DSC	Differential Scanning Calorimetry
FET	Field Effect Transistor
FWHM	Full-Width-At-Half-Maxima
HOMO	Highest Occupied Molecular Orbital
IR	Infra Red
LUMO	Lowest Unoccupied Molecular Orbital
MOSFET	Metal-Oxide-Semiconductor Field Effect Transistor
OFET	Organic Field Effect Transistor
OLED	Organic Light Emitting Diode
OMC	Organic Molecular Crystal
OPV	Organic Photovoltaic
OPVC	Organic Photovoltaic Cell
OSC	Organic Solar Cell
OTFT	Organic Thin Film Transistor
PAH	Polycyclic Aromatic Hydrocarbon
PEDT:PSS	Poly(3,4-ethylenedioxythiophene)/poly(styrenesulfonate)
PMT	Photo Multiplier Tube
RFID	Radio Frequency Identification
SCLC	Space Charge Limited Current
TOF	Time-Of-Flight
UV-Vis	Ultra Violet-Visible

Zusammenfassung

Organische halbleitende Materialien stehen gegenwärtig im Mittelpunkt zahlreicher Studien der modernen Festkörperphysik. Neben ihren vielseitigen Einsatzmöglichkeiten in flexiblen Dünnschichtbauteilen, wie z.B. Leuchtdioden, werden die experimentellen und theoretischen Untersuchungen durch Fragen nach den zugrundeliegenden Transportmechanismen motiviert. Hierbei zeigt sich, dass konkurrierenden Prozesse, wie der elektronische Überlapp und die Elektron-Phonon-Wechselwirkung, auf vergleichbaren energetischen Skalen auftreten und die van-der-Waals gebundenen polyaromatischen Kohlenwasserstoffe somit eine hochkomplexe Materialklassse definieren. Infolge der z.T. erheblichen chemischen Instabilität sowie der großen Energielücke der polyaromatischen Kohlenwasserstoffe ist es notwendig, hoch-reine, einkristalline Referenzsysteme für das Studium der intrinsischen Transportparameter, sowie der extrinsischen Effekte, mit einzubeziehen.

Dieser Aufgabe widmet sich die vorliegende Arbeit, die am Beispiel zweier ausgewählter Verbindungen die elektronischen Eigenschaften vor dem Hintergrund der jeweiligen strukturellen Merkmale der entsprechenden kristallinen Proben analysiert. Dazu wurden mittels Sublimations- und Bridgman-Zucht Einkristalle aus den organischen Halbleitermaterialien Diindenoperylene (DIP) und 9,10-Diphenylanthrazen (DPA) hergestellt. Motivation für die Wahl dieser beiden polyaromatischen Kohlenwasserstoffe war deren chemische Stabilität gegenüber Photo-Oxidation sowie die thermische Robustheit, welche die Abscheidung aus der Gasphase ermöglicht. Die einkristallinen Proben konnten mit lateralen Abmessungen von einigen Millimetern präpariert werden und erlaubten so ihre strukturelle und elektronische Charakterisierung. Hierbei wurde zum ersten Mal eine vollständige Strukturbestimmung dieser Einkristallsysteme mit Hilfe temperaturabhängiger Röntgenmethoden vorgenommen. Verschiedene Polymorphismen wurden experimentell bestätigt und deren jeweilige Kristallstruktur bestimmt.

Um den Zusammenhang zwischen strukturellen und elektronischen Eigenschaften zu untersuchen, wurden zusätzlich temperaturabhängige Messungen mittels TOF, SCLC und FET an den einkristallinen Proben vorgenommen. Der Einfluss von Fallenzuständen,

Kristallit-Größen, Fallen an metall-organischen und Isolator-Halbleiter Grenzflächen auf die temperaturabhängige Ladungsträgerbeweglichkeit wurde im Rahmen verschiedener Transport-Modelle diskutiert.

DIP Kristalle: Enantiotropischer Polymorphismus

Für sublimationsgezüchtete DIP Kristalle konnte ein enantiotropischer Phasenübergang von einer triklinen *α-Phase* (Tieftemperaturphase) mit den Gitterparametern a = 11.58 Å, b = 12.96 Å, c = 14.88 Å, α = 98.14°, β = 98.10°, γ = 114.53°, Raumgruppe $P\bar{1}$ und einem Volumen der Einheitszelle von V = 1963.0 Å^3 zu einer monoklinen *β-Phase* (Hochtemperaturphase) mit der Einheitszellengröße a = 7.17 Å, b = 8.55 Å, c = 16.80 Å, β = 92.42°, Raumgruppe $P2_1/a$ und dem Volumen der Einheitszelle von V = 1028.9 Å^3 bei 403 K (T_c) nachgewiesen werden. Diese Hochtemperatur *β-Phase* entspricht interessanterweise der DIP Dünnschicht-Phase, welche auf schwach wechselwirkenden Substraten wie z.B. SiO_2 beobachtet wird. Die mit Hilfe der Scherrer Formel aus der Breite der Bragg-Peaks bestimmte Kristallit-Größe schwankt je nach Kristallqualität zwischen 900 Å und 2400 Å. Röntgenmessungen zeigen, dass der fest-fest Phasenübergang von einer metastabilen Zwischenphase begleitet wird, welche in die β-Phase übergeht, wenn der Phasenübergang abgeschlossen ist. Die Zwischenphase bildet sich bei etwa 370 K (T_{ph}) und definiert damit den Beginn des Phasenübergangs, der sich durch eine große Temperaturhysterese auszeichnet.

Eine weitere Beobachtung in Hinblick auf die temperaturabhängigen Transportmessungen ist die Verschiebung der Phasenübergangstemperatur für DIP Kristalle, deren Oberflächen mit metallischen Kontaktschichten aus Silber versehen sind. Gegenüber Kristallen mit freien Grenzflächen verschiebt sich bei diesen die Phasenübergangstemperatur zu höheren Werten und, wie Röntgenmessungen zeigen, ist zumindest bis zu einer Temperatur von 405 K der strukturelle Phasenübergang noch nicht vollständig abgeschlossen. Als Ursache für die Erhöhung der Phasenübergangstemperatur kommt zum Einen die starke physisorptive oder chemisorptive Wechselwirkung an der Metall-DIP Grenzfläche in Betracht, die infolge eines effektiven ‚pinnings' der oberen

Lage die molekulare Umordnung bis in tiefe Schichtbereiche hinein behindert. Hierbei dürfte das Ineinanderrasten der benachbarten DIP Lagen wesentlich zur Fixierung beitragen. Eine weitere Möglichkeit für die Verschiebung des Phasenübergangs zu höheren Temperaturen ist durch das Eindringen des Kontaktmetalls in die organischen Schichten bei erhöhten Temperaturen gegeben. Die dabei gebildeten Metall-Cluster innerhalb der organischen Schichte können die Re-Orientierung der DIP Moleküle effektiv stören.

Durch temperaturabhängige Röntgenstrukturunteranalysen können die Details der DIP Kristallstruktur und des Phasenübergangs untersucht werden. Sie zeigen, dass die Gitterparameter, Schwingungen und Translations-Bewegungen eine Unstetigkeit bei T_c aufweisen und dass der enantiotropische Phasenübergang dementsprechend erster Ordnung ist. Beim Phasenübergang von der niedrig-symmetrischen triklinen α-Phase zur höher-symmetrischen monoklinen *β-Phase* halbiert sich die Größe der Einheitszelle. Zusätzlich treten starke Scherkräfte innerhalb des Kristallgitters auf, die Spannungsfelder hervorrufen und oft zum Zerbrechen des Kristalls während der temperaturabhängigen Messungen führen.

Die Enthalpie des Phasenübergangs wurde aus Kalorimetrie-Spektren berechnet und beträgt $\Delta H = 1{,}0 \pm 0{,}2$ kJ/mol, entsprechend einer Entropieänderung von $\Delta S = 2{,}4 \pm 0{,}5$ J/(mol K). Die experimentell bestimmten Werte stimmen gut mit den theoretischen Vorhersagen von $\Delta S = 2{,}88$ J/(mol K) überein, wenn man annimmt, dass der Hauptbeitrag zur Entropieänderung durch die Symmetriebrechung hervorgerufen wird.

DPA Kristalle: Monotropische Polymorphismen

Im Falle des Materials DPA wurden Kristalle, die nach der Bridgman-Methode aus der Schmelze gezogen wurden, mit denen, die mittels Sublimation aus der Gasphase präpariert wurden, strukturell verglichen. Als zentrale Beobachtung konnten wir feststellen, dass die Kristallstruktur signifikant von der Wachstumsmethode abhängt. Bridgman-gezüchtete Kristalle zeigen eine monokline Struktur mit den Gitterparametern $a = 10{,}7$ Å, $b = 13{,}6$ Å, $c = 12{,}3$ Å, $\beta = 90{,}5$ °. Diese stimmen mit den charakteristischen Größen überein, die für DPA-Kristalle aus der Lösungszucht gemessen wurden. Sublimationsgezüchtete DPA-Kristalle weisen jedoch eine völlig andere Anordnung der

Moleküle in der Einheitszelle auf und bilden eine monokline Kristall-Struktur mit den Gitter- bzw. Winkelparametern a = 9,5 Å, b = 20,4 Å, c = 10,1 Å und β = 112,3 °. Außerdem ist das Anthrazen-Gerüst in sublimationsgezüchteten DPA-Kristallen um nahezu 90° gegenüber dem in Bridgman-gezüchteten Proben gedreht. Dieser fundamentale Unterschied in den jeweiligen molekularen Anordnungen legt den Schluss nahe, dass DPA in zwei monotropen Polymorphismen vorkommt, die nicht durch Heizen oder Kühlen ineinander überführt werden können. Röntgenmessungen an den Kristallen haben zudem gezeigt, dass sublimationsgezüchtete Kristalle eine deutlich bessere strukturelle Kohärenz im Vergleich zu den Bridgman-Kristallen besitzen. Die Kristallit-Größe der Sublimationskristalle wurde zu ca. 1600 Å bestimmt, wohingegen die Bridgman-Kristalle eine Kristallitgröße von etwa 900 Å aufweisen. Die Tendenz einer höheren strukturellen Qualität von DPA Sublimationskristallen zeigt sich auch in den durchgeführten Messungen der Rocking-Breiten, die eine geringere mittlere Verkippung der Kristallite ergaben als im Fall der Bridgman-gewachsenen Kristalle.

Elektronischer Transport in DIP Kristallen

Sowohl Elektronen- als auch Löchertransport kann in DIP Einkristallen aufgrund der chemischen Stabilität der DIP Moleküle mit der Time-Of-Flight Methode beobachtet werden. Die Elektronen-Beweglichkeit bei Raumtemperatur beträgt ca. 0,02 cm²/Vs und die Löcher-Beweglichkeit ca. 0,003 cm²/Vs. Die Elektronen-Beweglichkeit ist im gemessenen Temperaturbereich stets höher als die Loch-Beweglichkeit. Dies lässt auf eine unterschiedliche Ankopplung der jeweiligen Ladungsträgerart an die phononischen Anregungen schließen bzw. auf unterschiedliche Empfindlichkeiten gegenüber den auftretenden Fallenzuständen und Einfangmechanismen für Elektronen und Löcher.
In Hinblick auf die Korrelation der elektronischen mit den strukturellen Eigenschaften zeigen beide, Elektronen- und Loch-Beweglichkeit, Abweichungen vom erwarteten thermischen Transportverhalten bei Einsetzen des Phasenübergangs bei 370 K. Temperaturabhängige TOF-Messungen ergeben für die Loch-Beweglichkeit ein thermisch aktiviertes Verhalten mit einer Aktivierungs-Energie von Ea = 230 ± 20 meV,

wobei diese vermutlich auf Potentialbarrieren infolge des Bruchs der Translationssymmetrie an den Korngrenzen zurückzuführen ist.

Temperaturabhängige SCLC und FET Messungen wurden von 300 K bis 450 K durchgeführt. Aufgrund der hohen Injektionsbarriere für Elektronen an der Ag-DIP Grenzfläche konnte mit beiden Methoden ausschließlich Löchertransport beobachtet werden. Ähnlich wie die TOF Messungen zeigen auch die temperaturabhängigen SCLC und FET-Messungen Abweichungen vom regulären Beweglichkeitsverhalten bei etwa 370 K. Dies deutet auf eine starke Beeinflussung der elektronischen Transporteigenschaften durch den strukturellen Phasenübergang hin, wobei die FET Beweglichkeit in der *(ab)*-Ebene deutlich stärker beeinflusst wird als die Beweglichkeit orthogonal dazu (entlang der *c'*-Richtung). Vermutlich ist hierfür die spezielle Packung (Fischgräten-Struktur) der DIP Moleküle in der *(ab)*-Ebene verantwortlich. Diese ergibt zwar einen größeren Überlapp der am Transport beteiligten Molekülorbitale, erfährt aber andererseits mit zunehmender thermischer Energie auch stärkere Fluktuationen bzw. Störungen. Die FET Beweglichkeit in der *(ab)*-Ebene bei Raumtemperatur ist mit 2×10^{-4} cm^2/Vs beinahe eine Größenordnung höher als die dazu senkrecht orientierte SCLC Beweglichkeit.

Die SCLC Beweglichkeit zeigt thermisch aktivierten Transport, allerdings mit zwei unterschiedlichen Aktivierungsenergien in verschiedenen Temperaturbereichen. Im Bereich von 300-360 K wurde eine Aktivierungsenergie von 820 ± 80 meV gemessen, wohingegen die Aktivierungsenergie für Temperaturen über 360 K auf 120 ± 20 meV sinkt.

Die beiden verschiedenen Aktivierungsenergien lassen auf Fallenzustände an der metall-organische Grenzfläche schließen, die im niedrigeren Temperaturbereich dominieren. Allerdings sinkt deren Einfluss, wahrscheinlich aufgrund von irreversiblen Tempereffekten bei höheren Temperaturen.

Entsprechend der gleichen strukturellen Phase ist die FET Lochbeweglichkeit in den DIP Einkristallen bei Temperaturen über 405 K vergleichbar mit der in DIP Dünnfilm-Transistoren auf SiO_2.

Bandähnlicher, ambipolarer Transport in DPA Kristallen

Die nach der Bridgman-Methode hergestellten DPA-Kristalle zeigen TOF Loch-Beweglichkeiten über den gesamten Temperaturbereich von 5 K – 405 K. Allerdings waren TOF Signale von Elektronen für den Großteil des gemessenen Temperaturbereichs, vermutlich aufgrund von tiefen Fallenzuständen, die durch Oxidationsprodukte wie z.B. Diphenylanthrazen-endoperoxid hervorgerufen wurden, nicht eindeutig nachweisbar. Die TOF-Beweglichkeiten bei Raumtemperatur erreichen hohe Werte für Löcher von ~ 3,8 cm²/Vs und für Elektronen von ~ 13 cm²/Vs. Die temperaturabhängige Loch-Beweglichkeit zeigt ein bandähnliches Transportverhalten im Temperaturbereich von 100 K bis 420 K mit einer Abhängigkeit von $\mu(T) \sim T^{-2,3}$, welches vorrangig auf die Streuung an akustischen und optischen Phononen hindeutet. Unterhalb von 100 K nimmt die Lochbeweglichkeit einen nahezu temperaturunabhängigen Wert von ~ 10 cm^2/Vs an. Die im Rahmen eines tight-binding Bandmodells durchgeführte Abschätzung der Dispersion aus dem Sättigungsbereich der TOF Lochbeweglichkeit resultiert in einer Valenzbandbreite von ~ 2 meV. Die entsprechende thermische Energie bei 100 K übersteigt diese Bandbreite aber deutlich und zeigt die Notwendigkeit eines differenzierteren theoretischen Ansatzes, der z.B. auch den Einfluss energetisch tiefliegender (kohärenter) Vibrationsmoden der Moleküle mitberücksichtigt.

In sublimationsgezüchteten DPA-Kristallen lässt sich sowohl die Löcher- als auch die Elektronen-Beweglichkeit im Temperaturbereich von 300 K – 440 K bestimmen. Die Beweglichkeit bei Raumtemperatur beträgt 6,6 cm²/Vs für Löcher und 4,8 cm²/Vs für Elektronen. Sowohl Elektronen als auch Löcher zeigen einen bandähnlichen Transport mit präferentieller Streuung an akustischen Phononen entsprechend einer Temperaturabhängigkeit von $\mu(T) \sim T^{-1,5}$. Der balancierte Elektronen- und Löchertransport mit hohen Ladungsträgerbeweglichkeiten in sublimationsgezüchteten DPA Kristallen zeigt das Potential dieses Materials für die Anwendung in organischen, ambipolaren Bauelementen. Die Löcherbeweglichkeit, die aus den *I-V* Messungen berechnet wurde, ist allerdings fünf Größenordnungen niedriger als die TOF Beweglichkeit. Daraus kann geschlossen werden, dass die standardmäßig verwendeten

Metallelektroden aus Ag nicht für eine Lochinjektion in DPA geeignet sind. Elektroden aus leitenden Polymeren wie PEDOT:PSS könnten, aufgrund des geringeren Unterschiedes zwischen dem DPA HOMO-Niveau von ~5,8 eV und der Austrittsarbeit des Polymers von ~ 5,7 eV, gegenüber Ag oder Au eine Verbesserung des Injektionsverhaltens ergeben.

Ausblick

Sowohl DIP als auch DPA zeigen ambipolaren Transport mit ausgeglichenen Löcher- und Elektronenbeweglichkeiten bei der injektionsfreien TOF-Messung, was die Möglichkeit diese Materialien für Anwendungen in ampipolaren Bauelementen einzusetzen aufzeigt. Vor allem DPA ist aufgrund des ampipolaren Transports mit hohen Elektronen- und Löcherbeweglichkeiten, sogar bei Raumtemperatur, ein sehr interessantes Material.

Die Ladungsträgerinjektion in DPA bleibt jedoch bis jetzt ein Problem für die Realisierung von FETs auf Basis dieses Materials. Für eine mögliche Anwendung müssen noch weitere Änderungen an den Eigenschaften der metall-organischen Grenzfläche vorgenommen werden, wie z.B. die Verwendung von leitenden Polymeren oder funktionalisierten Metallelektroden, um die Injektionsbarriere zu senken.

Eine optische Charakterisierung von DPA Kristallen, z.B. mit Raman-Spektroskopie oder Ellipsometrie, würde, zusammen mit den elektronischen Transporteigenschaften, die in dieser Arbeit präsentiert wurden, helfen, weitere mikroskopische Mechanismen des Ladungsträgertransports besser zu verstehen und würde ebenfalls Erkenntnisse liefern, die helfen könnten, die Injektions- und Transporteigenschaften dieser Kristalle zu verbessern.

1 Introduction

Organic semiconductors have been a field of intense research interest over the past several decades due to their unique mechanical and opto-electronic properties. For example, substituting the hydrogen atoms attached to the conjugated π-system with various organic and inorganic substituents can delicately modify the opto-electronic properties of organic semiconductors. This chemical tunability provides enormous opportunities to optimize desired optical and electronic properties of the organic molecules.

Their ability to form semiconducting layers on flexible substrates enables realization of flexible organic electronic devices. Indeed, various organic electronic devices such as Organic Light Emitting Diodes (OLEDs), Radio-Frequency Identification (RFID) tags etc. have been successfully fabricated. Few commercial products such as mobile phones with OLED based displays etc. are already present in the market.

However, all organic devices, e.g. optoelectronic organic devices driven by organic field effect transistors (OFETs), have not yet been realized because of the limited performance, mainly due to subdued electronic transport properties of the active organic layers. Even the best charge carrier mobilities observed in organic thin film transistors (OTFT) are several orders of magnitudes lower than those observed in conventional inorganic semiconductor based electronic devices, e.g. ~10^3 cm^2/Vs for polycrystalline silicon [1] compared to ~1 cm^2/Vs for typical organic thin film transistors [2,3]. Low charge carrier mobility in organic semiconductors is mainly due to the weak intermolecular overlap in the van-der-Waals bonded molecules compared to covalently bond inorganic semiconductors.

Although researchers around the globe have been successful in fabricating organic electronic devices such as RFID, OLED, complementary circuits etc. [4,5,6], the underlying transport mechanisms of charge carriers are still poorly understood due to the various extrinsic constraints imposed by photo-oxidation [7,8], limitations due to the structural order [9], complex injection phenomena at metal-organic interfaces [10,11] etc.

Therefore, investigations on samples showing best structural order as well as chemical and thermal stability are necessary to analyze the microscopic transport mechanisms in organic semiconductors.

Chronological development in organic electronics

The history of organic semiconductors dates back to early 20th century related to the work of Pocchettino in 1906 who observed the photoconduction in anthracene crystals [12]. Further developments resulted in the observation of dark conductivity in anthracene by Königsberger and Schilling (1910) [13]. In 1913 Vollmer demonstrated a prototype of photovoltaic cell based on organic materials [14].

Around 1960 research in the field of organic semiconductors based on organic molecules as well as on polymers was carried forward by Pope and other scientists who laid the foundation of modern organic electronics [15,16,17]. In 1964 the first field-effect measurements for holes were performed on α-CuPc organic films [18] and in 1970 field-effect for electrons was reported on organic crystals of chloranil [19]. McGinness reported the first organic electronic device, a semiconductor switch based on melanin, in 1974 [20]. In 1977 Heeger, MacDiarmid and Shirakawa reported a path breaking work in which they discovered the high conductivity in oxidized, iodine-doped polyacetylene [21] and they received the Nobel Prize in chemistry in the year of 2003 for this contribution.

Since then, the developments in the field of organic semiconductors have taken up pace and various device applications such as OTFTs [22,23], complementary circuits [24], OFET driven active matrix OLED displays [25,26], organic photovoltaic cells (OPVCs) [27] etc. have been reported and certain products have been launched in the market.

Need of investigation of Organic Molecular Crystals (OMCs)

Organic thin film devices do not provide a good reference system for the microscopic level investigation of charge carrier transport because of various reasons, e.g. limited structural quality, and complex interface phenomena at metal-organic interfaces etc.

Therefore, in order to get an insight in the underlying transport mechanisms, investigation of electronic transport in organic molecular crystals (OMCs) is mandatory. It has been shown in the past that electronic transport properties strongly depend on structural order [28]. Crystals, due to their excellent structural quality compared to the respective thin films, provide good reference system and a benchmark for the performance of organic thin film based devices. So far, the highest mobility in organic semiconductors has been reported on single crystals of naphthalene which amounts to ~ 400 cm^2/Vs for holes at 10 K [29], which in fact is comparable to the electron mobilities in silicon Metal-Oxide-Semiconductor-FET (MOSFET) at room temperature. The room temperature mobilities of charge carriers in some ultra-pure organic crystals of polycyclic aromatic hydrocarbons (PAHs) lie in the order of ~ 1 – 10 cm^2/Vs [30] and already exceeds charge carrier mobilities in microcrystalline silicon (e.g. ~ 1 cm^2/Vs at RT) [31]. Another advantage of OMCs is that the effect of spatial anisotropy on electronic and optical properties can be studied in detail as these crystals provide the possibility to perform measurements along different crystallographic directions, which is almost impossible on organic thin films. Mobility tensors for several organic crystals such as anthracene [32], perylene [33] etc. have been reported and show strong anisotropy in the electronic properties along different crystallographic directions.

OFETs based on rubrene single crystals show room temperature hole mobilities of ~ 20 cm^2/Vs on their surfaces [34] and OFETs based on pentacene crystals exhibit surface hole mobilities as high as 35 cm^2/Vs at room temperature [35]. These mobility values reported on organic single crystals are one order of magnitude higher than the best mobilites reported on OTFTs [22,23]. Besides improved mobility values, the effect of anisotropy on the surface mobility has been studied in rubrene single crystals by FET method, which differs by almost a factor of four along different crystallographic directions ($\mu_{h,b}(RT) \cong 4\times\mu_{h,a}(RT)$) [36]. Temperature dependent mobility measurements on various organic crystals give information about the relevant transport phenomena and therefore temperature dependent electronic characterization of OMCs of good structural order and high purity is an important step to understand the charge conduction mechanisms and to systematically improve the performance of organic thin film based devices.

Goal and objective of the present research

Motivated by the excellent electronic and structural properties exhibited by the various OMCs, we have carried forward the research on the transport phenomena in single crystals of PAHs. Although very high mobilities have been reported already on single crystals of naphthalene [29] and durene [37], these materials cannot be used for practical purpose in organic electronics device fabrication due to their high vapor pressure and inability to form stable thin films.

On the other hand, crystals of rubrene and pentacene exhibit high hole mobilities on the surface and are thermally stable, yet their tendency to photo-oxidize suppresses the transport of electrons due to the formation of trap states related to oxidation products [38,39]. Photo-oxidation in organic compounds is supposed to be a big obstacle to achieve balanced ambipolar transport, i.e. good electronic transport of both electrons and holes of similar quality.

Therefore, in order to realize ambipolar organic electronics we need to find organic semiconductor compounds that are chemically and thermally stable and exhibit both electron and hole transport. The focus in this thesis will be on the investigation of OMCs of Diindenoperylene (DIP) and Diphenylanthracene (DPA), both showing low affinity for photo-oxidation and hence are supposed to exhibit ambipolar transport.

Outline of the thesis

The structure of this thesis is organized as following:

In Chapter 2 we shall introduce the semiconductor properties of conjugated organic compounds in general followed by the discussion on the conduction in PAHs. The theoretical background relevant to the experimental work performed in this thesis shall be presented and special focus will be given to the charge carrier mobility in weakly bonded OMCs. Temperature dependence of mobility provides useful information about conduction mechanisms in these materials and it will be discussed in the framework of various theoretical models, i.e. band-like transport or hopping transport. Microscopic

phenomena such as electron-phonon coupling, scattering of charge carriers by acoustic and optical phonons, etc. shall be discussed.

Purification is one of the most important steps in order to observe the intrinsic transport behavior. In Chapter 3 we will describe the techniques, sublimation and zone refinement, used to purify DIP and DPA prior to crystal growth. Further, we will discuss the techniques used for the growth of these crystals.

Chapter 4 reports on experimental methods used for structural and electronic characterization of the organic crystals of DIP and DPA.

In Chapter 5 we shall present temperature dependent Bragg diffraction and single crystal X-ray diffractometry measurements together with the quantitative analysis of thermal behavior of DIP crystals. Complementary Differential Scanning Calorimetry (DSC) measurements are performed in order to analyze the thermodynamic behavior.

In Chapter 6 we have investigated the electronic transport properties of DIP single crystals. Temperature dependent electron and hole mobilities are estimated by the Time-Of-Flight (TOF) method along the *c'*-direction in DIP single crystals. Experimental data will be analyzed in the framework of different electronic transport models and will be correlated with the structural changes occurring. Finally, a comparative study of bulk and surface transport in DIP single crystals will be presented by using Space-Charge-Limited-Current (SCLC) and Field-Effect-Transistor (FET) measurements.

In Chapter 7 electronic and structural characterizations of DPA crystals grown by sublimation as well as by Bridgman method are presented. TOF measurements are performed over a broad temperature range of 5 K – 420 K on Bridgman grown DPA crystals in order to understand the occurring transport mechanisms. The observed ambipolar transport will be discussed in the framework of various (transport) models and will be correlated to the crystal structure. Finally, injection properties in sublimation grown DPA crystals are studied by Current-Voltage (*I-V*) measurements.

Important results achieved in the PhD work are summarized in the Chapter 8 followed by an outlook.

2 Transport Properties of Organic Semiconductors

In this chapter we shall briefly cover the important aspects of charge carrier transport in organic semiconductors. Transport mechanisms in organic semiconductors are non-trivial phenomena, which still have not been very well understood. There are different theoretical models, which have been used to explain the charge transport in different molecular systems, yet a universally accepted concept is still lacking. We shall start from the basic conduction mechanisms in conjugated organic materials, especially in PAHs.
In later sections, we will introduce the concept of charge carrier mobility and provide a theoretical background for the temperature dependent mobility behavior in OMCs in the framework of band-like transport as well as hopping transport models. Effects of narrow bandwidth, polaron formation, electron-phonon coupling, etc. on the charge carrier mobility will be discussed.

2.1 Conduction in molecules with a conjugated π-system

Electrons in carbon atoms in conjugated molecules, i.e. molecules with alternate single and double bonds, are described by sp^2 hybrid orbitals which constitute three covalent σ-bonds. The remaining unpaired electron occupies the p_z-orbital perpendicular to the sp^2 hybrid orbital plane and is referred to as π-electron. Due to the conjugation, these π-electrons are delocalized over the entire molecule as the adjacent p_z-orbitals overlap with each other. As a result, a cloud of delocalized π-electrons situated above and below the molecular plane is obtained due to the shape of p_z-orbitals. Such conjugated organic compounds are known as organic (wide bang-gap) semiconductors.
Figure 2.1 shows the schematic of p_z-orbital overlap in benzene. Delocalization of the π-electrons over the benzene ring results in improved conduction properties in conjugated systems compared to their aliphatic counterparts [40].

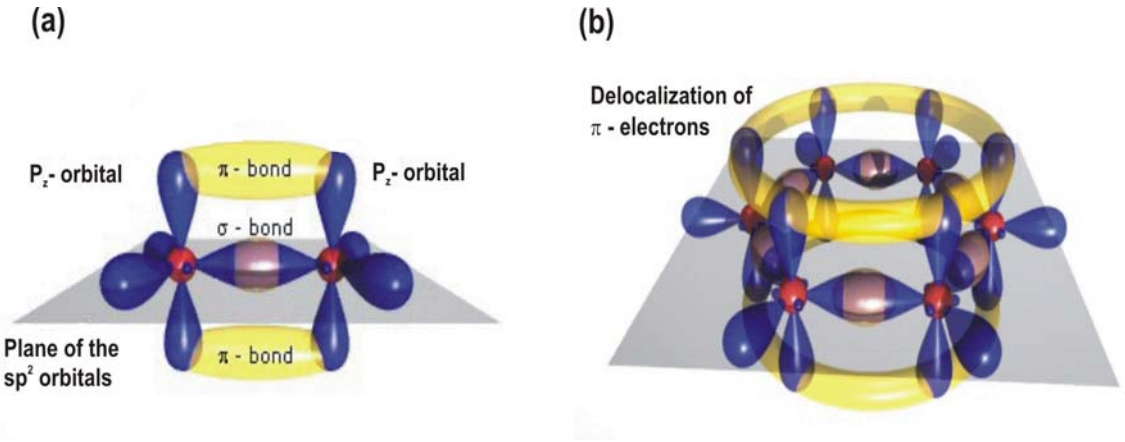

Figure 2.1 *Illustration of p_z orbital overlapping in benzene molecule [41].*

Organic semiconductors can be further divided on the basis of their molecular weight, into polymers with much higher molecular weight (e.g. > 1000) and conjugated small molecules [42]. Polymeric organic semiconductors consist of aliphatic conjugated carbon atoms in which the π-electrons are delocalized along the length of the chain and the transport properties of such semiconductors mainly depend on the chain length and the inter-chain transfer of charge carriers. Polymeric organic semiconductors are easy to process and have been widely used in organic electronics applications, e.g. OLEDs, OPVCs. However, due to the poor structural order of polymers and hence their poor electronic transport properties, many researchers have focused on small molecule organic semiconductors.

An obvious advantage of small molecule organic semiconductors is their tendency to form well ordered thin films and crystals that lead to improved electronic transport properties compared to polymers. Small molecule organic semiconductors may further be classified as linear (e.g. anthracene, tetracene, pentacene etc.), planar or three dimensional (e.g diindenoperylene, rubrene, diphenylanthracene, metal-pthalocyanine etc.) fused ring compounds, and heterocyclic oligomers (e.g. thiophene derivatives).

2.2 Polycyclic aromatic hydrocarbons (PAHs)

PAHs consist of fused aromatic rings. Aromaticity, i.e. conjugated rings of unsaturated bonds, exhibits much stronger chemical stabilization than expected from the conjugation of the neighboring carbon pairs alone. This improved stability is due to the resonance

structure and delocalization of the π-electrons, which reduces the susceptibility of unsaturated double bond towards oxidation and other chemical reactions. Benzene rings are the basic units of most of the PAHs. Kekulé was the first who suggested the structure of benzene as alternating single and double bonds between six carbon atoms arranged in a hexagonal shape [43]. However, the strong chemical stability and the regular hexagonal shape of benzene molecule required the need of modifying Kekulé's structure of benzene [44]. Therefore it was proposed that there are two molecular structures of benzene that are in resonance with each other, resulting in a resonance hybrid state. *Figure 2.2 (a)* shows these two molecular structures of benzene, which are in resonance with each other.

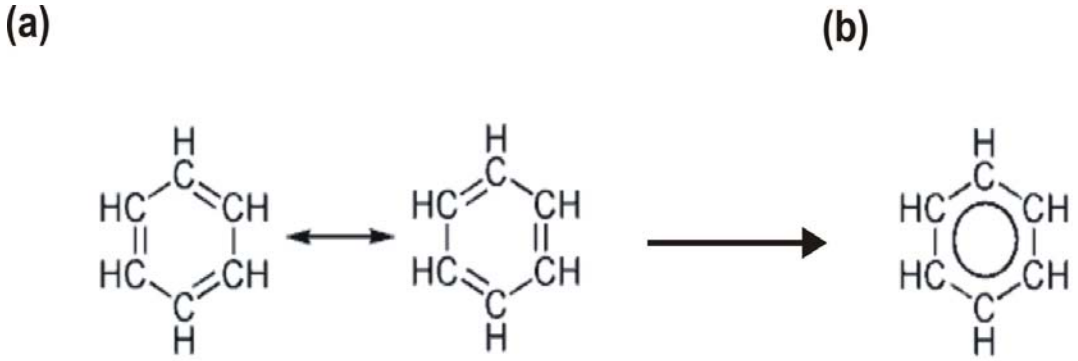

Figure 2.2 (a) *Two resonance structures of the benzene molecule.* ***(b)*** *Representation of the benzene structure indicating the delocalization of π-bonds.*

As shown in the *figure 2.2 (b)*, these two resonance structures are inseparable from each other and alternatively the electron π-bonds of benzene molecule are represented by a circular π-bond, referred to as aromatic sextet. *Figure 2.3* shows the structure of few molecular organic compounds which have been of great interest because their semiconducting properties. On the left hand side, few linear organic semiconductors are shown which have been studied in great detail due to their good transport properties (e.g. naphthalene, anthracene) and relevance in device applications (e.g. pentacene). On the right hand side, schematic representations of diindenoperylene and diphenylanthracene, which have been investigated in this thesis, are shown.

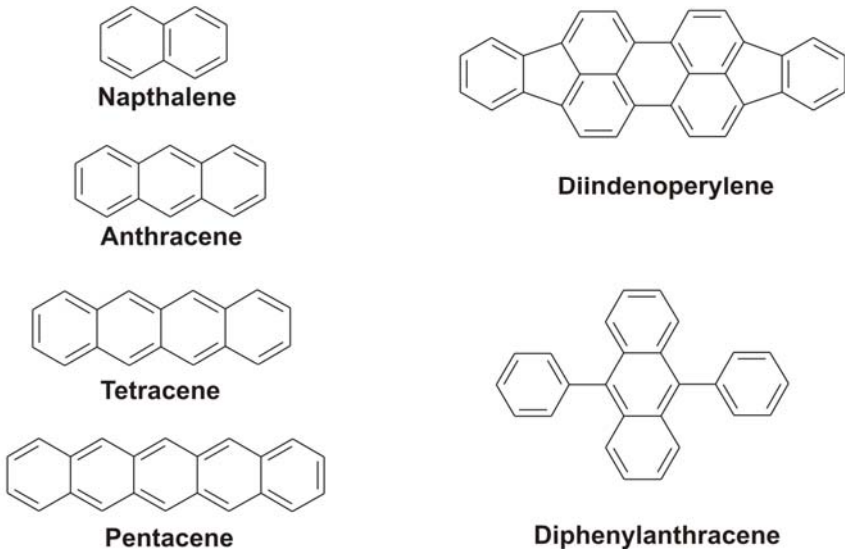

Figure 2.3 *Molecular structures of widely investigated linear PAHs : Napthalene, Anthracene, Tetracene and Pentacene (left hand side) and Diindenoperylene and Diphenylanthracene (right hand side).*

2.2.1 Degree of aromacity: Clar's sextet rule

According to the Clar's sextet rule (*E. Clar, 1961*), the number of disjoint aromatic sextets, i.e. isolated benzene rings, in a PAH is a measure for the chemical stability of the compound [45]. More the number of aromatic sextets, less vulnerable the compound is towards any chemical reaction due to the reduced availability of localized electrons.. The effect of aromaticity on chemical stability of different PAHs is demonstrated in *figure 2.4*. Triphenylene exhibits very strong chemical stability as it has three aromatic sextets without any unsaturated bonds available for chemical reaction. Coronene, on the other hand, has three aromatic sextets and three unsaturated bonds therefore it is more reactive compared to triphenylene. Reactivity of linear PAHs increases with increasing number on benzene rings as the ratio of double bonds to aromatic sextets increases and hence more reaction centers are available. Anthracene can photodimerize with radiation by UV light or it can react with oxygen in presence of UV-light to form oxidation products, e.g. anthracenequinone [46]. Tetracene is even more reactive and rapidly degrades by forming tetracenequinone and other oxidation products while exposed to mild UV light [47,7].

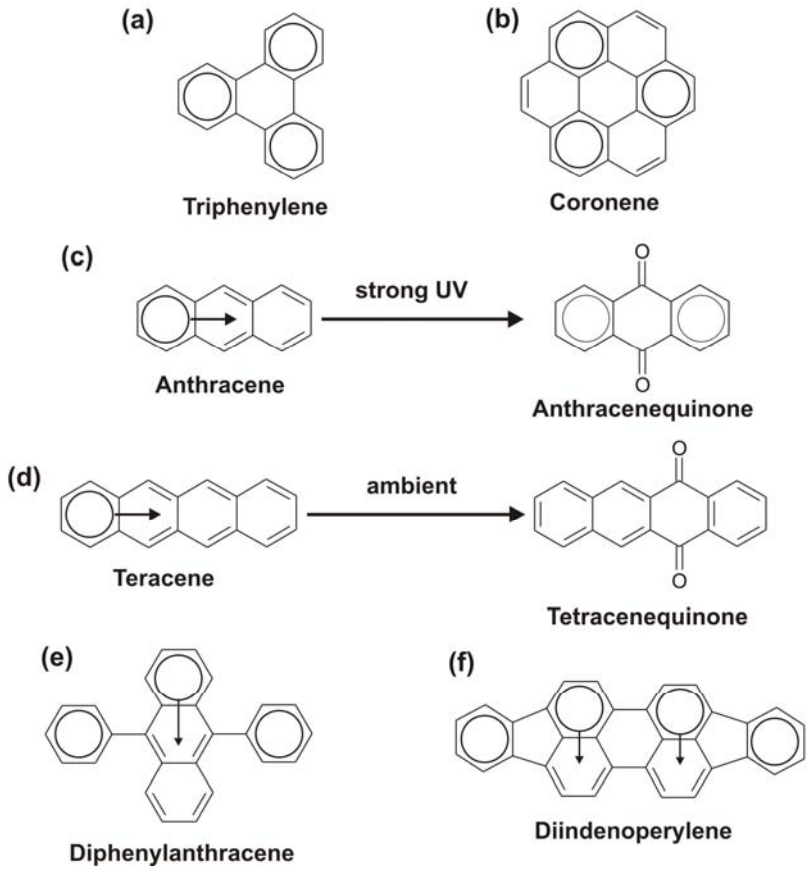

Figure 2.4 (a) *Triphenylene molecule.* ***(b)*** *Coronene with three aromatic sextets.* ***(c)*** *anthracene with one aromatic sextet oxidizes to form anthracenequinone in presence of UV.* ***(d)*** *Tetracene reacts in presence of mild UV to form tetracenequinone.* ***(e)*** *Diphenylanthracene containing three aromatic sextets is more stable compared to anthracene because of the higher substitution energy of phenyl groups compared to hydrogen atom.* ***(f)*** *Diindenoperylene forms four aromatic sextets and exhibits strong chemical stability against oxidation.*

2.3 Charge carrier mobility in organic semiconductors

Mobility is an intrinsic material property, which depends entirely on the crystal structure, transport mechanism, and the band structure. Temperature dependent charge carrier mobility provides important information about the various intrinsic properties such as electronic transport mechanism, effect of spatial anisotropy on electronic transport etc. Charge carrier mobilities can be extracted by, e.g. injection free (TOF) and injection

based (SCLC, and FET) measurement techniques. We shall discuss these techniques in detail in Chapter 4.

2.3.1 Basic concept of the mobility

When a charged particle experiences an external electric field its momentum increases with time resulting in an increase in its drift velocity. For a free particle, temporal increase of average drift velocity $\langle v_d \rangle$ under the influence of an external electric field E follows a linear relation given by

$$\langle v_d \rangle = \frac{e}{m} \tau E \qquad 2.1$$

where e is the elementary charge (1.6×10^{-19} Coulomb), and τ and m are the relaxation time and the mass of the charge carrier, respectively. The average velocity gained per unit field is termed *"mobility"* μ, given by

$$\mu = \frac{\langle v_d \rangle}{E} = \frac{e}{m} \tau \qquad . \qquad 2.2$$

However, this formulation of the mobility is valid only for free charge carriers and is inadequate to describe the mobility behavior in solids, especially organic semiconductors. The linear relation described by *equation 2.2* does not hold for either band-like transport or for hopping transport because the relaxation time τ depends on the energy of the charge carriers and the effective mass of the charge carrier depends strongly on the band structure and bandwidth within the solid. Therefore to develop a model for charge carrier mobility, understanding of the relaxation time and the effective mass is mandatory.

2.3.2 Effective mass and mobility tensor

The effective mass is defined as the mass a particle carries in a periodic potential described by a semi-classical transport model in crystals. The effective mass of a charge carrier can be described by the following equation [48]

$$\frac{1}{m_{ij}^{*}} = \frac{1}{\hbar^2}\frac{\partial^2 \varepsilon(k)}{\partial k_i \partial k_j} \quad . \qquad 2.3$$

Here $\varepsilon(k)$ is the dispersion relation, i.e. the energy as a function of the wave vector k. Therefore, in order to extract the mobility, knowledge of the band-structure along the direction of the electronic transport is necessary, which is one of the most tedious aspects of electronic transport in organic crystals.

As indicated by *equation 2.3*, the effective mass is a tensorial property. This has a very important significance for charge carrier transport, as the mobility is related to the effective mass by *equation 2.2* and therefore, shows a strong anisotropy in organic crystals.

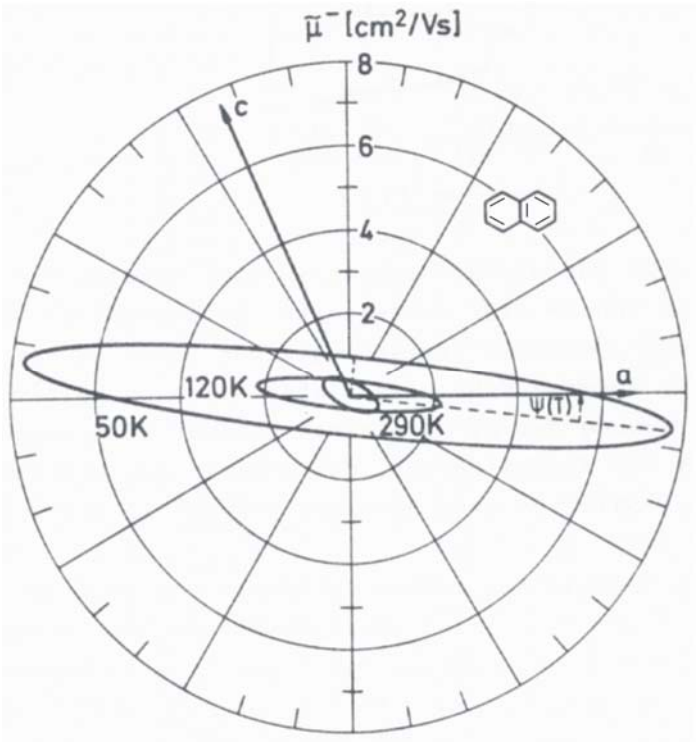

Figure 2.5 *Electron mobility as a function of temperature along different crystallographic directions in naphthalene [49].*

Figure 2.5 shows the temperature dependent electron mobility measured in ultra-pure crystals of naphthalene. The electron mobility shows a strong anisotropy with respect to

different crystallographic directions due to different molecular orbital overlapping and electron-phonon coupling along different crystallographic directions [49].
Also, the mobility tensor changes its orientation with varying temperatures, which indicates the temperature dependence of the band-structures in combination with related parameters, e.g. the anisotropic electron-phonon coupling etc.

In tensorial form, we can rewrite *equation 2.1* as

$$\underline{v}_d = \underline{\underline{\mu}}\,\underline{E} \tag{2.4}$$

where $\underline{\underline{\mu}}$ represents the mobility tensor. Assuming a Boltzmann like distribution of velocities, different components of mobility tensor can be extracted by [50]

$$\mu_{ij} = \left(\frac{e}{k_B T}\right)\left\langle \tau(\underline{k}) v_i(\underline{k}) v_j(\underline{k}) \right\rangle \tag{2.5}$$

here v_i and v_j are the velocity components along i^{th} and j^{th} directions respectively.

2.4 Band-like transport in organic molecular crystals

Band-like transport is characterized by an increase in the mobility with decreasing temperature, i.e. the mobility follows a power law given by

$$\mu(T) \sim T^{-n} \tag{2.6}$$

This typical temperature dependence arises due to the scattering of charge carriers by the lattice phonons. Exponent *n* in *equation 2.6* contains information about the occurring scattering mechanisms, e.g. scattering by acoustic and/or optical phonons , bandwidth of the conduction level, and relaxation time of the charge carriers. Obviously, estimation of the exponent alone does not provide the complete information about the exact transport mechanism and complementary studies, e.g. IR absorption spectroscopy [51], ellipsometry [52] etc. in combination with *ab initio* theoretical studies [53,54] are necessary to understand the charge carrier transport in organic semiconductors. In this section, we shall have a look into different transport models in the framework of existence of electronic bands in organic molecular crystals.

2.4.1 Mobility: Wide band theory

Wide band theory is commonly used to describe the electric field and temperature dependence of the mobility in inorganic semiconductors. Benchmark works by Warta and Karl [29,49] in which they measured the charge carrier mobility for electrons and holes in ultra-pure organic crystals of naphthalene lead to application of this wide-band approximation in organic crystals. *Figure 2.6 (a)* shows the electron and hole mobilities along the crystallographic *a*-direction in naphthalene single crystal as function of temperature.

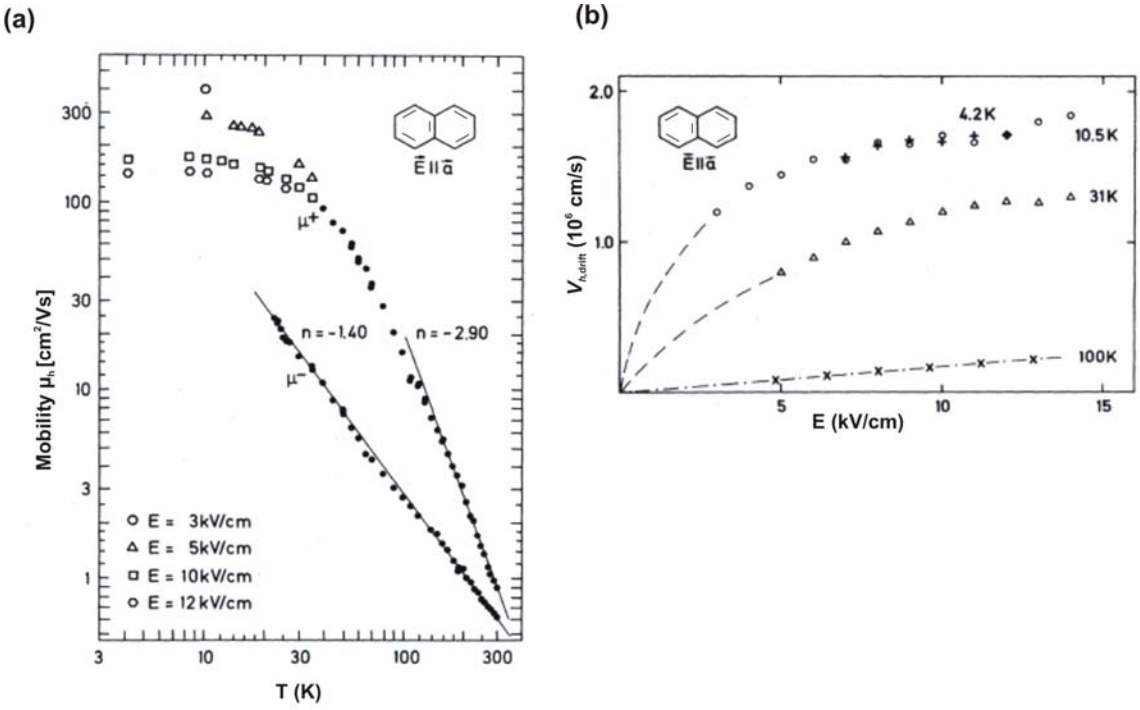

Figure 2.6 (a) *Electron and hole mobilities along the crystallographic a-direction in ultra-pure naphthalene crystal.* ***(b)*** *Hole drift velocities as function of electric field at various temperatures [49].*

Hole mobility obeys a power law dependence with $\mu_h \sim T^{-2.9}$ whereas electron mobility shows a temperature dependent behavior given by $\mu_e \sim T^{-1.4}$ up to 40 K. The field dependent drift velocity for hole saturates at higher electric fields for temperatures below 40 K, as shown in the *figure 2.6 (b)*. High hole mobilities of ~ 400 cm^2/Vs at 10 K and

typical power law dependence of mobility on the temperature can only be explained by band-like transport. Moreover, saturation of the drift velocity was successfully explained by assuming a wide band ($W > k_B T$) with non-parabolic band approximation, where W is the bandwidth. In the following, we shall define the arguments based on non-parabolic band approximation to explain the saturation of the drift velocity at high electric fields.

Non-parabolic band: saturation of drift velocity

Assuming a cosine shaped non-parabolic band in tight-binding approximation, the dispersion relation can be described by

$$\varepsilon(k) = E_0 - \frac{1}{2} W \cos(\vec{k} \cdot \vec{a}) \qquad 2.7$$

where $\vec{a}$ is the unit cell vector along the crystallographic a-direction. A single charge carrier starting at $k = 0$, i.e. at the center of the Brillouin zone would be scattered back after a defined collision time τ. Just before scattering, the charge particle would attain a momentum $\hbar k$ and at this moment it would reach a velocity

$$v(\tau) = \frac{1}{\hbar} \frac{\partial \varepsilon}{\partial k}\bigg|_{k(\tau)} = \frac{Wa}{2\hbar} \sin\left[\frac{eaE}{\hbar}\tau\right] \qquad 2.8$$

where E is the external electric field. Assuming that the collision time τ is sufficiently small, so that the particle does not reach the zone boundary before being scattered, an average velocity achieved between the times 0 and τ can be described by

$$\bar{v}(E,\tau) = \frac{Wa}{2\hbar}\left[1 - \cos\left[\frac{eaE}{\hbar}\tau\right]\right]\left[\frac{eaE}{\hbar}\tau\right]^{-1} \quad . \qquad 2.9$$

For small E we can expand the cosine term to obtain an Ohmic behavior given by

$$\bar{v} = \mu E, where \mu = \frac{e}{m^*}\tau \quad . \qquad 2.10$$

For very high fields, *equation 2.9* leads to a saturated maximum drift velocity given by

$$v_{\max} = \frac{0.724Wa}{\pi\hbar} \quad . \qquad 2.11$$

As indicated by *equation 2.11*, at high fields the drift velocity depends only on the bandwidth of the conduction level and the periodicity along the transport direction. Using *equation 2.11*, the estimated bandwidth of 40 meV along the crystallographic *a*-direction in naphthalene proves to be in good agreement with the calculated value ~30 meV reported in the literature [55] and therefore supporting the adequacy of a non-parabolic wide band approach. For a detailed study of transport in naphthalene crystals we refer readers to the PhD thesis of W. Warta [49].

However, the argumentation of a non-parabolic band approximation leading to the saturation of drift velocity was challenged by Kenkre et. al. as he suggested that the saturation behavior is a consequence field-dependence and/or *k* dependence of the scattering rate [56].

2.4.2 Mobility: Narrow band theory

Wide-band approach with non-parabolic band approximation was successfully applied to explain the saturation of drift velocity in naphthalene crystals. However, this model is not adequate to explain the transport behavior in other OMCs where no saturation of drift velocity was observed. Moreover, weakly bounded molecules in OMCs result in small overlap integrals and hence favoring the narrow-band approach over the wide-band approach.

A narrow-band approach was proposed by Schein to study the temperature dependent mobility in molecular crystals of As_2S_3 and of anthracene [57]. As we have seen in the previous section, in case of a band theory approach the mobility can be estimated by using the relaxation time τ approximation for the Boltzmann equation [50]. For a degenerate semiconductor, the mobility can be assigned to

$$\mu = \left(\frac{e}{k_B T}\right)\left\langle \tau v_i^2 \right\rangle \qquad 2.12$$

where v_i is the charge carrier mobility along the i^{th} crystallographic direction. In case of wide-band approach one can relate the kinetic energy of the charge particle with its thermal energy by

$$\frac{1}{2}mv_i^2 = \frac{1}{2}k_BT \quad . \qquad 2.13$$

Equation 2.12 and *2.13* together provide the mobility expression given by *equation 2.10*. However, in case of narrow-band approximation ($W \cong k_{BT}$) the effective mass approximation is no longer valid because all k states in the band are thermally occupied instead of just the states at the band minima. According to Fröhlich and Sewell [58], in this case the magnitude of v_i can be estimated as some fraction of the maximum velocity in the band. In the tight-binding approximation, this results in [50]

$$|v_i| \approx \frac{Ja}{\hbar} \qquad 2.14$$

where a is the lattice constant and J is the electron overlap integral, which in following is assumed to be temperature independent. For a three-dimensional cubic crystal, the corresponding bandwidth is given by $6J$ [48]. *Equations 2.12* and *2.14* give

$$\mu = \frac{e\lambda}{k_BT}\frac{Ja}{\hbar} \qquad 2.15$$

where $\lambda = v_i\tau$ is the mean free path. The main difference between wide-band and narrow-band approach is that in case of the latter, the velocity becomes temperature independent and the temperature dependence of the mobility arises from the temperature dependence of the relaxation time. The relaxation time depends on the various scattering mechanisms, such as scattering by acoustic or optical phonons. Therefore, in the next section we briefly introduce scattering mechanisms in organic crystals.

2.4.3 Scattering of charge carriers: electron-phonon coupling

As discussed in the previous section, the charge carrier transport in narrow-band OMCs depends on the electron exchange interactions and various scattering mechanisms. Scattering by phonon modes in a periodic lattice has a major impact on the mobility.

Various research papers deal with analyses of the exponent in the power law dependence of the temperature dependent mobility in the framework of scattering by acoustic and optical phonons [53,59,60].

In inorganic crystals, the electron exchange interaction is much larger compared to the electron-phonon coupling and therefore charge carriers can be treated as quasifree particles which are occasionally scattered by phonons. However, in weakly bounded molecular crystals the situation is different: the electron exchange interaction is much smaller due to the weak overlap of molecular orbitals whereas the electron-phonon interaction remains almost of the same order as in inorganic semiconductors. Therefore, electron-phonon coupling is a determining parameter influencing the charge transport. The gradually varying electrostatic potential is superimposed by the periodic lattice potential, which resembles to acoustic modes of phonons in non-polar lattices. The effective potential is also referred to as deformation potential in which charge carriers move [61].

Under the assumptions: (1) elastic scattering, (2) isotropic scattering, and (3) mean free path is independent of the velocity of charge carrier, scattering by acoustical vibration modes results in power law dependence of mobility as $T^{-1.5}$ [62]. Such power law is commonly observed in pure non-polar crystals of Ge, Si and Te. However, in case of polar OMCs charge carriers can be scattered by acoustic as well as optical phonons and both acoustic and optical deformation potentials have to be considered and the temperature dependence of the mobility has to be modified by the following equation [63]

$$\mu(T) = \mu_{acoustic}(T) f(T) \quad . \qquad 2.16$$

Where the additional factor *f(T)* depends on the optical phonon energy, occupation density of phonon branches, and the strength of electron-phonon coupling. For strong *f(T)*, combined effect of scattering by acoustic and optical phonons can lead to a rather strong temperature dependence, as observed in various organic crystals [29,32,33].

Apart from scattering by acoustic and optical phonons, Coulomb scattering, scattering by neutral impurities, scattering by dislocations might also take place, which makes the mobility behavior even more complex. *Table 2.1* shows the temperature dependence of

mobility for narrow-band as well as wide-band semiconductors under the influence of different scattering mechanisms.

Table 2.1 *Temperature dependence of mobility in wide-band and narrow-band semiconductors under the influence of various scattering mechanisms.*

Scattering	**μ (wide-band)**	**μ (narrow-band)**
Acoustic phonons One phonon Two phonon	$T^{-1.5}$ [62]	T^{-2} [64] T^{-3} [65]
Optical phonons One phonon Two Phonon	$T^{0.5}[\exp(h\nu/k_BT)-1]$ [66]	$[\exp(h\nu/k_BT)-1]$ [57] $[\exp(h\nu/k_BT)-1]^2$
Coulomb	$T^{1.5}$ [67]	T^{-1} [57]
Neutral impurity	T^{0} [68]	T^{-1} [65]
Dislocation	$T^{-0.5}$ [69]	T^{-1} [57]

Consistency of the band transport theory

One of the fundamental criterion to check the consistency of the band transport theory is the mean free path $\lambda = v\tau$ of the charge carriers. Adequacy of the band picture requires that the mean free path should be significantly larger than the lattice constant ($\lambda > a$) so that charge carriers can move like quasifree particles in the electronic band. The relaxation time can be estimated from the Heisenberg uncertainty principle

$$\Delta E \cdot \Delta t \geq \hbar \Rightarrow \tau \geq \frac{\hbar}{W} . \qquad . \qquad 2.17$$

Here τ is the lifetime of the charge carrier in a band of energy dispersion width W. This life-time can be regarded as the time over which a charge carrier moves coherently in a band before scattering and therefore can be defined as carrier relaxation time. In order to be band-model consistent, the minimum limit of the mobility can be expressed by combining *equation 2.12 and 2.17* as

$$\mu > \frac{ea^2}{\hbar} . \frac{W}{k_B T} \qquad . \qquad 2.18$$

Low temperature mobility values in ultra pure single crystals of various organic semiconductors, e.g. naphthalene [29], anthracene [32], perylene [33], and durene [37] satisfy *equation 2.18*. However, room temperature mobility values in most of these organic semiconductor crystals are in the order of ~ 1 cm^2/Vs which falls in the regime between band-like and hopping transport.

Table 2.2 summarizes the highest room temperature mobilities for holes measured in various organic crystals and compares it with the theoretical limit of the mobility required for the transport under the assumption of a wide-band model. The band-width values are taken from the theoretical calculations by Bredas et. al [70,71]. It is worth mentioning that they did not consider charge carrier interactions with lattice phonons, which depends strongly on the temperature, and therefore values obtained are overestimated and can be used only to check the consistency of the wide-band transport. At room temperature very few organic semiconductor satisfy the condition given by *equation 2.18*. As shown in *table 2.2*, room temperature hole mobilities in naphthalene, anthracene, and tetracene are almost one order of magnitude lower than the theoretical limit. Though, room temperature FET hole mobilities in pentacene and rubrene are sufficiently high and indicate band-like transport.

Table 2.2 *Comparison of the minimum mobility required for a band-like transport at RT and experimentally measured hole mobilities in selected PAHs.*

	$W_{theoretical}$ $(T=0)$ [70,71]	$\mu_{min,theoretical}$ [cm^2/Vs]	$\mu_{max.,\ exp.}$ [cm^2/Vs]
Napthalene	~ 409 meV	~ 8	~ 0.32 [29]
Anthracene	~ 509 meV	~ 10	~ 0.73 [32]
Tetracene	~ 625 meV	~ 12.5	~1 [7]
Pentacene	~ 738 meV	~ 15	~35 [35]
Rubrene	~ 350 meV	~ 7	~ 43 [72]

Above consistency check is based on wide-band transport theory, where the band-width changes only slightly with the temperature. However, in case of organic semiconductors the situation is more complicated and the band-width varies strongly with the temperature. Hannewald et al. reported theoretical calculations on polaron bandwidth

narrowing in organic crystals with increasing temperature [73]. It was shown that the HOMO polaron band-width in naphthalene crystals narrows from ~ 250 meV at 20 K to ~25 meV at 300 K, comparable to the thermal energy at 300 K. Also, Troisi et al. reported that thermal molecular motions result in fluctuations in the transfer integrals and for temperatures above 150 K, these fluctuations become comparable to the band-width and destroy the band-structure, ruling out any coherent transport in this temperature regime[74].

2.5 Polaron band transport in OMCs

OMCs are mostly molecular solids with theoretical calculations suggesting the band-width lying between 100 meV to 600 meV at room temperature [70, 71], and therefore charge carriers in OMCs show the strong tendency to localize, resulting in the formation of polarons. A polaron is a quasiparticle, which is composed of a charge accompanied by local distortion of the crystal lattice induced by the charge carrier itself. A polaron is associated with a polarization cloud, which forms an energy potential well and hinders the motion of the charge carriers.

If the molecular relaxation takes place during the residence time of the charge carrier on a molecular site then the charge carriers might get trapped by the molecular relaxation, forming a polaron. In other words, a polaron is a self-trapped state of the charge carrier in a crystal lattice. Polarization might occur on various time scales depending on the respective processes.

Polarons formed by *electronic polarization* (10^{-16} – 10^{-15} sec) in the molecule due to the shielding of the uncompensated charge carrier lower the energy of this charge carrier by approximately 1 eV.

Vibronic polarization (10^{-15} – 10^{-14} sec) results in small polarons, in which case the molecular cation or anion adjusts its nuclear configuration. Formation of small polarons lowers the energy of charge carriers by almost 0.1 eV.

In case of *lattice polarization* (10^{-13} – 10^{-12} sec), the surrounding molecules adjust their nuclear configuration, resulting in *large polarons*. This is a relative slow process and it lowers the charge carrier energy by < 0.1 eV.

Holstein proposed a polaron band transport model assuming a small polaron in a one-dimensional molecular crystal along with a tight-binding approximation [75]. Under above treatment charge carrier mobility can be given by

$$\mu(T) = \frac{ea^2}{k_B T} 2\omega \left[\frac{\alpha}{\pi} \operatorname{csc} h \left[\frac{\hbar\omega}{2k_B T} \right] \right]^{1/2} \times \exp\left[-2\alpha \operatorname{csc} h \left[\frac{\hbar\omega}{2k_B T} \right] \right] \qquad 2.19$$

here $\alpha = E_p/\hbar\omega$ represents the strength on the electron phonon coupling with E_p as polaron binding energy. *Equation 2.19* suggests strong increase in mobility with decreasing temperature. Hannewald et al. proposed a generalized model for high charge carrier mobility by including non-local electron-phonon coupling in Holstein's polaron model to successfully explain the charge carrier mobility and its spatial anisotropy in naphthalene [53].

2.6 Hopping transport in organic semiconductors

Localization of charge carriers either caused by the narrowing of bands or because of the trap states induced due to chemical impurities or structural defects lead to thermally activated hopping transport in organic semiconductors. Hopping transport is commonly observed in disordered semiconductors or in organic polymers where charge carriers must hop from one site to the next. Hopping transport is characterized by an increase in mobility with increasing temperature. Experimental findings reveal that apart from the temperature, hopping transport might also depend on the field strength. In this section we shall introduce some standard hopping transport models, which are widely used to explain temperature and field dependent mobilities in organic semiconductors.

In case of hopping transport, the transport depends on the intersite jump rate ν_{ij}. Charge carrier hopping from one site to another proceeds via absorption or emission of a phonon. *Miller-Abrahams* (*M-A*) formalism provides an expression for the jump rate between sites *i* and *j* under *single phonon approximation* [76]. It assumes a weak overlap of electronic wave functions between neighbouring sites *i* and *j* with energies ε_i and ε_j respectively. Under these assumptions, the jump rate can be calculated as,

$$\nu_{ij} = \nu_0 \exp\left(\frac{-2r_{ij}}{b}\right) \cdot \exp\left[\frac{-(\varepsilon_j - \varepsilon_i)}{k_B T}\right] \quad \text{for } \varepsilon_j > \varepsilon_i \text{ (absorption)} \qquad 2.20$$

and

$$\nu_{ij} = \nu_0 \exp\left(\frac{-2r_{ij}}{b}\right) \qquad \text{for } \varepsilon_j < \varepsilon_i \text{ (emission)} \qquad 2.21$$

where ν_0 is given by

$$\nu_0 = \frac{A\overline{(\varepsilon_j - \varepsilon_i)}}{\hbar} \quad . \qquad 2.22$$

A is a dimensionless constant and r_{ij} is the intersite distance. The *M-A* formalism is the basis of various hopping transport models.

2.6.1 Thermally activated hopping

Thermally activated processes follow an *Arrhenius Law* [77], i.e. rate of hopping from one site to another depends on the activation energy E_a and the temperature T. Mathematically, the hopping rate R can be expressed by

$$R = \nu_0 \exp\left[\frac{-E_a}{k_B T}\right] \quad . \qquad 2.23$$

Here ν_0 is the attempt frequency which depends on the activation energy of the traps. In polymers ν_0 might vary between 10^9 sec^{-1} to 10^{12} sec^{-1} for trap energies ranging from 0.4 eV to 0.9 eV [78]. The resulting mobility is proportional to the hopping rate and is given by

$$\mu(T) = A \exp\left[\frac{-E_a}{k_B T}\right] \quad . \qquad 2.24$$

Here the prefactor A is a material dependent property. The activation energy E_a contains various parameters such as energy barriers at grain boundary, polaron binding energies, fluctuations in transfer integrals, etc. Thermally activated hopping transport is widely reported on polymers [79] and organic thin films [80].

2.6.2 Poole-Frenkel model

Field and temperature dependence of charge carrier mobilities in polymers and amorphous organic semiconductors are quite often described by the *Poole-Frenkel model*. In this model, the Coulomb potential near a localized charge is modified by an external electric field E so as the free-carrier density increases with increasing field [81,82]. The *Poole-Frenkel model* can be applied to systems where the drift-mobility is limited by traps or localized states, i.e. polymers, thin films or crystals with high impurity concentrations. In the framework of this model, the charge carrier drift mobility can be expressed by

$$\mu(E,T) = \mu_0 \exp\left[-\frac{E_a - \beta E^{0.5}}{k_B T_{eff}}\right] \qquad 2.25$$

where

$$\frac{1}{T_{eff}} = \frac{1}{T} - \frac{1}{T_0} \qquad 2.26$$

and

$$\beta = \sqrt{\frac{e^3}{\pi \varepsilon_r \varepsilon_0}} \quad . \qquad 2.27$$

E_a is the activation energy and β is a constant, which depends only on the dielectric constant of the material. A sufficiently high density of localized states is needed for adequacy of this model. However, this model is oversimplified and ignores many important parameters e.g. variation of the potential barrier to the next hopping site in presence of an external electric field. Therefore corrections are needed in this model to estimate an adequate value of the mobility.

2.6.3 Bässler model

Another model, proposed by Bässler considers the distribution of hopping site energies and intersite distances [83]. This is also known as disorder model. In localized systems,

energy disorder (or diagonal disorder) results in a Gaussian distribution of energy levels and spatial disorder (of off-diagonal disorder) results in a Gaussian distribution of hopping distances respectively. This model is based on the assumption that in the absence of long-range order, which holds true e.g. for polymers and thin films, the transport proceeds mainly via localized states with energy and intersite states having Gaussian distribution. Under these assumptions the carrier mobility is defined by

$$\mu(E,T) \propto \mu_0 \exp\left[-\left(\frac{T_0}{T}\right)^2\right]\exp\left(\frac{E}{E_0}\right) \quad . \qquad 2.28$$

Where μ_0 is the temperature independent zero-field ($E = 0$) mobility. T_0 is related to the width of Gaussian density of states σ by $T_0 = K\sigma$ where K is a constant and E_0 is the constant, which depends on the material and the width of the Gaussian distribution of states. This model is used to explain the transport behavior in disordered organic semiconductors, mainly polymers and amorphous organic semiconductors [83,84].

2.6.4 Polaron hopping

In case of polaron hopping, the *M-A* formalism has to be modified by assuming a two-phonon process (i.e. simultaneous absorption of one phonon and the emission of another) instead of one phonon process because of the stronger electron-phonon coupling. The main effect of polaronic contribution, when the electron-phonon interaction is large, is to introduce an exponentially depending term in the jump rate and assuming a temperature dependent prefactor in *equation 2.20 and 2.21*. Austin proposed a hopping transport model in case of strong electron phonon coupling which results in a mobility for a one dimensional chain given by [85]

$$\mu(E,T) = \mu_0(T)\exp\left[-\frac{e^2a^2E^2}{8E_pk_BT}\right]\frac{\sinh(eaE/2k_BT)}{eaE/2k_BT} \quad . \qquad 2.29$$

Here E_p is the polaron binding energy, which is half of the activation energy, on a linear chain with lattice distance a. It was proposed by the above formulation that the electric field can not only increase, but also can decrease the hopping mobility by reducing the

probability of energy level coincidence. Fischuck et. al. provided a polaron hopping transport model for disordered organic semiconductors [86].

2.7 Hoesterey-Letson (H-L) model

Temperature dependent mobility behavior in most of the organic solids does not follow any standard transport model due to the effects of residual impurities and structural defects. A general trend observed in most of the organic crystals is an initial increase in the mobility with increasing temperature followed by a decrease after reaching a certain maximum. Hoesterey and Letson proposed a model to explain the combined effects of thermally activated and band-like transport on the temperature dependence of mobility [87], also known as *multiple-shallow-trapping and release* model.

Let μ_0 and n_0 be the mobility and carrier density in the conduction band. N_t carriers are trapped at a trap depth of E_t. Now this situation can be distinguished by two cases, namely *shallow traps* and *deep traps*. Shallow traps are characterized by the condition $t_r << \tau$, where t_r is the life time of the carrier in the trap and τ is the transit time of the charge carrier across the sample. Also, the characteristic trap energies should be less than several k_BT (e.g. 200 meV) so that the thermal energy is sufficient to release charge carriers from the tail of the exponential trap distribution whereas in case of deep traps, charge carriers once trapped can not be released by the thermal energy.

In case of shallow traps, during the transit, the effective mobility is related to the trap free mobility by

$$\mu_0 n_0 = \mu_{eff}(n_0 + n_t) \tag{2.30}$$

where n_t is the density of trapped charges. At thermal equilibrium we have an occupation of traps according to the Boltzmann distribution,

$$\frac{n_t}{n_c} = \frac{N_t}{N_c}\exp\left(\frac{E_t}{k_BT}\right) \tag{2.31}$$

with N_t and N_c are the total density of trap states at E_t and density of conduction states at the band edge, respectively. *Equations 2.30 and 2.31* lead to an effective mobility given by

$$\mu_{eff}(T) = \mu_0(T)\left[1 + \frac{N_t}{N_0}\left\{\exp\left(\frac{E_t}{k_B T}\right) - 1\right\}\right]^{-1} \qquad 2.32$$

where N_0 is the density of conduction states in the conduction band (valence band) for electrons (holes).

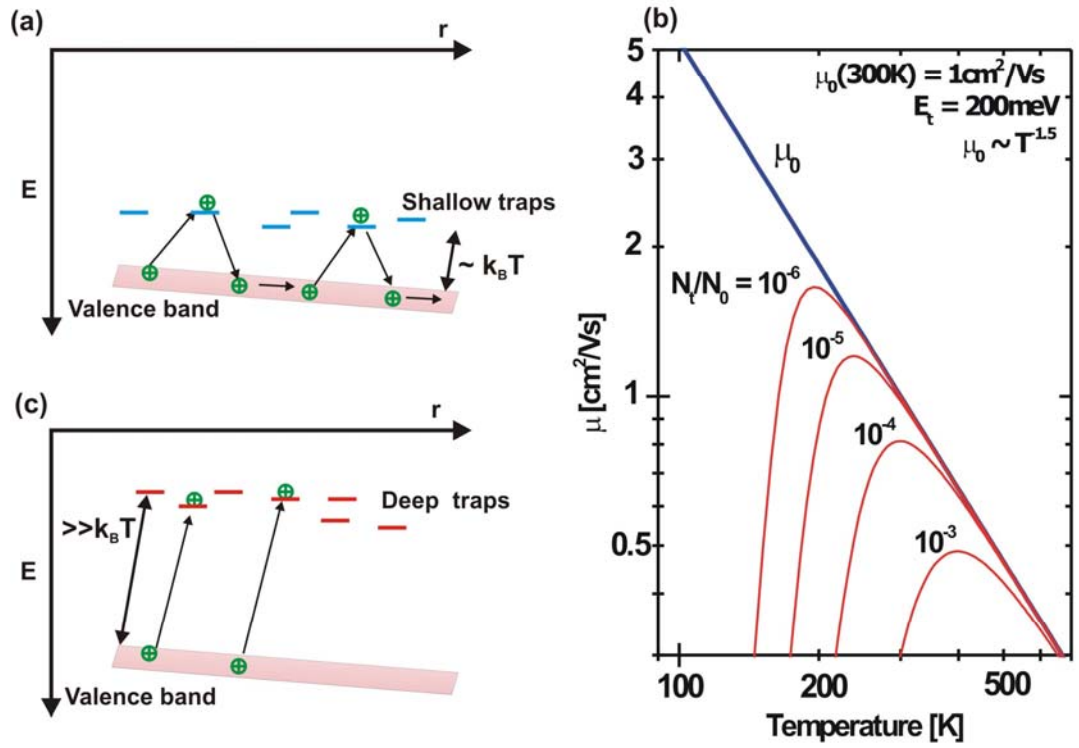

Figure 2.7 (a) *Schematic representation of the H-L model.* ***(b)*** *Temperature dependent mobility behavior as depicted by the H-L model. Blue line represents the intrinsic mobility (equation 2.6) and red curves are temperature dependent mobility calculated by H-L model (equation 2.32) for different trap densities.* ***(c)*** *Effect of deep traps: thermal release of the charge carriers is not possible.*

Figure 2.7 (a) shows the schematic representation of the *H-L model* for hole transport. Temperature dependent mobility behavior predicted by *H-L model* (*equation 2.32*) is shown in the *figure 2.7 (b)*. Characteristic trap energy of 200 meV and the room temperature intrinsic mobility of 1 cm^2/Vs is assumed and the temperature dependence of

mobility is plotted for different trap densities. Exponent n = 1.5 indicates the scattering by acoustic phonons. *Figure 2.7 (c)* represents the situation of deep trapping where trapped charge carriers can not be released by thermal energy.

At very low temperatures the exponential term in *equation (2.32)* dominates and almost all the charge carriers are trapped in shallow traps. In this case, the effective mobility shows the thermally activated transport given by

$$\mu_{eff}(T) \approx \mu_0(T) \exp\left(-\frac{E_t}{k_B T}\right) \quad . \qquad 2.33$$

Whereas at high temperatures, charge carriers are released much faster from the shallow traps and the mobility behavior is mainly governed by the motion of charge carriers in the transport band. In that case, the effective mobility is almost equal to the intrinsic mobility described by *equation 2.6*.

In this chapter we have seen that the temperature dependent mobility in organic solids is very much system specific and therefore it is not possible to propose a universally accepted model for charge carrier transport in organic semiconductors [88]. However, these theoretical models for charge carrier transport provide a basis to understand the experimental results.

3 Materials, Purification and Crystal Growth

In this chapter we will first introduce the organic semiconductors: diindenoperylene and diphenylanthracene, which are investigated in this work and we will discuss advantages these materials have over various other PAHs. Material purification is one of the most important steps in order to obtain good structural order and thereby high mobilities in organic semiconductor devices, especially in case of devices based on organic crystals. It has been shown in the past that chemical impurities severely hamper the electronic transport properties of organic semiconductors [89,90]. Even impurities in the order of *sub-ppm* level can drastically degrade the electronic properties and hence the device performance. *Figure 3.1* shows the effect of impurities on the electronic transport properties of anthracene single crystals intentionally doped with 0.1 ppm of tetracene [90].

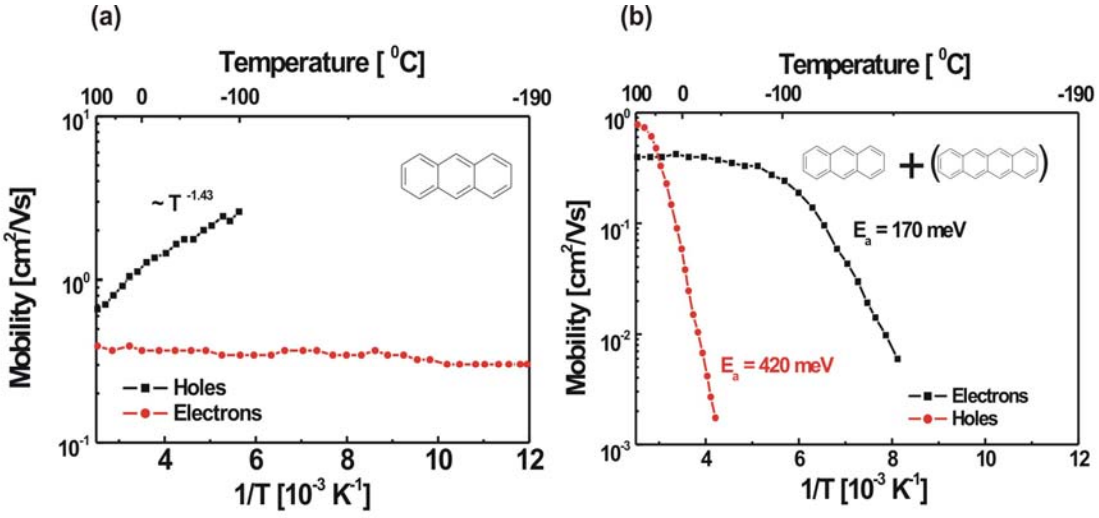

Figure 3.1 *Temperature dependent mobility of electrons and holes along the c'-direction in* ***(a)*** *ultra-pure anthracene crystals and* ***(b)*** *anthracene crystal doped with 0.1 ppm tetracene [90].*

As shown in *figure 3.1 (a)*, the hole mobility increases with decreasing temperature as ~ $T^{-1.43}$ and the electron mobility remains almost constant over the entire temperature range down to -190 °C.[†] The increase in the mobility with decreasing temperature, as discussed in Chapter 2, is a signature of the band-like intrinsic transport. In *figure 3.1 (b)*, the temperature dependent electron and hole mobilities in anthracene crystals, doped intentionally with 0.1 ppm of tetracene, are shown. Both electron and hole mobilities now exhibit a thermally activated behavior, i.e. increase in mobility with increasing temperature with an activation energy of 420 meV for holes and 170 meV for electrons. Again, thermally activated behavior is a consequence of broken translational symmetry and hence the distortion in band structure due to the presence of chemical defects caused by tetracene, which act as electrically active trap states for electrons and hole, resulting in a non-intrinsic electronic transport. Therefore it is mandatory to purify the material before it can be used for crystal growth or device fabrication.

3.1 Materials

3.1.1 Diindenoperylene (DIP)

Diindenoperylene (DIP), full chemical name: *diindeno[1,2,3-cd: 1',2',3'-Im]perylene* is a derivative of perylene with two indeno groups attached opposite to each other on the perylene backbone. *Figure 3.2* shows a sketch of the DIP molecule. DIP molecule stretches ~ 18.4 Å in length and ~ 7Å in width. The physical properties of DIP are summarized in the *table 3.1*.

Table 3.1 *Physical properties of DIP*

Chemical formula	$C_{32}H_{16}$
Molecular weight	400.48 g/mol
Bulk density	1.35 g/cm^3
Sublimation temperature	~ 350 °C
Appearance	Red powder

[†] Various research papers discuss the temperature independence of the electron mobility in anthracene However, there has been no convincing transport model proposed yet to explain this behavior.

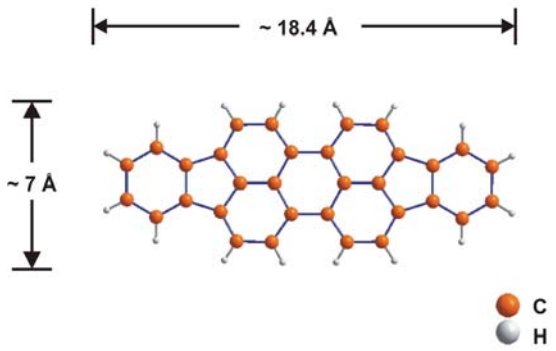

Figure 3.2 *Schematic representation of DIP molecule.*

DIP is known to form highly ordered thin films on weakly interactive substrates such as SiO_2 [91]. Encapsulated thin films of DIP exhibit strong thermal stability and sustain crystallinity even up to ~ 400 ^{o}C as it was shown by Sellner et.al.[92,93]

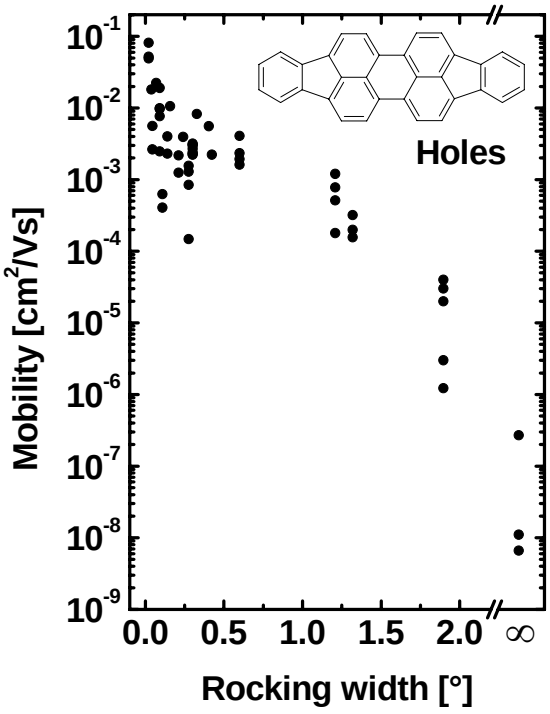

Figure 3.3 *Hole mobility in DIP thin film FETs as a function of structural order [28].*

Besides thermal stability, DIP thin films exhibit remarkable semiconducting properties, e.g. exciton diffusion length as large as ~ 100nm and therefore rendered useful for OPVCs applications [94], and in TFTs providing hole mobilities as high as 0.1 cm^2/Vs at room temperature [95]. It was further shown that the mobility depends strongly on the structural order of the films [28]. *Figure 3.3* shows the dependence of the hole mobility on the structural order of the DIP thin film, where the abscissa represents the rocking width, e.g. average tilting of crystallites. Hole mobility increases by almost seven orders of magnitude from 10^{-8} cm^2/Vs to ~ 0.1 cm^2/Vs by increasing the structural order from almost amorphous (rocking width > 2°) to highly ordered film (rocking width ~ 0.02°). Strong enhancement of the mobility with increasing structural order is an impetus to study the electronic transport in DIP crystals as will be reported in Chapter 6.

3.1.2 Diphenylanthracene (DPA)

9,10-Diphenylanthracene (DPA) is the second organic semiconducting compound that is studied in this thesis. DPA too is chemically stable due to the formation of three aromatic sextets and hence is expected to show ambipolar transport. DPA is a substitute of anthracene with two phenyl groups attached to the 9,10-positions on the anthracene backbone. *Figure 3.4* shows the schematic representation of the DPA molecule.

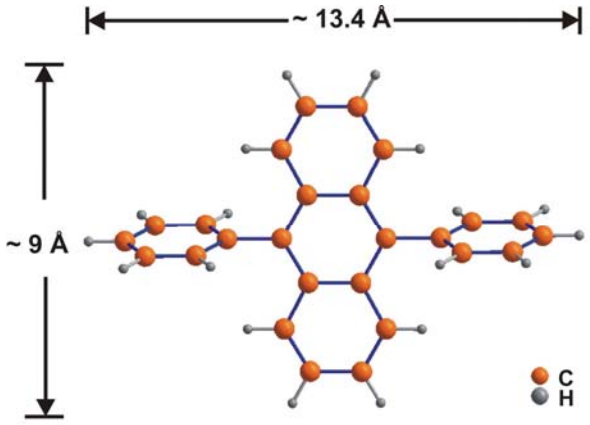

Figure 3.4 *Schematic representation of the DPA molecule.*

DPA molecule stretches ~ 9Å along the anthracene backbone and ~ 13.4Å along the phenyl groups. DPA has similar molecular motif as the rubrene molecule, which shows excellent electronic transport properties at its crystal surfaces [36]. However, DPA has a strong advantage over rubrene, as in contrast to rubrene it melts without decomposition and therefore provides the possibility to achieve ultra-high purity by applying zone-refinement and hence to minimize the amount of chemical impurities. Important physical properties of DPA are summarized in *table 3.2*.

Table 3.2 *Physical properties of Diphenylanthracene*

Chemical formula	$C_{14}H_8(C_6H_5)_2$
Molecular weight	330.42
Bulk density	1.23 g/cm^3
Melting point	~ 250 °C
Appearance	Yellowish powder

Recognition of semiconducting properties of DPA started with the observation of laser action in liquid DPA at a wavelength of 4326 Å when pumped by the second harmonic of a ruby laser [96]. Further application of DPA involves fabrication of blue light emitting diodes based on the DPA moiety [97]. Recently DPA platelets have been used as gate insulator for rubrene crystal based OFET yielding a room temperature hole mobility as high as ~ 43 cm^2/Vs [72]. But to date, electronic transport studies in DPA crystals have been less conclusive due to the poor injection into the material because of the mismatch between HOMO/LUMO level and the respective metal Fermi level. In this thesis we shall study the temperature dependent electronic transport properties in DPA crystals by using the injection free Time-Of-Flight (TOF) method and will further check the feasibility of this compound for organic electronic applications.

3.1.3 Chemical stability of DIP and DPA

As discussed in Chapter 2, chemical stability of PAHs depends on the aromaticity of these compounds. In order to experimentally verify the relative stability of DIP and DPA against the photo-oxidation, we performed UV-Vis absorption spectroscopy on various

organic compounds dissolved in the organic solvent toluene. Samples were exposed to ambient and UV light for different times and UV-Vis spectra were subsequently recorded using a Perkin-Elmer Lambda UV-Vis spectrometer.

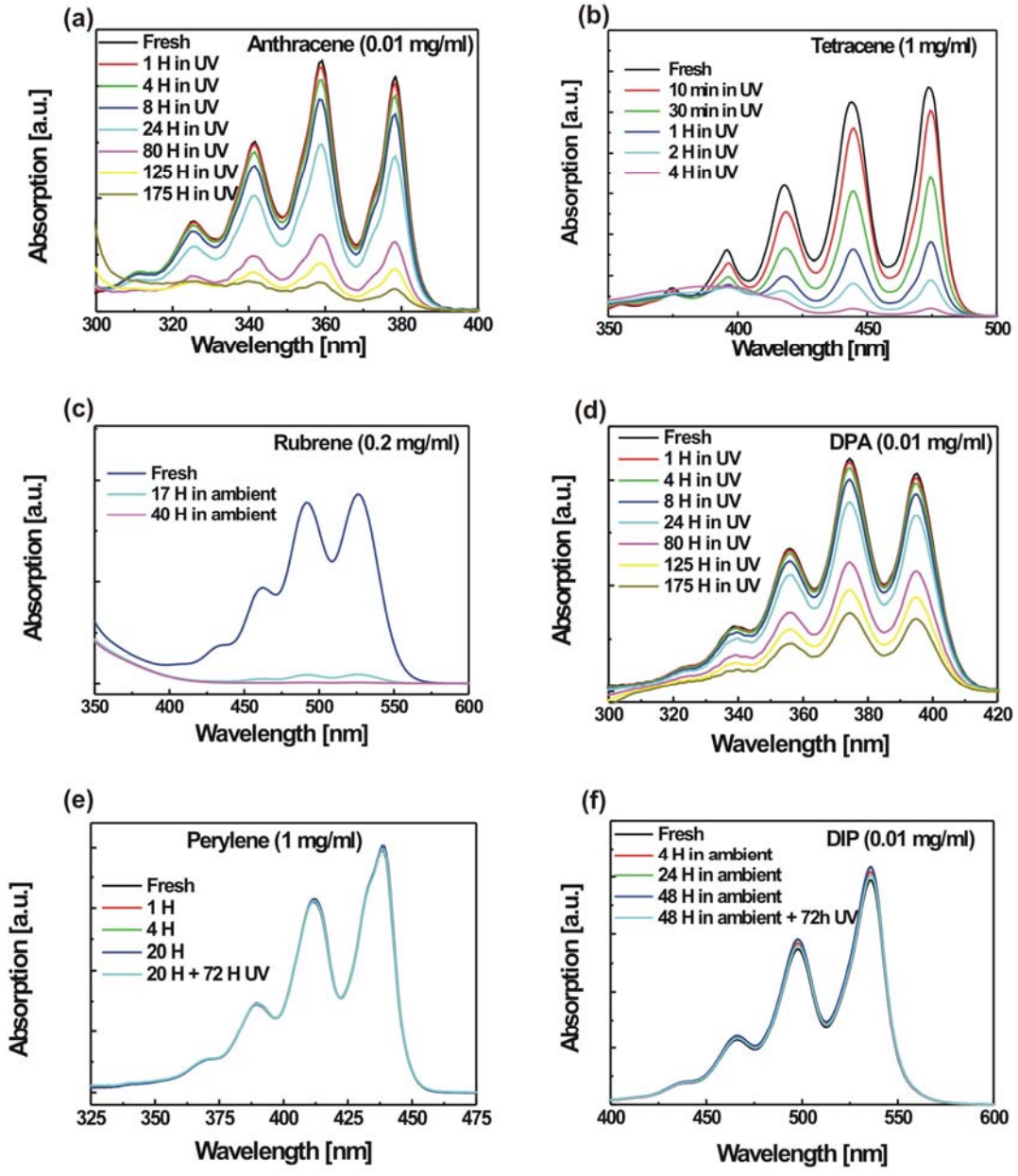

Figure 3.5 *UV-Vis spectra of selected organic compounds dissolved in toluene and exposed to ambient and UV light for different time.* ***(a)*** *Anthracene,* ***(b)*** *Tetracene,* ***(c)*** *Rubrene,* ***(d)*** *DPA,* ***(e)*** *Perylene, and* ***(f)*** *DIP.*

Samples were prepared by dissolving purified organic compounds in toluene and afterwards solutions were filled into quartz cuvettes. Molar concentrations of different compounds were chosen according to the intensity of the respective absorption spectrum. This experiment is based on the fact that the relative decrease in the intensity of electronic transition peaks in UV-Vis absorption spectra reflects the decrease in molar concentration of the respective organic compound due to the conversion of these molecules into oxidation products.

Absorption spectra corresponding to the $S_0 \rightarrow S_1$ electronic transitions are shown in the *figure 3.5* for certain selected organic compounds. Several peaks in the absorption band correspond to the vibrational sub-levels. As it can be seen, anthracene degrades relatively slowly compared to tetracene and rubrene. Tetracene degrades under the influence of UV light by forming oxidized products resulting in a rapid decrease of the tetracene absorption peaks. After 4 hours of exposure to UV light no trace of tetracene was found in the absorption spectra [7]. Whereas the anthracene solution shows the electronic transitions corresponding to the anthracene molecule even after 175 hours of exposure to the UV light. This observation could be explained on the basis of Clar's sextet rule as mentioned in Chapter 2: compared to tetracene, anthracene has a higher ratio of aromatic sextets to unsaturated double bonds, resulting in relatively better chemical stability.

Rubrene is even more sensitive to oxidation and rapidly degrades only if exposed to ambient conditions and no traces of rubrene were found after 40 hours. DPA shows much better chemical stability compared to rubrene and anthracene and does not degrade under the ambient condition. Trace of DPA molecules could be found in the absorption spectra even after exposing the solution to the UV light for more than 175 hours. DIP and perylene exhibit remarkable chemical stability and no significant degradation were observed by exposing their solutions to UV light for more than 72 hours.

In order to perform a comparative study of photo-oxidation upon exposure to ambient and UV light, relative concentrations of anthracene and DPA have been plotted against the exposure time to UV in the *figure 3.6*. Since the intensity of the absorption spectra is directly proportion to the molar concentration of the respective compound in the solution, relative concentration has been calculated by relative absorption intensities of the

$S_0 \rightarrow S_1$ transition after exposure to UV light for a certain time to that of observed right after preparation of the solution (fresh).

The lowest $S_0 \rightarrow S_1$ transition corresponds to ~ 380 nm in anthracene and ~ 395 nm in DPA. The Molar concentration of both decay exponentially upon exposure to UV light and can be described by

$$C(t) = C_0 \exp(-kt) \qquad 3.1$$

where C_0 is the molar concentration of the compound in the fresh solution, $C(t)$ is the molar concentration after exposing the solution to UV light for time t and k is the decay rate constant.

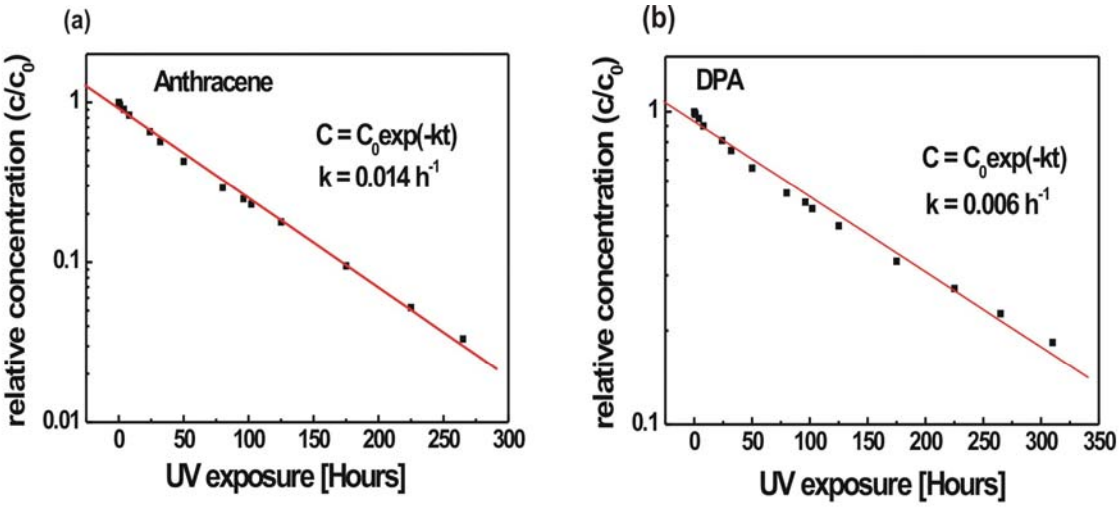

Figure 3.6 *Relative concentration as a function of exposure time in* ***(a)*** *anthracene and* ***(b)*** *in DPA. Red line represents the exponential fit to the data.*

As can be seen in the *figure 3.6*, anthracene decays faster than DPA. It takes nearly 44 hours of UV exposure for a 50% decrease in the relative concentration of anthracene whereas DPA shows much better chemical stability and needs about 100 hours of UV exposure for a 50% drop in the relative concentration. An exponential fit to the data results in a decay rate constant of ~ 0.014 h^{-1} for anthracene in ~ 0.006 h^{-1} for DPA. As for comparison, tetracene degrades rapidly with a rate constant of ~ 0.375 h^{-1} and was

proven to be chemically unsuited for any device applications without a protective capping [7].

UV-Vis spectroscopy infers the chemical stability of DIP and DPA which motivates for further electronic and structural characterization of these compounds to check the feasibility of their application in organic electronics.

3.2 Purification techniques

In this section we will introduce techniques used to purify commercially available DPA and DIP. Purification techniques can be divided into two categories: (1) from the vapor phase of the starting material and (2) from the melt.

3.2.1 Purification by zone refinement

Zone refining was introduced by Pfann [98] as a tool for material purification. This purification technique can be applied only on materials which do not decompose upon melting. Zone refining is based on the fact that a binary liquid mixture of host material (*A*) and impurity (*B*) usually forms crystals of different relative composition upon cooling. i.e.

$$k_B = \left[\frac{B}{A+B}\right]_{solid} \Big/ \left[\frac{B}{A+B}\right]_{liquid} = \frac{c_B^s}{c_B^l} \neq 1 \qquad 3.2$$

Here c_B^s and c_B^l are the concentration of the impurity amount *B* in the solid (*s*) and liquid (*l*) phases respectively. k_B is the distribution coefficient of the impurity amount *B* in the binary liquid system. *A* is the amount of the host material. If $k_B < 1$ then crystallization (or freezing) of the molten phase of a binary liquid in the ingot would result in a compound purer by a factor of k_B in the beginning compared to the portion which solidifies at later time.

On the other hand, for $k_B > 1$, the solidified portion at the later time will have relatively higher purity compared to the portion solidified in the beginning.

Figure 3.7 (a) shows the schematic of the zone refinement technique. This method applies repeated melting and recrystallization (or solidification) steps upon cycling the

passage of small molten zones along the ingot. Fractional melting of small zones avoids complete equalization of the concentration profile across the length of the ingot and hence provides the possibility of continuous purification.

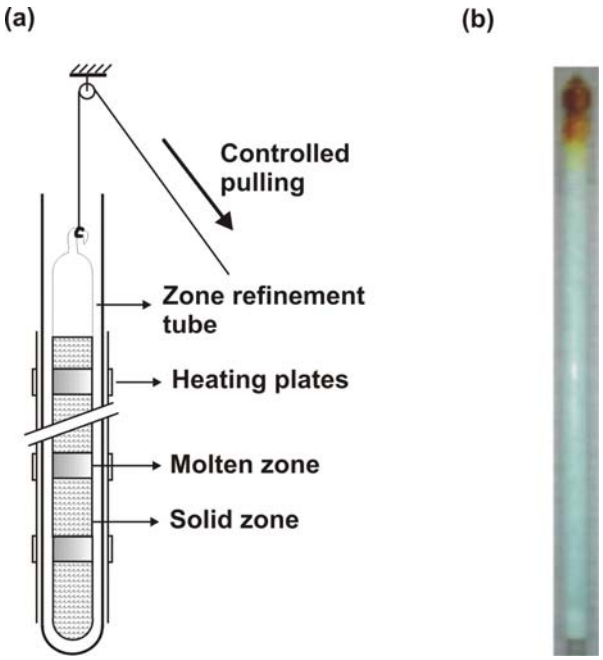

Figure 3.7 (a) *Schematic of the zone refinement technique* ***(b)*** *zone refined DPA.*

For a complete mathematical formulation of the zone refinement process we refer to literature [99]. Zone refining has been applied on various organic materials in the past, resulting in ultra-high purity and consequently resulting in improved electronic transport properties. *Figure 3.7 (b)* shows the zone refined DPA. The pristine material bought from Sigma Aldrich was purified by 140 zone refinement cycles. The segregation of impurities is clearly visible along the ingot.

3.2.2 Purification by sublimation

Zone refining is possible only for the compounds which do not decompose upon melting. Various organic semiconductors do not fulfill this criterion and decompose before they reach the melting point or just slightly above this point over long time. For example, tetracene, pentacene, rubrene, diindenoperylene etc. were found to decompose before

they melt and therefore an alternative purification technique is needed in order to reduce the impurity level in these organic compounds.

Fortunately, these organic semiconductor compounds sublime without decomposing and hence provide the possibility of purification by the sublimation method. Purification by sublimation is based on the fact that in general, impurities have different sublimation temperatures than the host material and therefore can be segregated by sublimation under a controlled temperature gradient. Purification by sublimation can be divided mainly into two methods as discussed below.

Purification by step sublimation

In this method the source material is placed inside a quartz tube and heated slightly above the sublimation temperature. *Figure 3.8* shows the schematic of the step sublimation method. The vapor phase of the host material is transported along the purification tube and condenses in the colder zone of the tube. The step sublimation method is limited by the amount of non-decomposed impurities which are present in the host material and have lower sublimation temperature than the host material. Further caution has to be taken to avoid any cross-contamination of the already purified fraction.

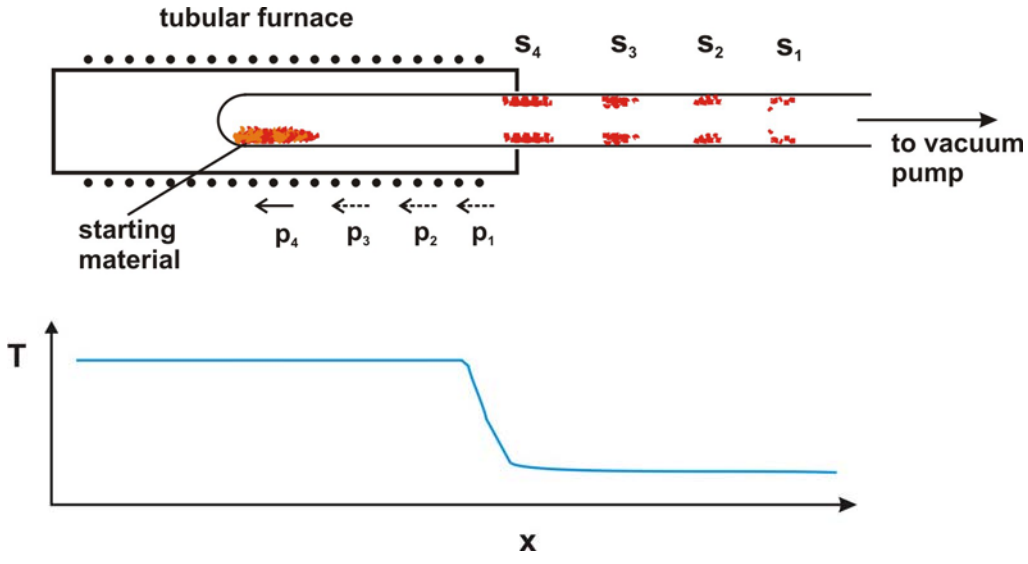

Figure 3.8 *Schematic of the step sublimation.*

Purification by gradient sublimation

A modification to step sublimation method, namely, fractional or gradient sublimation can efficiently separate the impurities with different sublimation temperatures. *Figure 3.9* shows the schematic of the gradient sublimation technique. The source material is again placed inside a quartz tube and subsequently the temperature is adjusted higher than the sublimation temperature of the host material. The temperature gradient extending over the tube is created by the controlled heating of the oven. An inert gas at a pressure, high enough to reduce the mean free path of the subliming molecules to stop them from reaching the tube walls and condensing, is produced inside the tube.

Due to the different sublimation temperatures, different impurities condense at the respective zone of appropriate temperature and therefore impurities which could not be removed by step sublimation method might be separated by the gradient sublimation.

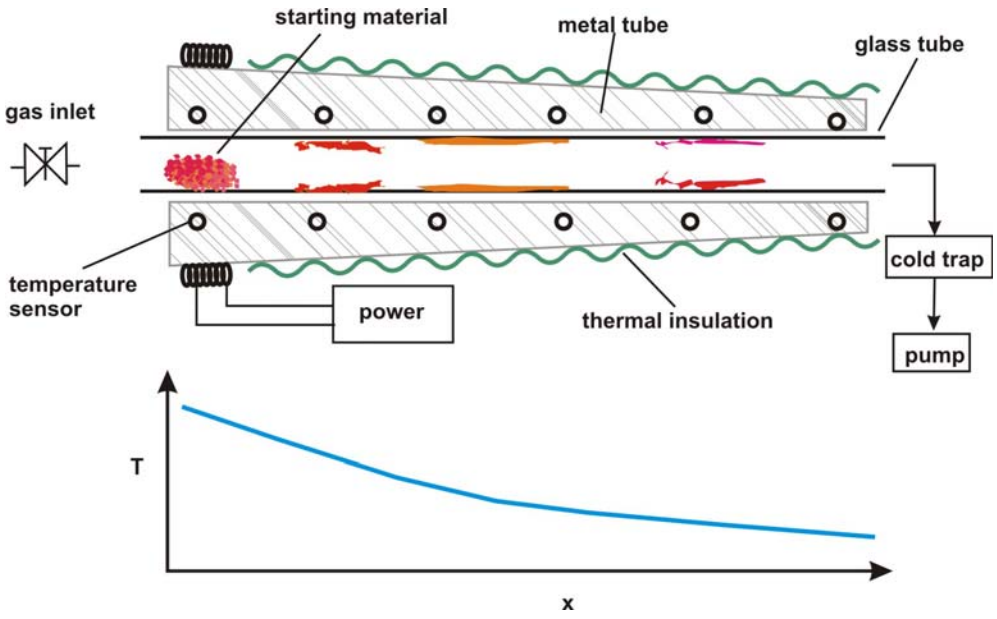

Figure 3.9 *Schematic of the gradient sublimation method.*

3.3 Delayed fluorescence and purity of the material

The triplet exciton lifetime, which depends on the diffusion of the triplet excitons in the material, is limited by impurities [100]. Only molecules with energy levels within the

excitonic or single charge carrier band gap lead to trapping and hence to triplet-triplet annihilation of the localized excitons. It has been shown in the past that multiple cycles of zone refinement result in ultra-pure material with very high triplet lifetimes, e.g. ~ 420 ms for naphthalene and ~25 ms for anthracene [99] and in accordance, such materials also exhibit very high charge carrier mobilities for electrons and holes, e.g. ~ 400 cm^2/Vs for holes in naphthalene at ~ 10 K [29]. The triplet exciton lifetime τ_{Tr} can be estimated by delayed fluorescence at low triplet excitation density where, after exciting the triplet states in the material by a laser pulse or a flash lamp in combination with an appropriate filter, the decay rate for mobile triplet excitons can be described by

$$-\frac{dT_1}{dt} = \beta T_1 + \gamma T_1^2 \qquad 3.3$$

where, β is the reciprocal of the triplet lifetime and γ is the bimolecular recombination rate constant.

In case of low exciton density,

$$\gamma T_1^2 \langle\langle \beta T_1 \qquad 3.4$$

from *equations 3.3 and 3.4* the triplet exciton density at any time *t* can be given by

$$T_1(t) = T_1(0)\exp(-\beta t) \qquad 3.5$$

Figure 3.10 shows the schematic of the triplet-triplet annihilation process resulting in the delayed fluorescence.

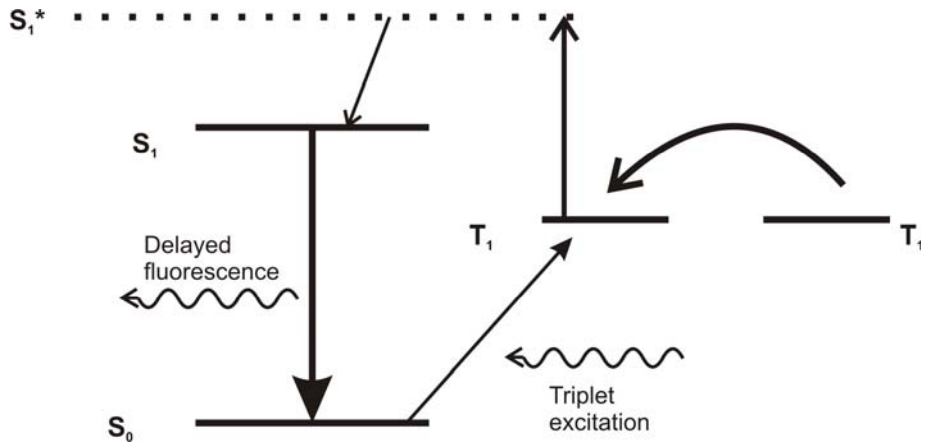

Figure 3.10 *Schematic of the triplet-triplet annihilation process.*

The delayed fluorescence is based on the triplet-triplet annihilation process in which two triplets recombine to form a super-excited singlet state S_1^* that relaxes to an excited single state S_1 by a non-radiative process. S_1 further relaxes to ground state S_0 via a radiative process. Therefore, the triplet-triplet annihilation process can be described by

$$T_1 + T_1 \rightarrow S_1^* \rightarrow S_1 \rightarrow S_0 + h\nu \qquad 3.6$$

The $S_0 \rightarrow S_1$ transition results in the fluorescence signal described by

$$\frac{dS_1}{dt} = \gamma T_1^2 \qquad 3.7$$

From *equations 3.5 and 3.7* it follows

$$S_1(t) \propto \exp(-2\beta t) \qquad 3.8$$

Therefore fitting the delayed fluorescence signal to a single exponential decay will provide the triplet lifetime.

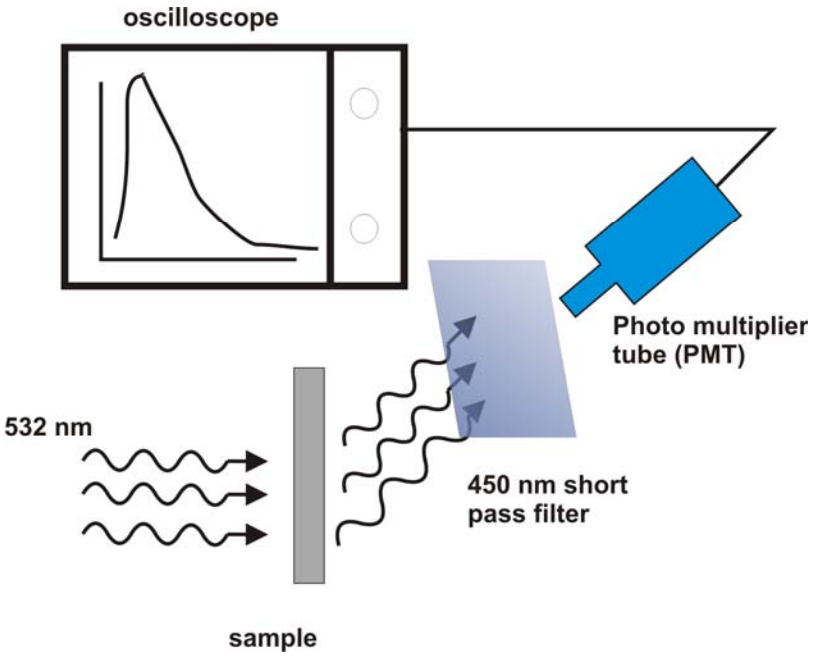

Figure 3.11 *Schematic of the experimental set-up for the measurement of the triplet lifetime.*

Figure 3.11 shows the schematic of the experimental set-up used for the estimation of triplet life time of the zone refined DPA.

The sample is illuminated by a laser pulse of 532 nm wavelength, which can excite only triplet states in case of DPA as for excitation of the singlet state of the DPA molecule a minimum wavelength of 395 nm is necessary as shown in the *figure 3.5*. The delayed fluorescence signal was filtered through a 450 nm short-pass filter in order to exclude signal from the direct relaxation of triplet to the singlet ground state. Afterwards, the delayed fluorescence signal is collected via a photo-multiplier-tube (PMT) recorded on a digital oscilloscope.

Figure 3.12(a) shows the delayed fluorescence signal for a purified portion of zone-refined DPA. Triplet lifetime as a function of distance from the top edge of the material column in the tube is shown in *figure 3.12 (b)*. To illustrate the position, an image of the tube with DPA, purified by 140 zone refinement cycles, has been put along with the *x-axis*.

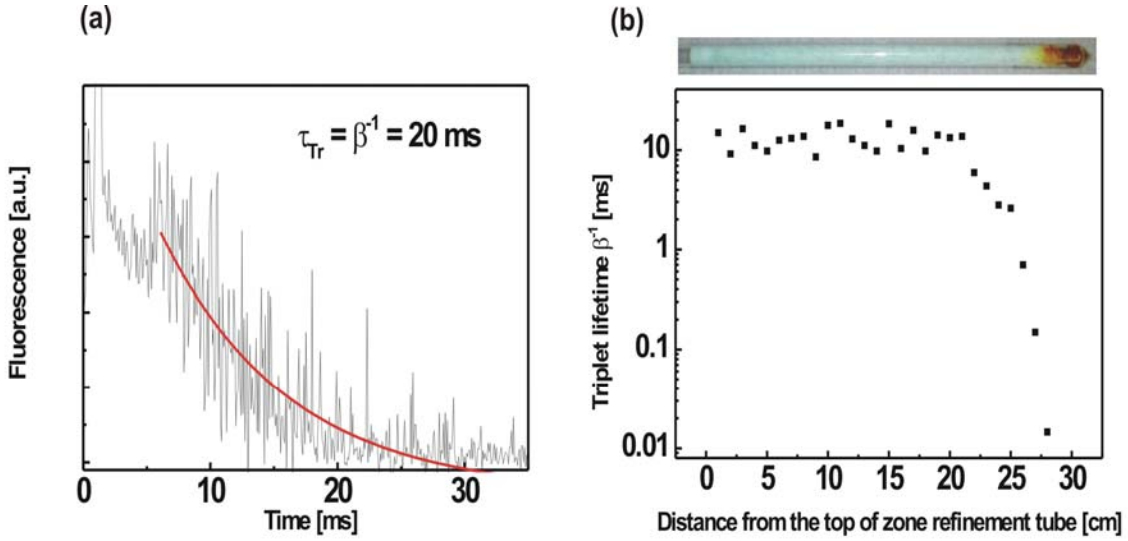

Figure 3.12 (a) *Delayed fluorescence signal for DPA purified by zone refinement. Red curve represents the fit to a single exponential decay process.* ***(b)*** *Triplet lifetime measured at various positions of the DPA zone-refinement tube. For illustration, an image of the tube is embedded in the figure at the same scale as the position assigned by the x-axis.*

The triplet lifetime drops drastically from ~ 20 ms in the purest material fraction in the middle of the tube to ~ 0.01 ms at the end of the tube where the material contains more chemical impurity (in this case the darker part of the tube). In case of DPA the triplet lifetime is in the range of ~ 0.01 ms to ~ 20 ms with the highest triplet lifetime in the middle of the zone refinement tube.

The lifetime the most purified DPA fraction is still shorter by more than an order of magnitude compared to ultra-high purified zone refined materials such as naphthalene (τ_{Tr} ~ 420 ms), which was purified by 900 zone refinement cycles, indicating that a certain amount of chemical impurities is still present in the material. However, purification of DPA is limited by the presence of certain chemical byproducts, e.g. diphenylanthrace-endoperoxide etc. which are very difficult to separate from the host material.

3.4 Crystal growth

3.4.1 Bridgman growth method

Brigdman growth is one of the most reliable techniques to grow bulk crystals of ultrahigh purity. This technique, introduced by Bridgman in 1925 [101], was earlier used for metals. However later this technique was successfully transferred to grow various organic crystals, e.g. naphthalene, anthracene, perylene etc.[99] One of the most important features of Bridgman growth is that the bulk organic crystals grown by this technique can be sawed along different crystallographic planes and hence render the possibility to estimate mobility tensors, as has been successfully demonstrated on anthracene, perylene and naphthalene[30].

Figure 3.13 shows the schematic of vertical Bridgman growth method. Bridgman growth is essentially a slow unidirectional cooling of the molten material with an initial seed formation in order to obtain a single crystal. A Bridgman furnace is consisting of two parts: an upper portion which is hotter than the melting temperature of the compound and a lower one which is colder. For organic compounds, the Bridgman ampoule is made of glass.

The Bridgman ampoule filled with the molten material can be slowly lowered in the temperature gradient or alternatively, the whole temperature gradient can be moved relative to the Bridgman ampoule. By moving an external reflector one can avoid the parasitic effects associated with the motion of the ampoule.

A single crystalline seed can either be placed in the lower part of the Bridgman ampoule in the beginning of the growth or a small amount of the solid polycrystalline material is placed in the lower stem of the ampoule. In the latter, the combined action of the capillary and the hollow sphere leads to the seed selection. Only the seed with the principal growth direction along the ampoule with survive and all other seeds will fade out. For a detailed study of the seeding process we refer to the literature [99].

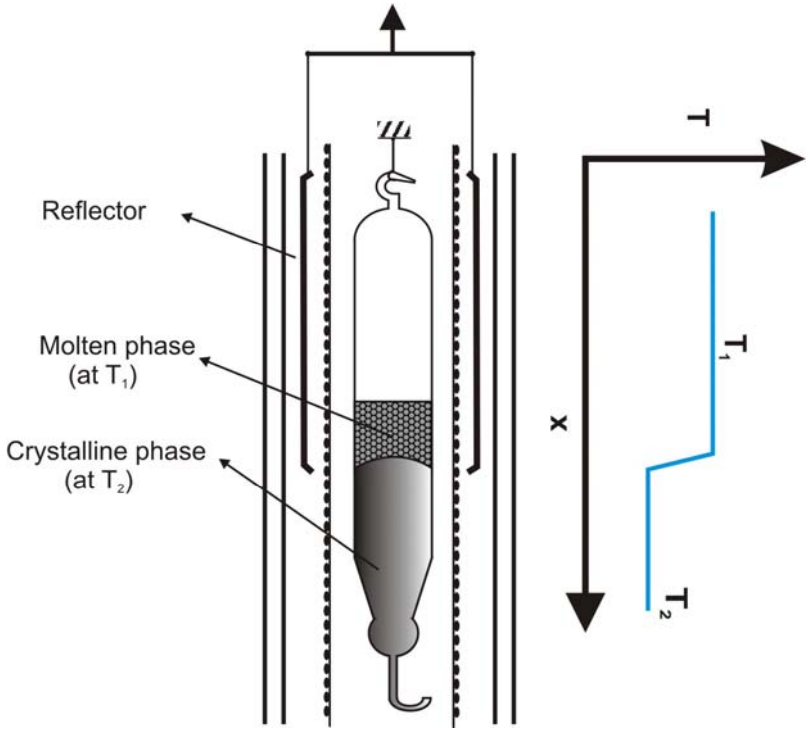

Figure 3.13 *Schematic of Bridgman growth method*

Bridgman crystals often stick to the glass of the ampoule and due to the different thermal expansion coefficients of glass and the material and the expansion anisotropy of the material. It might lead to considerable amount of stress induced crystal defects, e.g. dislocation lines. Density of these dislocation lines penetrating the surface can be

estimated by chemical etching [102]. For example, density of such dislocation lines obtained by the chemical etching ranges from 10^2 cm^{-2} for vapor-grown anthracene crystals, nearly 10^3 cm^{-2} for solution grown, to 10^6 cm^{-2} for melt grown anthracene crystals[102,103]. Therefore, though we can grow bulk crystals of ultra-high purity by this technique, structural defects induced during the growth might severely hamper the electronic transport properties. However, these structural defects can be reduced significantly by post annealing or by melting the crystals free from the wall of the ampoule for its most part before cooling down [104].

Bridgman grown DPA crystals

Figure 3.14 shows the optical image of a DPA crystal grown by the Bridgman method. Principal growth occurs in the *c'*-direction along the length of the ampoule, as it was verified by X-ray diffraction analysis.

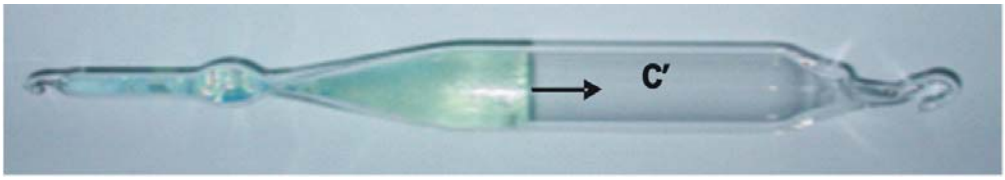

Figure 3.14 *DPA crystal grown by Bridgman method.*

The crystal was grown from zone refined material, purified by 140 zone refinement cycles, at a growth rate of 0.42 mm per hour. Grown crystal was slowly cooled down over a time span of 5 days. Crystal flakes or varying thicknesses between 0.9 mm to 1.2 mm were cut perpendicular to the surface normal by using a thread saw soaked with xylene. These flakes were further polished by using lens cleaning paper soaked with xylene in order to get smooth surfaces.

3.4.2 Growth from vapor phase transport

Organic compounds which decompose upon melting cannot be grown by melt, e.g. by usual Bridgman method. Moreover, crystal growth from solution or melt results in

relative higher density of structural defects, e.g. dislocation lines propagating up to the crystal surface, and hence is not best suited for FET measurements.

Growth from vapor phase results in crystals with smooth surfaces on which FETs can be successfully fabricated. Growth or organic crystals from vapor phase transport was first introduced by Laudise et. al and has been used to grow high quality crystals of many organic semiconductor compounds such as pentacene, tetracene, oligothiophenes etc.[105].

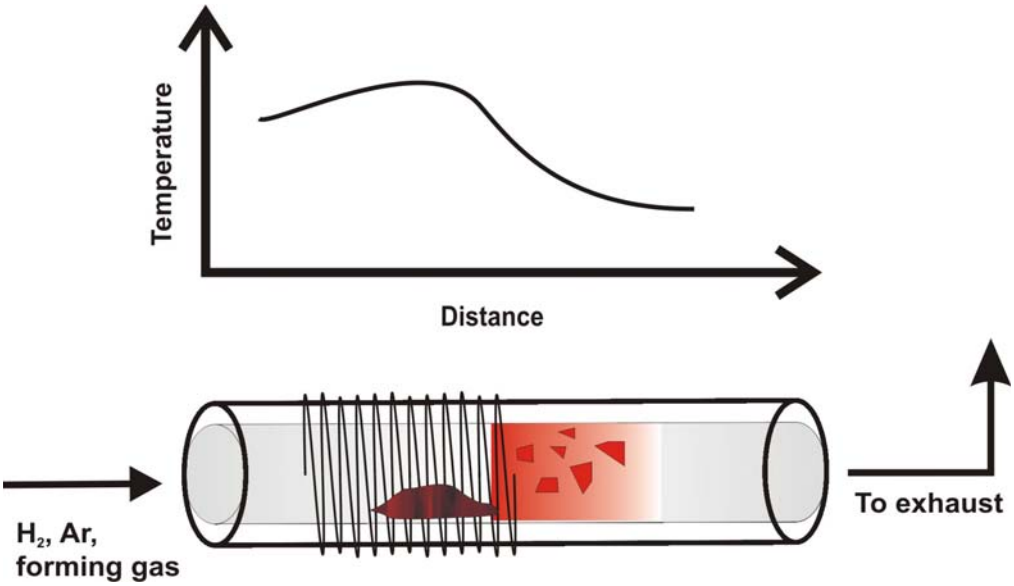

Figure 3.15 *Schematic of the vapor phase transport growth set-up.*

Figure 3.15 shows the schematic diagram of vapor phase transport growth setup. In this technique, source material is kept in a horizontal fused silica tube at a temperature slightly above its sublimation temperature. The crystal growth takes place as a consequence of physical transport of the vapor of source material to the colder zone where vapor of the respective material condenses forming crystals. The desired temperature gradient is achieved by the heating of a resistance coil wound around the tube. Growth is done within flowing H_2, Ar or forming gas. The gas flow is directed over the source material with a flow rate varying between 60 ccpm to 100 ccpm.[†] The vapor is physically transported by the gas flow and the crystal growth takes place in the region of the steepest temperature gradient.

[†]ccpm = cubic centimeter per minute

Velocity profile of the carrier gas at any point inside the tube is the combined effect of forced convection (essentially the flow rate) and the buoyancy driver convection (arising from the temperature gradient). In the region of the crystal growth, i.e. region with the steepest temperature gradient, the buoyancy term is dominated and we get a circulating convection flow facilitating the nucleation and growth of crystals. There are several advantages of this technique listed in the following:

1. This method needs very small amounts of source material (~ 100 mg) compared to other technique, e.g. Bridgman growth technique where we need nearly 3 – 5 g of material for the crystal growth.

2. It is a very fast process. The growth is usually finished within 48 hours whereas Bridgman growth needs 2 - 8 weeks depending on the material. Moreover, a self-purification process runs implicitly during the crystal growth.

3. Usually this technique has a very high yield and results in crystals with smooth surfaces which can be used for FET fabrication.

However, there are certain drawbacks of this technique, i.e. it is difficult to control the lateral dimensions and thickness of the crystals, the generation of structural defects due to the convection flow, and the incorporation of chemical by-products which have similar sublimation temperature. Nevertheless, vapor phase transport is meanwhile the most commonly used technique for the fast growth of organic semiconductor crystals.

DIP crystals grown by vapor phase transport

DIP crystals were grown from two times gradient sublimated DIP, by physical-vapor-transport technique in a temperature gradient under a streaming carrier gas at a flow rate of 100 ccpm. We used both H_2 and forming gas as carrier media yielding to similar structural and electronic properties of the crystals. The growth resulted in platelet like crystals with surfaces parallel to the *(ab)*-plane as verified by X-ray and shown in *figures*

3.16 (a) and (b). Most of DIP crystals shatter while cooling to the room temperature because of the stress generated due to the structural phase transition, which we shall discuss in detail in Chapter 5. *Figure 3.16 (c)* shows the micrograph of the surface of such a DIP crystal. Cracks are formed on the crystal surface due to the structural phase transition that crystals undergo during cooling. Origin of such defects shall be discussed later in Chapter 5.

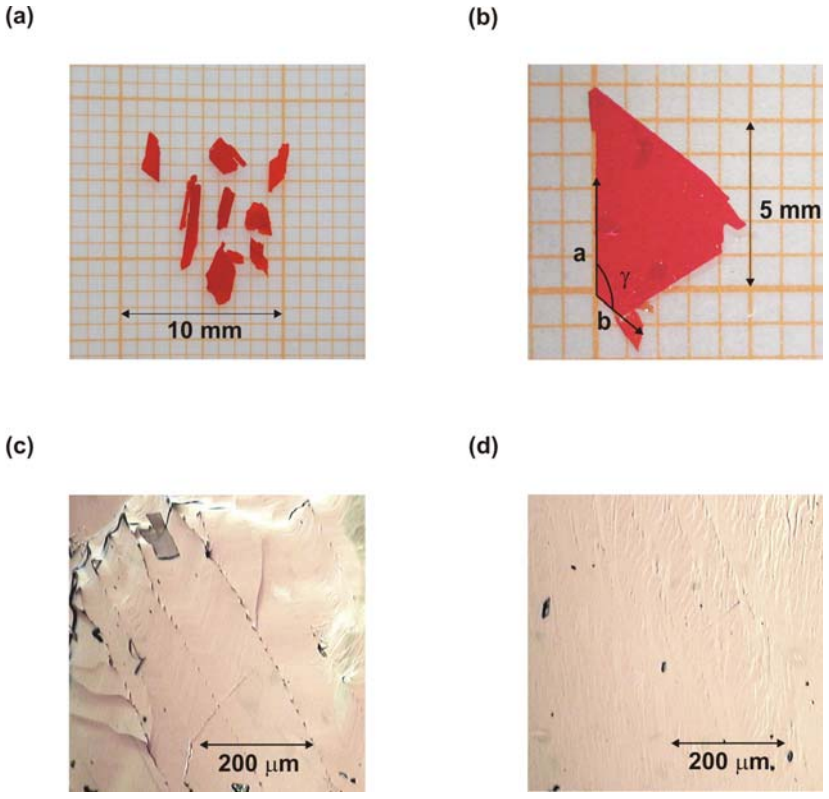

Figure 3.16 (a) *DIP crystals grown by vapor phase transport.* ***(b)*** *Magnified image of a DIP crystal with surface normal along c'-direction.* ***(c)*** *Micrograph of the surface of a DIP crystal with structural defects.* ***(d)*** *Micrograph of the surface of a DIP crystal with a relatively smooth surface.*

However, extremely slow cooling rates (~ 1 K/hr) result in crystals with lateral dimensions between 4×4 mm^2 to 7×7 mm^2 and the thickness varying between 20 μm - 50μm. Micrograph of the surface of a crystal of relatively high quality is shown in the *figure 3.16 (d)*.

DPA crystals grown by vapor phase transport

DPA crystals were also grown from vapor-phase-transport technique from the zone refined DPA (140 zone refinement cycles). *Figure 3.17* shows the DPA crystals grown by sublimation method. As demonstrated by *figure 3.17 (a)*, growth results in mostly needle shaped crystals. However, at faster growth rates (~ 5 hours for the complete growth) sometimes we get platelet shaped crystals with thicknesses between 50 – 200 μm and a lateral area of about 5 mm^2. *Figure 3.17 (b)* shows the magnified image of a platelet like crystal, whose edges resemble to the crystallographic *a*- and *c*- directions respectively and the surface normal along *b*-direction, as verified by X-ray measurements. Also the surface indicates a branched structure, as shown in the *Figure 3.17 (c)*. *Figure 3.17 (d)* shows the surface of a DPA crystal with relatively better quality.

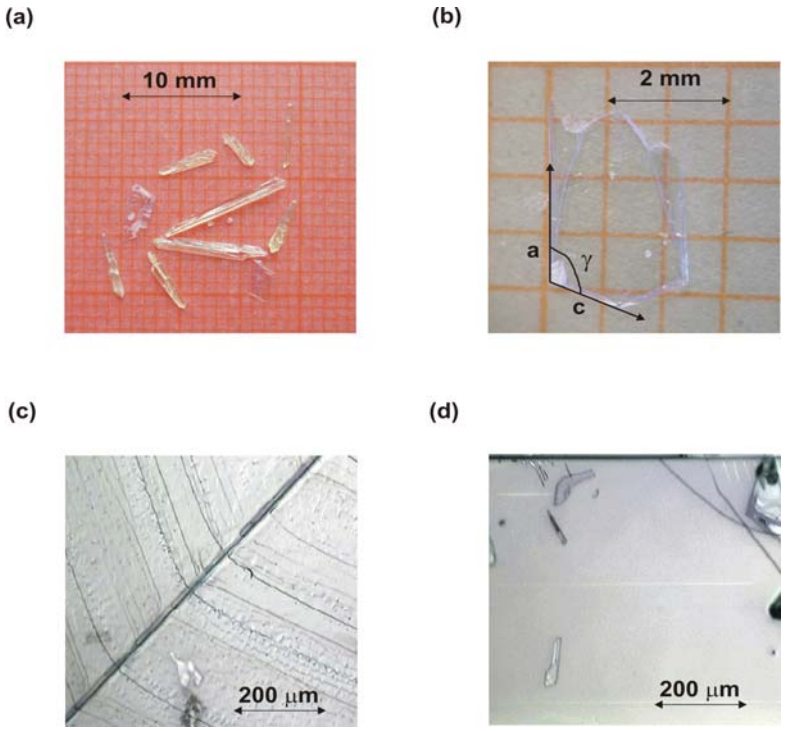

Figure 3.17 (a) *DPA crystals grown by vapor phase transport.* ***(b)*** *Image of a platelet like DPA crystal.* ***(c)*** *Branched structure on the surface of DPA crystals.* ***(d)*** *Optical micrograph of a relatively smooth surface.*

4 Experimental Methods

4.1 Methods for structural characterization

4.1.1 X-ray diffractrometry

X-ray diffractrometry was used for the structural characterization and orientation of the crystallographic directions for TOF measurements. For detailed information about X-ray diffraction analyses we refer to the literature [106,107]. In this section only the relevant theory will be discussed.

Principle of Bragg diffraction:

Bragg diffraction pattern were obtained by out-of-plane X-ray diffraction under Bragg-Brentano (θ - 2θ) geometry. *Figure 4.1* shows the schematic of the Bragg diffraction principle.

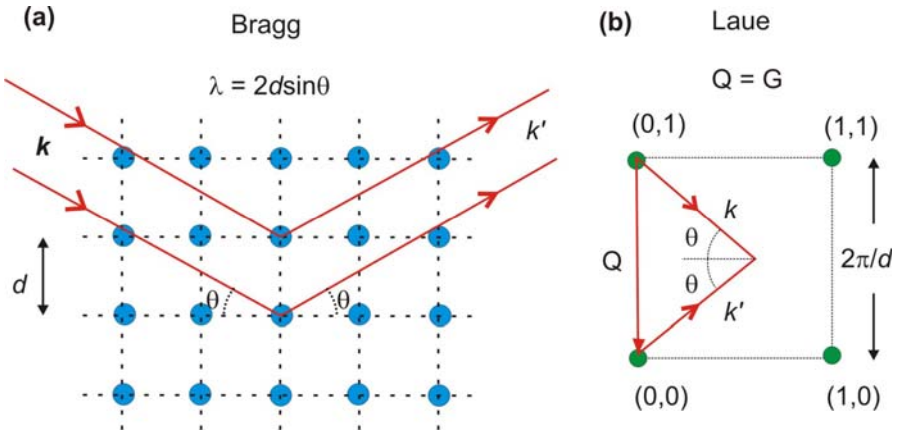

Figure 4.1 *Principle of Bragg diffraction* ***(a)*** *in real space and* ***(b)*** *in reciprocal space.*

X-rays, due to their wavelengths of same order as the lattice spacing in crystals, are diffracted by the lattice planes and interfere constructively when the X-ray beams diffracted by a set of adjacent lattice planes have a phase difference of multiple of 2π. This condition for Bragg peak can be formulated as

$$2d_{hkl}\sin\theta = n\lambda \qquad 4.1$$

where d_{hkl} is the lattice spacing between (*hkl*) planes, θ is the scattering angel, λ is the wavelength of the monochromatic X-ray source and n is the order of the Bragg peak. *Equation 4.1* is known as *Bragg's law* and gives the condition for the scalar description of the Bragg peaks.

Alternatively, the *Laue condition* provides the vector description of the X-ray diffraction pattern. As shown in the *figure 4.1 (b)*, this condition states that, in case of elastic scattering, the wavevector transfer defined by $Q = k' - k$ should be equal to the reciprocal lattice vector G for constructive interference. i.e.

$$Q = G \qquad 4.2$$

where,

$$|Q| = \frac{4\pi}{\lambda}\sin\theta \qquad 4.3$$

and

$$|G| = \frac{2\pi}{d_{hkl}} \qquad . \qquad 4.4$$

Equivalence between *Bragg's law* and *Laue condition* could be obtained by replacing Q and G from *equations 4.3 and 4.4*.

Intensities of the Bragg reflections

Scattering produced by a crystal is due to the interaction between incident X-rays and electrons. Therefore the density of the scattering material can be related to the electron density at that point. Since the electron density varies for different atoms, we have to

define an *atomic scattering factor* f_i for the atoms constituting the unit cell. The amplitude of the X-rays scattered by each atom in a unit cell is proportional to its atomic scattering factor yet we cannot predict the resulting scattering amplitude for the whole unit cell until we know the phase of the X-rays scattered by each atom. However, if we fix the origin of the unit cell as reference point of the phase, then the phase of the X-rays scattered into (*hkl*) reflection by an atom located at a point *xyz* is given by

$$\Delta\phi = 2\pi \frac{D_{hkl}}{d_{hkl}} \qquad 4.5$$

where D_{hkl} is the distance from the origin to the plane parallel to (*hkl*) passing through *xyz* and d_{hkl} is the lattice spacing corresponding to the (*hkl*) plane. The intensity of the X-rays scattered by one unit cell of a crystal can be given by,

$$I(hkl) = \left(\sum_{1}^{N} f_n \cos\phi_n \right)^2 + \left(\sum_{1}^{N} f_n \sin\phi_n \right)^2 \qquad 4.6$$

where f_n is the atomic scattering factor corresponding to the n^{th} atom in the unit cell and ϕ_n is the phase shift associated with the n^{th} atom. N is the total number of atoms in the unit cell.

In other words, we can define a *structure factor F(hkl)*, described by

$$F(hkl) = \sum_{1}^{N} f_n \exp 2\pi i(hx_n + ky_n + lz_n) \qquad 4.7$$

where (x_n, y_n, z_n) are the coordinates of the n^{th} atom in the unit cell and (*hkl*) the respective plane of reflection. Now the amplitude of the resulting reflected wave is proportional to $\left|F(hkl)\right|$, and known as the *structure amplitude*. Therefore, the intensity of the X-rays scattered by one unit-cell into the (*hkl*) reflection can be described by

$$I(hkl) = \left|F(hkl)\right|^2 \qquad . \qquad 4.8$$

One can see that the *equation 4.8* is identical to the *equation 4.6*.

Experimental set-up

Figure 4.2 shows the schematic diagram of the experimental set-up. We have used a Siemens Kristalloflux equipped with a *Cu*-tube providing *Cu-Kα* radiation at ~ 1.54237 Å. Measurements were performed in θ - 2θ geometry to determine the out-of-plane crystallographic direction of samples used for electrical characterization. Set-up is provided with four slits which are used to collimate the X-ray beam and also for adjusting the intensity of reflected X-rays into the detector.

The set-up enables us to estimate the sample thickness (by Kiessig oscillations), lattice spacing (by peak position), crystallite size (by Bragg peak width) and crystallinity or texture of the sample (by rocking curve). However, in case of crystals it is not possible to obtain Kiessig oscillation due to large thickness of the samples (> 10 μm) and thereby the corresponding oscillations can not be resolved by our set-up. Therefore, we shall discuss only the features observed in a typical Bragg spectrum for organic crystals.

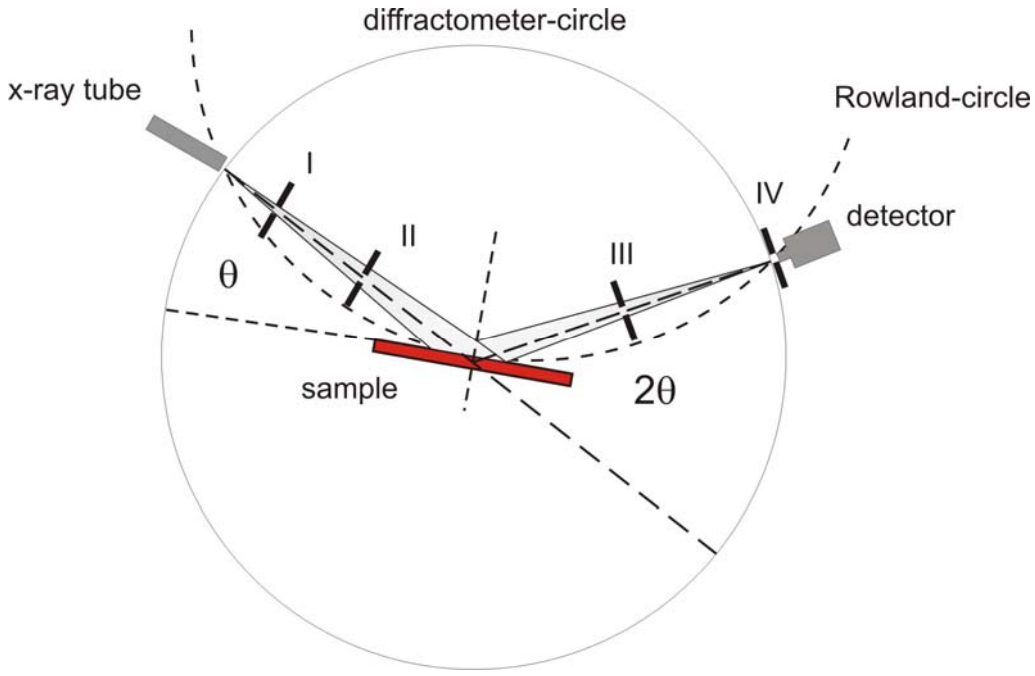

Figure 4.2 *Schematic representation of X-ray set-up [28].*

Crystallite size from the Bragg peak

The crystallite size along the out of plane direction can be calculated from the width of the Bragg reflections. The broadening of the Bragg peaks is related to relative phase differences occurring by the reflections from the grain boundaries. Crystallite size corresponds to the size of a coherently diffracting domain. Presence of dislocation lines etc. might also lead to the broadening of Bragg peaks. Scherrer first observed that the finite crystallite size leads to the broadening of the Bragg peak and he derived the equation relating full-width-at-half-maximum (FWHM) of the Bragg peak at 2θ to the crystallite size, which is also known as Scherrer formula [108]

$$\Delta\theta = \frac{0.9\lambda}{B\cos\theta} \qquad 4.9$$

where $\Delta\theta$ is the FWHM in radians and B is the crystallite size.

Estimation of the crystallite size from the Scherrer formula is limited by geometrical factors e.g. angular resolution and beam divergance as well as factors such as broadening caused by dislocations etc. Due to such limits crystallite sizes larger than 2000 Å can not be estimated accurately in our set-up.

Rocking curve

Rocking curve measurements were performed to study the tilting of the crystallites. Rocking curve measurements are performed via a α scan around the fixed 2θ Bragg peak position, as shown in the *Figure 4.3*. In other words, the sample is *rocked* over a small angular range α. A detailed rocking curve analyses give information about various structural properties, e.g. twist and tilt angles of crystallites. The width of the rocking curve is directly proportional to the average tilting of the crystallites and therefore the rocking curve measurements are signatures of the texture of crystals or thin films.

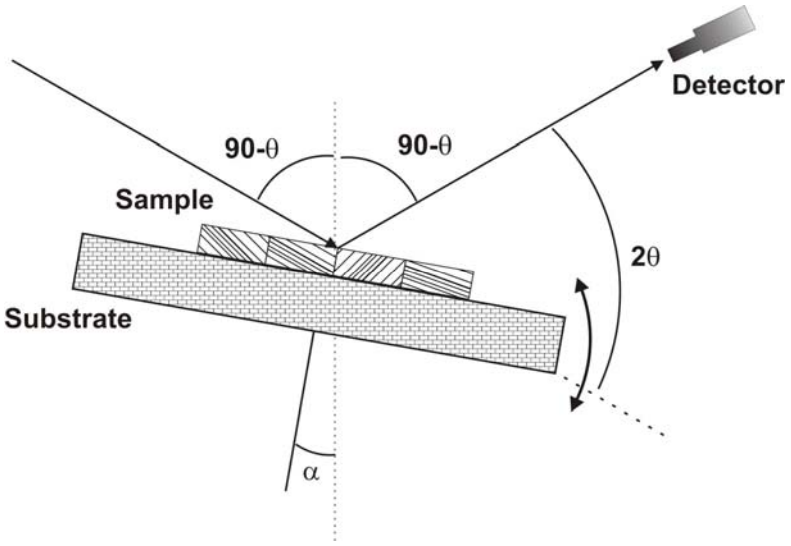

Figure 4.3 *Schematic of rocking curve measurement.*

4.1.2 Single crystal diffractrometry

Lattice parameters for DIP and DPA single crystals were performed in collaboration with Dr. T. Siegrist at Bell Laboratories, Lucent Technologies. Structural characterization was performed for these crystals in the temperature range of 110 K – 423 K, using an *Oxford Diffraction Xcalibur 2* diffractometer equipped with CCD camera and cryojet temperature controlled system. The diffractometer uses *Mo-Kα* wavelength at ~ 0.7107Å.

4.2 Methods for electronic characterization

4.2.1 Time-Of-Flight (TOF)

TOF is one of the techniques by which we measure the mobility of photo-generated charge carriers in a given material. This is the most direct way of measuring the velocity and hence the mobility of charge carriers in semiconducting materials. This technique was first described by Hayens and Schokley [109] and Kepler [110] and LeBlanc [111] first applied TOF technique to study organic solids. Over the time this technique has been used to estimate the mobiliy of charge carriers in numerous organic and inorganic semiconductor compounds.

Principle of TOF

TOF is based on the measurement of the drift velocity of photo-generated charge carrier under the presence of an external electric field in a semiconducting material. A schematic of the TOF set-up is shown in the *figure 4.4*. The sample under study is sandwiched between two conducting electrodes and the front face of the sample is illuminated by a pulsed laser in single shot mode to generate bound electron-hole pairs near the surface of the front electrode in the semiconductor material. In the presence of an external field, these electron-hole pairs are dissociated at the front electrode, resulting in a charge carrier sheet near the surface, which travels across the sample under the influence of the external field, resulting in a displacement current, which could be recorded as a voltage drop across the load resistor by an oscilloscope.

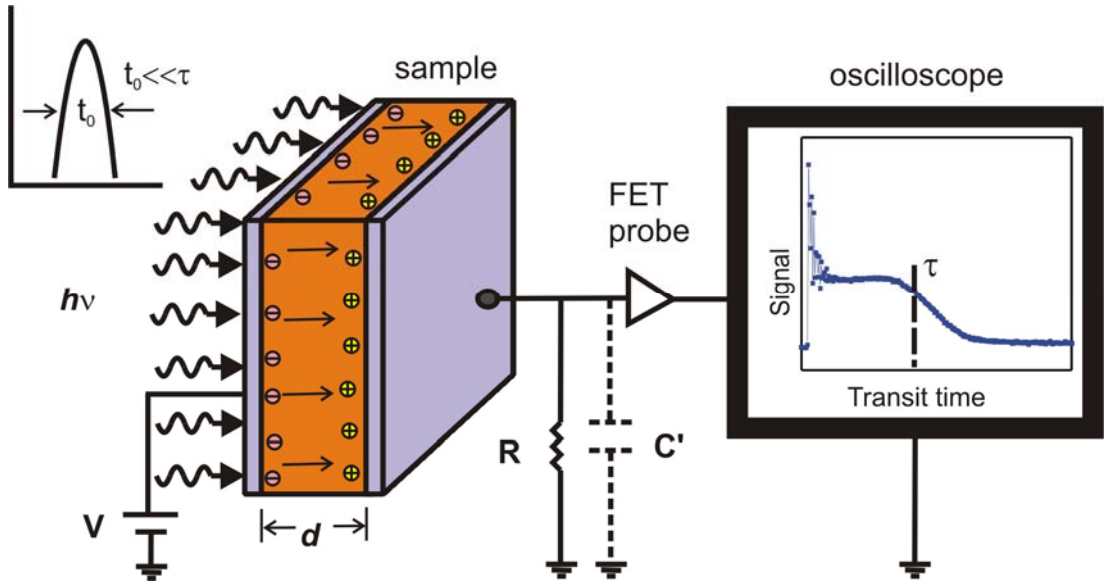

Figure 4.4 *Schematic representation of the Time-Of-Flight method.*

Length of this current pulse corresponds to the time needed for charge carriers to travel across the sample and hence enables to estimate the mobility of charge carriers by the following formula

$$\mu_{eff} = \frac{d^2}{\tau V} \quad . \qquad 4.10$$

Where μ_{eff} is the effective mobility of the respective charge carriers (electrons or holes), d is the thickness of the sample, τ is the duration of the current pulse, and V is the applied voltage. TOF has two major advantages compared to the injection based measurement techniques, e.g. FET, SCLC etc.

1. TOF is a charge injection free method, which means there is no requirement of injecting the charge carriers into the sample by electrodes. In this technique, charge carriers are photo-generated in the material by using a suitable light pulse source. This avoids the problem of injection barriers and contact effects, especially in organic semiconductors.

2. Another major advantage of this technique is that the mobility of both electrons and holes can be measured independently by changing the polarity of the external voltage. Current-voltage measurement methods need the injection of both electrons and holes into the material in order to estimate the respective mobility which is found to be a tedious task because of the mismatch between metal Fermi level and HOMO and LUMO levels of semiconductors.

Requirements of the technique

There are certain requirements, which must be met to confirm the applicability of this method. These requirements are explained in the following

1. Charge carriers must be generated near the surface of the front electrode in order to clearly distinguish the transit time. According to the Beer-Lambert's law, the intensity of the light pulse inside the sample attenuates as $\sim exp(-\alpha x)$ where α in the absorption coefficient and x is the distance from the illuminated surface. In order to get a distinguishable transit kink most of the charge carriers must be generated within 10% of the sample thickness which demands for a high absorption coefficient in the material for the incident wavelength or thick samples.

2. The amount of charges generated has to be small enough so that the effect of space charging does not change the internal field significantly. This will hold true as long as the photo-generated charge Q_0 satisfies the condition

$$Q_0 << CV \qquad 4.11$$

where C the sample capacitance.

Also, the shape of the leading edge of the pulse can broaden due to the Coulomb repulsion among the carriers during the transient. It has been shown that the error in the transit time due to this process is $\Delta t/\tau \approx Q_0/CV$ [112]. However, Q_0 should be large enough to give a reasonable signal to noise ratio, which requires an optimal intensity of the laser pulse for a suitable TOF signal.

3. Another important condition for the TOF analysis is that circuit time constant $\tau = RC$ must be smaller than the average drifting time of the charges. Where R is the external resistance across which the voltage drop caused by the displacement current is collected and C is the total circuit capacitance. A small time constant can be realized by choosing small R. But there is a lower limit of R defined by the adequate signal to noise ratio to obtain a distinguishable transit kink in the TOF signal. As the sample capacitance is proportional to the contact area and inversely proportional to the sample thickness, a small C can be achieved by choosing high thicknesses and small contact areas. But again, smaller contact areas would result in smaller Q_0, which leads to a poor signal to noise ratio. Also, a thick sample would lead to more traps in the sample and hence broadening and blurring the actual TOF pulse.

4. The dielectric relaxation time $t'_0 = \varepsilon\varepsilon_0/\sigma$ has to be long compared to the transit time with σ being the dark conductivity. This is the time required for an insulator to restore itself to the state of charge neutrality after a small change in the charge population. The intrinsic concentration of charge carriers is very small for materials with small dielectric relaxation time. Organic solids have dark conductivities in the range of $\sim 10^{-15}\ \Omega^{-1}m^{-1}$ and a dielectric constant of ~ 3 which leads to $t'_0 \sim 3\times10^4$ s. Therefore this condition is fulfilled for most of the organic materials.

5. The sample should be plane parallel in order to obtain a flat plateau and a distinguishable transit kink. A wedge shaped sample would give a blurred signal and estimation of the transit time will be erroneous.

Effect of traps and space charging on TOF pulses:

In the ideal case when the entire photo-generated charge carriers move in a thin sheet, the transient current pulse should display a rectangular signal if the circuit time constant is negligible compared to the transit time. But in reality pulse shapes often deviate from an ideal rectangular due to the various factors such as space charging by excess photo-generation of charge carriers compared to the capacitive limit of the sample, circuit time constant *RC*, and charge carrier traps etc. *Figure 4.5* shows the effect of space charging and deep and shallow traps on the TOF current pulse.

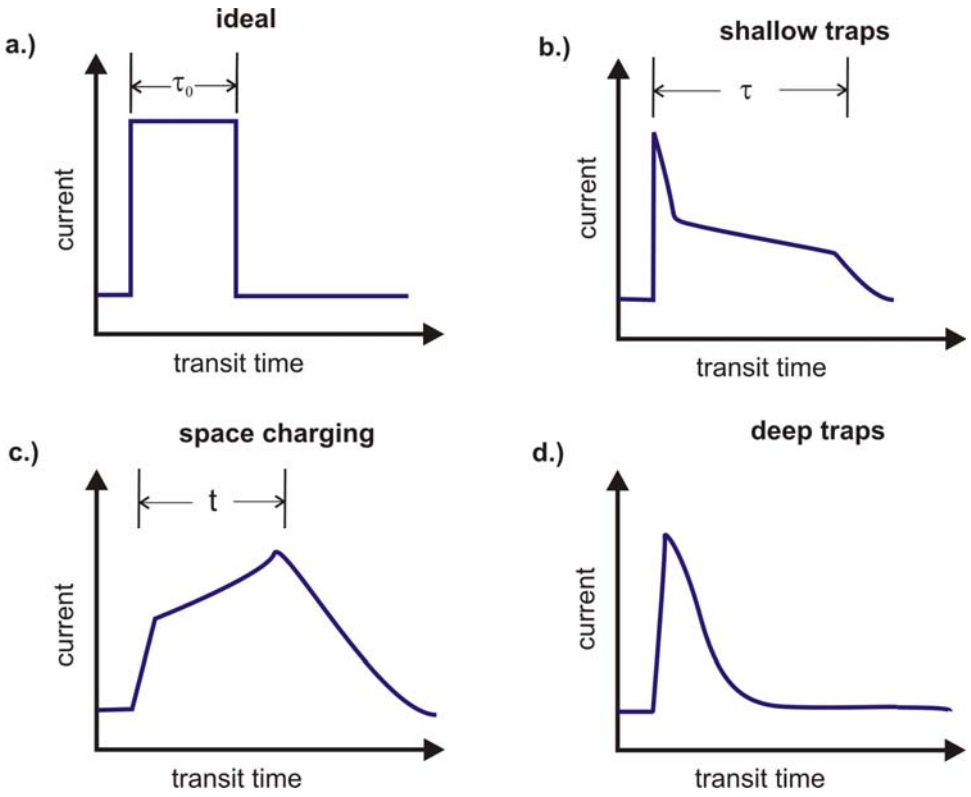

Figure 4.5 (a) *An ideal TOF pulse.* ***(b)*** *Effect of shallow traps: elongated TOF pulse.* ***(c)*** *Effect of space charging.* ***(d)*** *Effect of deep traps.*

Figure 4.5 (a) shows an ideal TOF pulse, rectangular in shape, which can be obtained only in the trap free case. In this case photo-generated charge carriers are drifted in transport bands under the influence of external electric field without being trapped and the intrinsic mobility can be directly calculated from *equation 4.10*.

Figure 4.5 (b) shows the effect of shallow traps. In this case, charge carriers are trapped by shallow traps and released within the transit time by the thermal energy. Therefore it results in a longer TOF pulse compared to the trap free case and *equation 4.10* provides the effective mobility.

Figure 4.5 (c) shows the effect of the space charging on the TOF pulse. In this case, charge carriers accumulate to form a charge reservoir because of the low mobility and thereby enhance the effective electric field in which charge carriers are accelerated and result in a time dependent space-charge-limited-current (SCLC) [113]. In the case of trap-filled-space-charging, the time dependent transient current can be described by [114]

$$I(t) = \frac{1}{2} I_{stat} \left[1 - \left(\frac{t}{2\tau} \right) \right]^{-2} \qquad 4.12$$

where I_{stat} is the stationary state SCLC given by

$$I_{stat} = \frac{9}{8} \varepsilon \varepsilon_0 \mu \frac{V^2}{d^3} \quad . \qquad 4.13$$

It can be derived from the *equation 4.12* that *I(t)* reaches a maximum value at $t = 0.79\tau$. Therefore, the calculated mobility should be multiplied by a factor of 0.79 in order to estimate the effective or intrinsic mobility.

Figure 4.5 (d) indicates how deep traps affect the TOF pulse. Charge carriers in deep traps are not able to be released by the thermal energy and therefore result in a rapid decay of the signal. In case all the charge carriers are trapped within the measurement time, no kink can be detected and the behavior is called totally dispersive transport.

Experimental setup

The TOF sample holder is mounted in a high vacuum chamber connected with a bipolar Keithley 246 high voltage supply with an output range of 0 – 3000 V and a Newtronic

temperature controller. The TOF current pulse is recorded as a voltage drop across the load resistance, which can be varied between 40 Ω - 1MΩ, by a high resolution Tektronix TDS3032 digital oscilloscope (50 Ω input resistance and 300 MHz bandwidth) through a Tektronix P6201 FET probe (DC to 900 MHz bandwidth and 100 KΩ impedance shunt with 3 pF capacitance). The TOF chamber is connected to a diffusion pump and a N_2 cylinder in order to perform measurements either in vacuum (~10^{-5} Torr) or under N_2/ambient conditions.

Figure 4.6 shows a schematic diagram of the TOF setup. A laser pulse of suitable wavelength is generated by using a N_2 laser with wavelength of 337 nm and a pulse width of ~ 0.76 ns or an Nd-Yag laser which can work on multiple frequency modes to provide wavelengths of 266 nm, 355 nm, 532 nm and 1064 nm with a pulse width between 2 - 6 ns. A beam splitter is used to trigger the oscilloscope via a photo-diode with the laser pulse and grey filters can be used to adjust the intensity of the laser pulse. External electric field is applied by the Keithley voltage source and the temperature of the sample can be controlled by the Newport temperature controller (295 K – 470 K). Low temperature measurements are performed in a flow cryostat in which it is possible to cool down the sample to liquid helium temperature (~ 4 K).

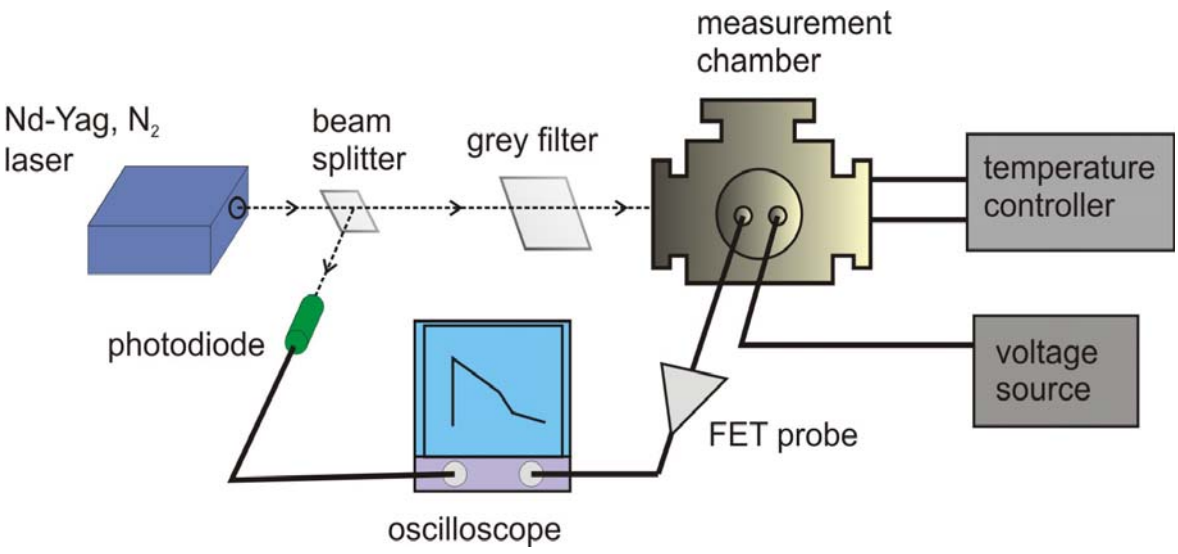

Figure 4.6 *Schematic representation of TOF set-up.*

Sample preparation

Samples were prepared for the TOF measurements by thermal evaporation of a semi-transparent silver layer of about 20 nm thickness as front electrode for low vapor pressure materials such as diindenoperylene (DIP) and diphenylanthracene (DPA). The thickness of the silver layer was estimated by X-ray reflectivity measurements on a separate reference sample (cover glass). Front electrode must be semi-transparent for the incident laser wavelength to generate a sufficient amount of charge carriers in the sample. Back electrodes were also prepared by thermal deposition of silver, but in this case the thickness is not critical for TOF measurements. *Figure 4.7* shows the TOF sample holder. The crystals are glued on a copper disk, which serves as a back electrode as well as a heat stage. These copper disks are mounted on the sample holder, which could be heated by a halogen lamp up to 475 K. A cromel-aluminium thermocouple (275 K – 875 K) is mounted on the sample holder to measure the temperature. Electrical feed-throughs are provided to apply an external bias and to collect the TOF the signal.

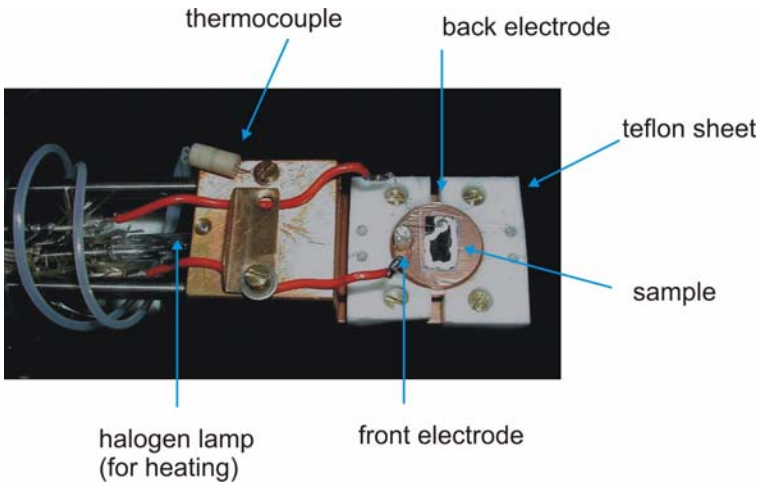

Figure 4.7 *Sample holder with a mounted crystal for TOF measurements.*

4.2.2 Space charge limited current (SCLC) measurements

SCLC studies are current-voltage (*I-V*) measurements which enable us to estimate various parameters such as mobility, trap density, trap depth etc. SCLC measurements

can be performed across the bulk (sandwiched geometry) as well as in-plane (surface geometry). *Figure 4.8 (a) and (b)* show the schematic drawings corresponding to the SCLC geometry in sandwich and surface configurations respectively.

Space charge limited current means that the density of free carriers injected into the organic semiconductor above a certain applied voltage becomes larger than the number of transport levels accessible in the material. Because of the low mobility of the charge carriers, they accumulate in the sample near the injection electrode and form a build-in potential which opposes the injection of further carriers at the contact electrodes as well as enhances the effective electric field.

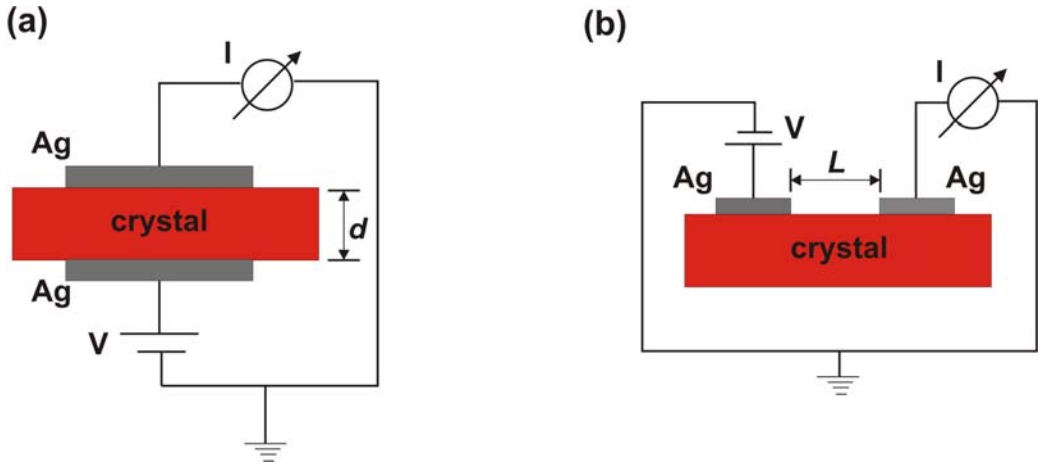

Figure 4.8 *Schematic drawings of the SCLC measurements in* ***(a)*** *sandwich and* ***(b)*** *surface configuration.*

For one type of charge carrier injection (i.e. either electrons or holes), the electric field inside the sample follows the Poisson's equation described by [115]

$$\frac{dE(x)}{dx} = \frac{\rho_{tot}}{\varepsilon\varepsilon_0} \qquad 4.14$$

where $\rho_{tot} = \rho_{free} + \rho_{trap}$ is the total charge density of injected free and trapped charge carriers. Considering hole transport, the current density can be written as

$$J = e\mu_p p(x)E(x) \qquad 4.15$$

where μ_p is the hole mobility and *p(x)* is the density of free holes. For a trap-free case, $\rho_{trap} = 0$ and from *equation 4.14* and *4.15* we can derive

$$2E(x)\frac{dE(x)}{dx} = \frac{d[E(x)]^2}{dx} = \frac{2J}{\varepsilon\varepsilon_0\mu_p} \quad . \qquad 4.16$$

Integrating *equation 4.16* and using the boundary condition

$$V = \int_0^d E(x)dx \qquad 4.17$$

we yield a current density in the trap-free SCLC region described by

$$J_{SCLC} = \frac{9}{8}\varepsilon_0\varepsilon_r\mu\frac{V^2}{d^3} \quad . \qquad 4.18$$

Equation 4.18 is also known as Mott-Gurney law [116]. In case of a sample with single or discrete trap levels, *equation 4.18* is modified as

$$J_{SCLC} = \frac{9}{8}\varepsilon_0\varepsilon_r\mu\frac{V^2}{d^3}\Theta \qquad 4.19$$

where Θ is the ratio of free carrier density ρ_{free} and the total carrier density ρ_{total}

$$\Theta = \frac{\rho_{free}}{\rho_{total}} \quad . \qquad 4.20$$

Once all trap states are filled, the *I-V* behavior is similar to the trap-free case and the mobility can be extracted by using *equation 4.18*.

In case of surface geometry, as shown in *figure 4.8 (b)*, the current density for SCLC regime has to be modified and is given by [117],

$$J_{SCLC} = \frac{2}{\pi}\varepsilon_0\varepsilon_r\mu\frac{V^2}{L^2} \qquad 4.21$$

where *L* is the distance between the electrodes.

Mobility shows cubic dependence on the sample thickness in sandwich geometry whereas it exhibits quadratic dependence on the channel length in case of planar geometry, as it is evident by *equations 4.18 and 4.21*. Applying the sandwich geometry formula to the planar SCLC data might result in overestimation of the mobility. For

example, applying *equation 4.18* for the surface geometry SCLC data obtained on a sample with 100 μm channel length would result in an overestimation of the mobility by almost two orders of magnitude. Therefore, a careful approach is needed for SCLC data analysis, which otherwise might result in deviations from the real values [118].

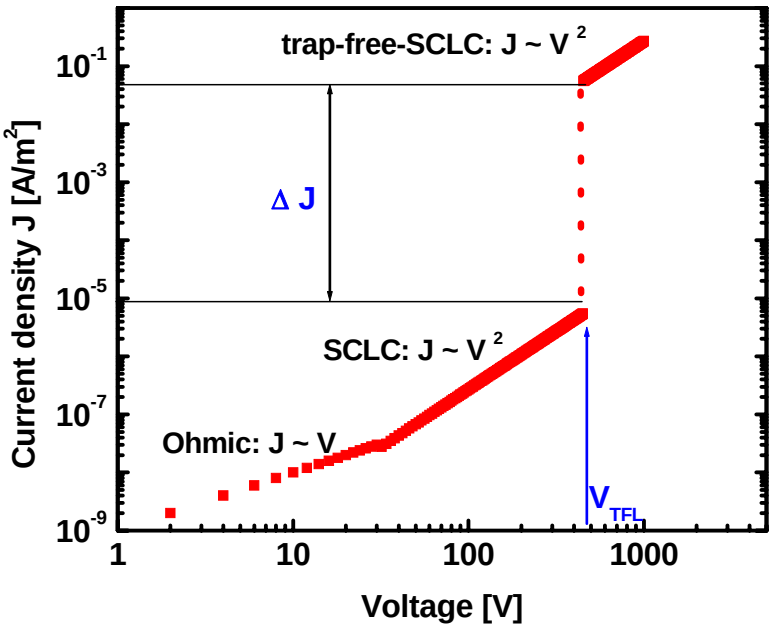

Figure 4.9 *J-V characteristic for a typical SCLC measurement on a sample containing a single trap level.*

Figure 4.9 shows the schematic representation of a typical *J-V* characteristic for low a mobility semiconductor with a single trap level. Initially, the current follows an Ohmic behavior (linear increase with voltage), in this case the density of thermally generated free charge carriers inside the sample is dominating the transport and charge carrier accumulation does not play a significant role. However, continuously increasing the charge carrier injection, the transport is now limited by the electric field generated by the space charges and the current can be described by *equation 4.19*.

Upon further increase in the applied voltage charge carriers get trapped into the trap states and once all trap states are filled, which corresponds to trap-filled-limit voltage

V_{TFL}, one observes a strong jump in the current ΔI by several orders of magnitude. V_{TFL} is related to the density of deep traps $N_{t,d}$ by

$$V_{TFL} = \frac{N_{t,d} e d^2}{\varepsilon_r \varepsilon_0} \quad . \qquad 4.22$$

The relative jump in the current is related to the characteristic energy for deep traps $E_{t,d}$ by

$$\frac{\Delta J(V_{TFL} + \Delta V)}{\Delta J(V_{TFL} - \Delta V)} = \frac{N_{t,d}}{N_0} \exp\left(\frac{E_{t,d}}{k_B T}\right) \quad . \qquad 4.23$$

Due to various discrete trap levels and large density of deep traps in organic semiconductors, often the trap-free limit is not reached and the mobility estimated from the *equation 4.18* describes the lower limit of the mobility μ_{min}.

4.2.3 Field-effect-transistor (FET) method

An FET consists of an active transport layer formed by the organic semiconductor, source and drain electrodes for injection of charge carriers into the active layer and collection of output current respectively. By an insulator with a gate electrode the number of charge carriers, which forms the accumulation layer in the transport channel, is controlled. *Figure 4.10* shows the schematic of a FET based on an organic crystal.

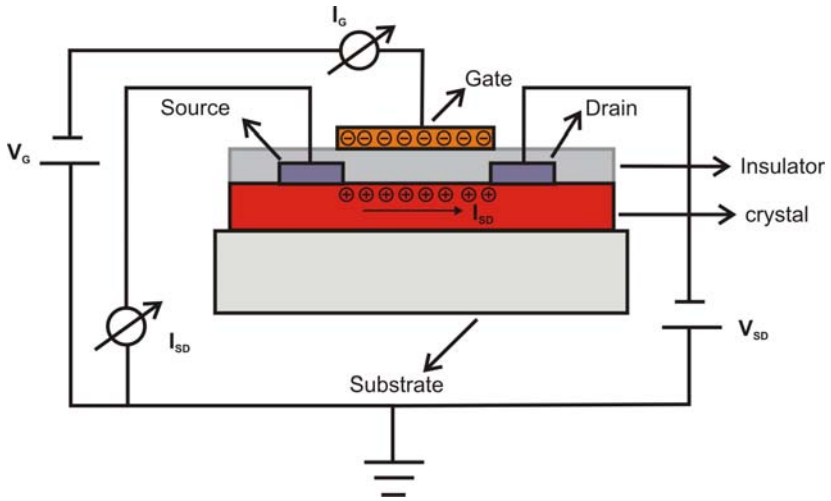

Figure 4.10 *Schematic of the Field-Effect-Transistor geometry prepared on top of an organic single crystal.*

Principle of OFET operation

Fundamental principles and applications of OFETs are based on conventional semiconductor MOSFETs (Metal-Oxide-Semiconductor Field-Effect-Transistors). OFETs show deviations from standard MOSFET behavior due to, i.e. metal organic interface dipoles [119], contact resistance [120] and semiconductor-insulator interface states [121] strongly affect the FET characteristics, yet this approach provides useful information about the OFET operation.

I-V characteristics of unipolar Field-Effect-Transistors can be divided into three regimes, namely *cut-off or sub-threshold*, *linear or triode*, and the *saturation* regime. In the *cut-off* regime ($|V_G| < V_{th}$), there is no conduction in the transistor and the FET is called to be in the *OFF* state. In the *linear* regime, a conducting channel is created between source and drain electrodes and the transistor is said to be in its *ON* state. In this regime, the transistor behaves like a resistor that can be controlled by varying the gate voltage. In the *saturation* regime the source-drain current is almost independent of the source-drain voltage and depends only on the gate voltage.

In terms of energy bands of metals and semiconductors, the FET behavior could be explained as following:

At equilibrium (V_G = 0V), the insulator-semiconductor interface is depleted of charge carriers. As V_G is decreased (i.e. made more negative for *p*-type conductors), holes are attracted towards the organic-gate insulator interface. Once the concentration of holes at the insulator-semiconductor interface reaches the limit so that no further charges can be induced into the semiconductor then the *flat band condition* is reached and at this point the gate voltage V_G is equal to the *flat band voltage* V_{FB}. Further increase in the absolute value of V_G results in accumulation of holes at the insulator-semiconductor interface and and the FET can be modeled as equivalent to a capacitor with gate insulator acting as a dielectric. The density of holes in the accumulation layer can be described by

$$Q_{acc} = -C_i(V_G - V_{FB}) \quad . \qquad 4.24$$

Here C_i is the capacitance of the gate insulator per unit area

Output and transfer characteristics of OFETs

Figure 4.11 shows typical output (I_{SD} vs. V_{SD}) and trans-conductance (I_{SD} vs. V_G) characteristics for an OFET based on rubrene single crystal [122]. Unlike Si-MOSFETs which operate in the inversion mode, OFETs operate in accumulation and the voltage needed to turn on the OFET corresponds to the flatband voltage (V_{FB}) plus contributions due to surface traps, organic-gate dielectric interface states etc. This *ON* voltage is referred to as threshold voltage (V_{th}), which can be calculated from the transfer characteristic shown in the *figure 4.11 (b)* by estimating the intercept of the square root of the source-drain current on the gate voltage scale.

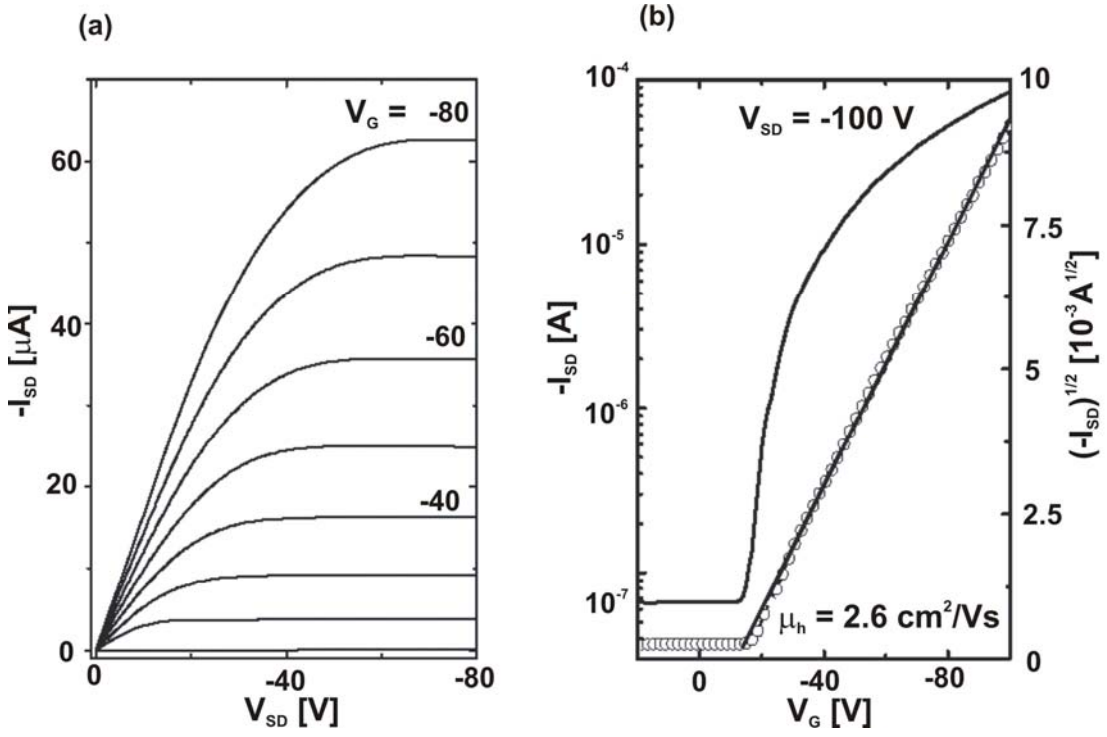

Figure 4.11 (a) *Output characteristic and* ***(b)*** *transfer characteristic for hole transport in a rubrene single crystal based OFET [122].*

In a simplistic approach, the threshold voltage can be related to the density of deep traps by the following equation

$$V_{th} = \frac{eN_{t,d}}{C_i} \quad . \qquad 4.25$$

In the linear region the source-drain current (I_{SD}) is described by,

$$I_{SD,Lin.} = \frac{W}{L}\mu C_i (V_G - V_{th}) V_{SD} \qquad 4.26$$

where W is the width of the channel, L is the length of the channel and C_i is the capacitance per unit area of the gate insulator.

The charge carrier mobility can be estimated from the *linear* regime of the OFET characteristics by taking the partial derivative of the *equation 4.26* with respect to V_G

$$\mu_{lin} = \frac{L}{WC_i V_{SD}} \frac{\partial(-I_{SD})}{\partial V_G} \quad . \qquad 4.27$$

The *saturation* regime is reached when the channel charges at the drain contact vanish and the drain current becomes almost independent of V_{SD}. This is also called *pinch-off* and is reached when $V_{SD} = V_G - V_{th} = V_{SD,\mathrm{Sat}}$. The source-drain current (I_{SD}) in the *saturation* regime is given by

$$-I_{SD,Sat.} = \frac{W}{2L}\mu C_i (V_G - V_{th})^2 \qquad 4.28$$

and the mobility in the *saturation* regime can be estimated by

$$\mu_{sat} = \frac{L}{2WC_i}\left(\frac{\partial\left(\sqrt{-I_{SD}}\right)}{\partial V_G}\right)^2 \quad . \qquad 4.29$$

Above formulation is based on standard MOSFET characteristics observed in conventional inorganic semiconductors and for all equations discussed above a *gradual channel approximation* has been assumed, i.e. the electric field gradient parallel to the surface is assumed to be much smaller than the electric field gradient perpendicular to the surface and the electric field gradient along the channel is constant. Application of MOSFET model should be considered as a very simplistic approach for the characterization of OFETs. However, this model enables us to get a first order estimation of various parameters in OFETs.

4.3 FET fabrication on DIP crystals

FET fabrication was performed under yellow light in order to minimize defects caused by photo-oxidation of the crystal surfaces. Chemical defects caused by photo-oxidation might severely hamper the device performance as oxidation states might contribute to surface traps [118]. Silver paste was used to paint source and drain electrodes on top of the DIP crystal prior to preparation of the gate insulator. The organic polymer parylene was deposited as gate insulator on the surface of the crystal (see *section 4.3.1*). The gate electrode was prepared by thermal evaporation of nearly a 20 nm thick gold layer on top of the gate insulator on the area in between source and drain electrodes.

Figure 4.12 shows the essential steps of FET fabrication. A typical OFET based on a DIP single crystal with a channel length of ~ 250 µm, channel width of ~ 4000 µm and insulator thickness of ~ 4 µm is shown in the *figure 4.12 (d)*. Temperature dependent FET measurements on these samples were performed under high vacuum (~ 10^{-7} Torr) using a Keithley 6517 electrometer (1 fA – 20 mA input current and up to ± 1000 V output) for applying V_{SD} and measuring I_{SD} and a Keithley 236 Source-Measurement-Unit (up to ± 110 V output) to apply V_G.

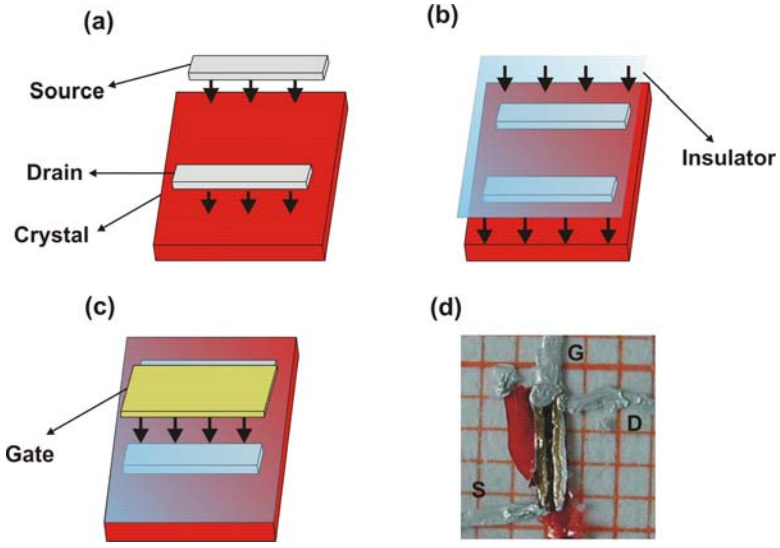

Figure 4.12 (a) *Preparation of source drain electrodes by painting silver paste.* ***(b)*** *Deposition of the polymeric gate insulator (parylene).* ***(c)*** *Preparation of the gate electrode by thermal evaporation of gold.* ***(d)*** *Optical image of a typical DIP FET: W = 4000 µm, L = 250 µm.*

4.3.1 Preparation of the parylene gate insulator

Sputtering of the conventional inorganic gate insulators, e.g. Al_2O_3, onto the surface of organic crystals, are not suitable for OFETs as they cause severe damage to the active transport layer of OMCs during the sputtering process resulting in surface traps, which might completely suppress the field-effect [121]. Also, its very difficult to form pinhole free thin layers of Al_2O_3 for gate dielectric applications. PDMS-based stamp techniques make it possible to realize OFETs with high dielectric constant gate insulators [121,123] though it was found that the use of high dielectric gate insulators cause an irreversible damage to OFETs because of the strong leakage current inducing damage of the transport layer [124,125] and possible bending of the crystals during the measurements.

A suitable gate insulator for OFETs based on single crystals remained a big hurdle until polymer films of parylene were probed as a novel material for the fabrication of gate insulator on top of single crystals [126]. Parylene has various advantages over inorganic gate insulators, such as its fabrication is inexpensive, it forms pinhole free layers down to 300 nm thicknesses, it does not cause severe damages to the surface of the organic crystals and therefore minimized interface traps etc. Parylene has a dielectric constant ε_i of ~ 2.65 [127] and it serves as a good insulator for OFET based on organic crystals. *Figure 4.13* shows the schematic of the parylene deposition set-up.

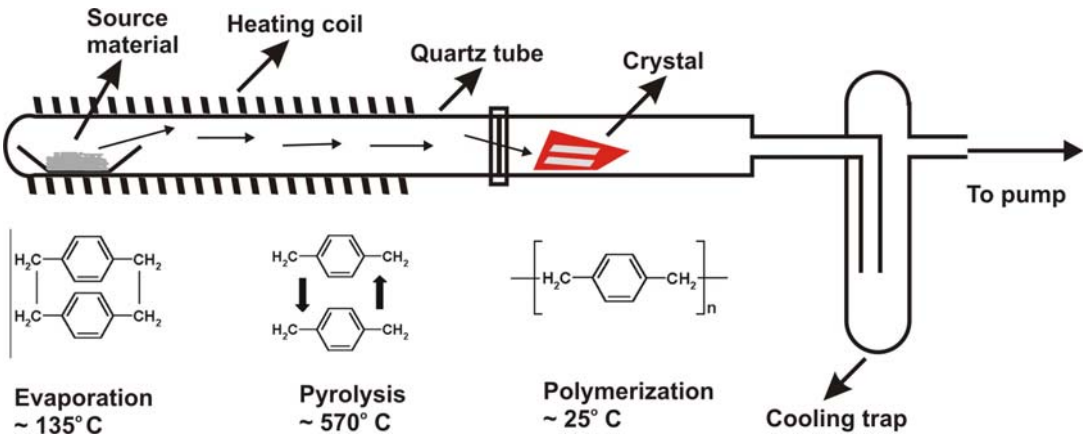

Figure 4.13 *Schematic diagram of the parylene deposition set-up.*

The set-up is consisting of a quartz tube, with three different temperature zones, namely, the evaporation zone, the pyrolysis zone and the polymerization zone (or deposition zone). An organic crystal with prefabricated source drain electrodes is placed in the polymerization zone that is maintained at room temperature and at low pressure (~ 10^{-3} Torr). Commercially available dimer para-xylylene is vaporized in the evaporization zone at a temperature of ~ 135 °C. The vapor passes the pyrolysis zone at ~ 570 °C where the dimer is monomerized and finally polymerizes upon deposition on top of the surface of the organic crystals in the polymerization zone maintained at room temperature.

Parylene films show sufficiently good insulating behavior and form pinhole free films of ~ 40 nm roughness estimated by the AFM measurements. Also, the dielectric breakdown occurs only for fields greater than 3 MV/cm which provides the gate voltage limit as high as 1000 V for a 3μm thick parylene insulator.

4.3.2 Thickness measurement of parylene film

The thickness of the parylene gate insulator was measured by the Fabry-Perot oscillations observed in the infra-red absorption spectra. *Figure 4.14* shows the IR absorption spectra in normal incidence mode for a parylene film of 7μm thickness.

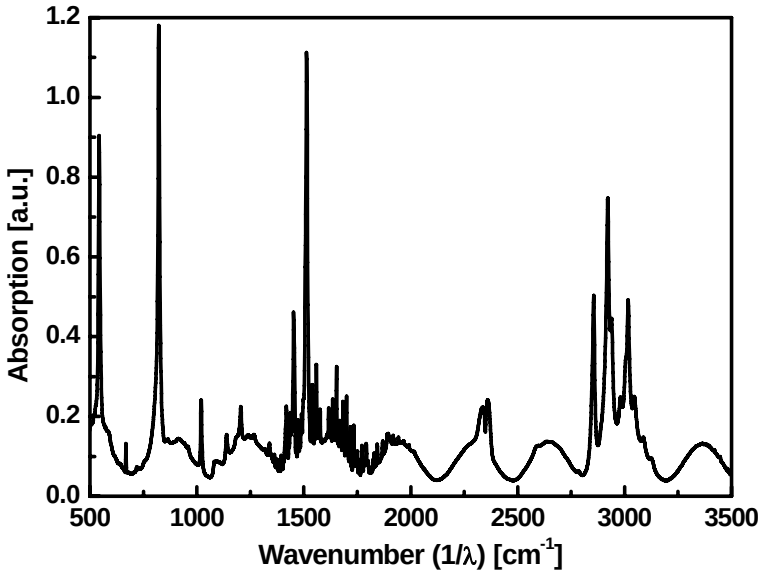

Figure 4.14 *IR absorption spectra for a ~ 7μm thick parylene film.*

As it can be seen, spikes in the absorption spectra correspond to the excitations of individual vibration modes of the PPX molecule. We observed superimposed oscillations due to the interference caused by the multiple reflected beams from the surfaces of the parylene film.

Schematic representation of formation of Fabry-Perot oscillations due to the interference is shown in the *figure 4.15*. An incoming beam with intensity I_0 undergoes direct transmission and multiple reflections from the surface of the film. When the optical path difference between transmitted and reflected beam is an integer multiple of the incident wavelength λ, they interfere constructively resulting in maxima in the transmitted intensity I. Condition for the interference maxima can be formulated as

$$2n_i d \sin\theta = m\lambda \qquad 4.30$$

where $n_i = (\varepsilon_i)^{1/2} \cong 1.4$ is the refractive index of the parylene film and m is the order of the maxima. Now taking two consecutive maxima of m^{th} and $(m+1)^{th}$ order, under the normal incidence $\theta = 90°$, we can rewrite *equation 4.30* as

$$1 = 2d\left[\frac{n_i(\lambda_1)}{\lambda_1} - \frac{n_i(\lambda_2)}{\lambda_2}\right] \quad . \qquad 4.31$$

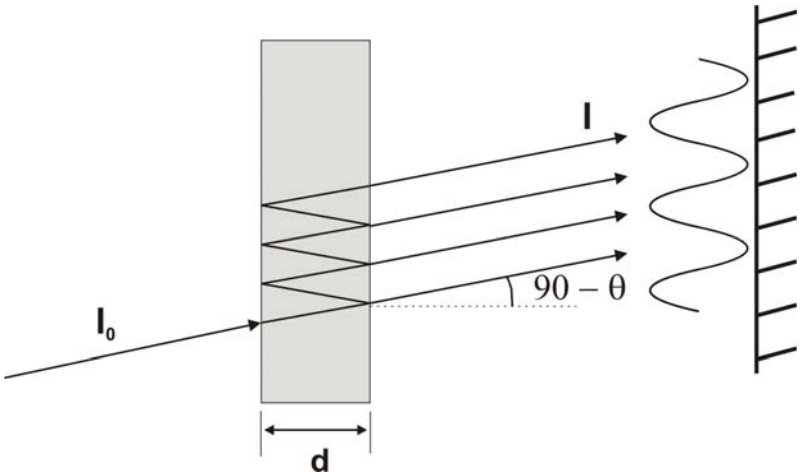

Figure 4.15 *Schematic representation of Fabry-Perot oscillations observed in IR transmission spectroscopy.*

In the non-dispersive region at low wavenumbers, $n(\lambda_1) \approx n(\lambda_2)$ and we can estimate the thickness by

$$d = \frac{1}{2n_i}\left[\frac{1}{\lambda_1} - \frac{1}{\lambda_2}\right]^{-1} \quad . \qquad 4.32$$

The thickness of the used parylene layers varies between 3µm to 10µm, depending on the different growth runs, amount of the starting material, and the deposition time.

4.4 Differential scanning calorimetery (DSC)

In the present work we have used a Perkin-Elmer DSC2 power-compensation differential scanning calorimeter for estimating the thermodynamic parameters of the phase transition in DIP crystals. *Figure 4.16* shows the schematic of our DSC set-up.

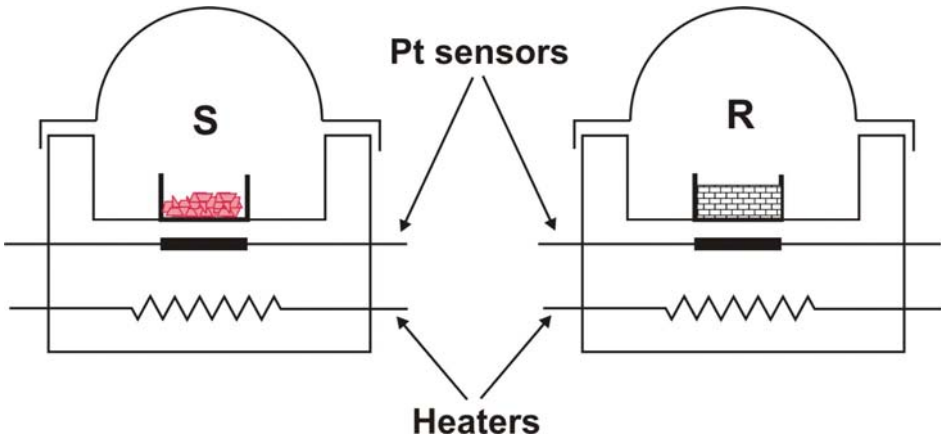

Figure 4.16 *Schematic of differential scanning calorimetry setup.*

Differential Scanning Calorimetry (DSC) is a thermoanalytical technique, which is widely used to study phase transitions, oxidation, crystallization etc. In DSC we measure the heat energy needed to establish a zero temperature difference between the sample and a *Platinum-Iridium* reference target, both subjected to identical heating or cooling.

Figure 4.17 shows a characteristic DSC spectrum illustrating various thermally induced processes which could occur in a polymer sample during the temperature ramping. An

exothermic process releases heat and therefore would result in a positive peak whereas endothermic processes would absorb heat resulting in a negative peak in the DSC spectra. For example, a glass transition may occur upon heating an amorphous solid which appears as a step in the DSC signal because of the change in the heat capacity of the sample. Upon further heating the sample might form a crystalline phase, which is an exothermic process and results in a positive peak in the DSC signal. Further increase in the temperature causes the material to melt and results in an endothermic peak in the DSC signal. Other exothermic processes such as cross-linking in polymers and/or oxidation and decomposition of the material can also be studied by DSC curves.

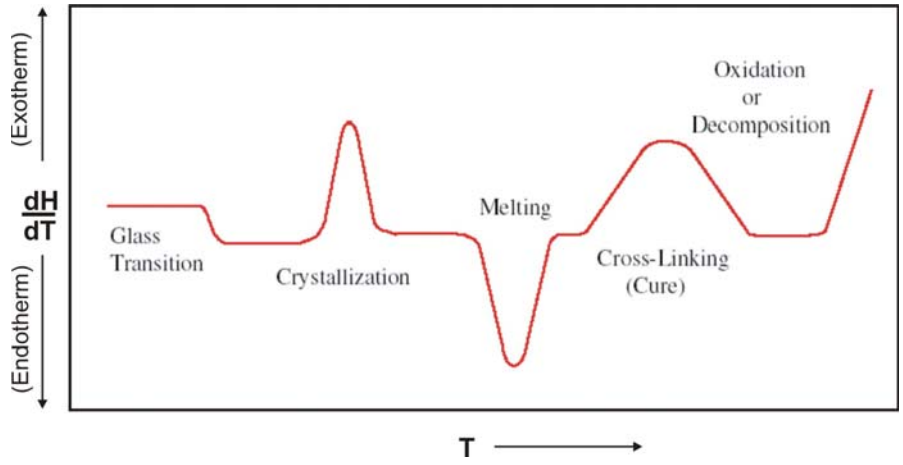

Figure 4.17 *Characteristic DSC spectra illustrating common features occurring during the measurements on polymer sample.*

If the material undergoes a solid to solid phase transition, the corresponding endothermic or exothermic peak could be detected in the DSC signal. The enthalpy of the phase transition can be estimated by

$$\Delta H = KA \tag{4.33}$$

where ΔH is the change of enthalpy, K is the calorimetric constant and A is the area under the measured DSC curve. Further, we know that change in free energy ΔG is given by

$$\Delta G = \Delta H - T\Delta S \tag{4.34}$$

For a first order phase transition $\Delta G = 0$ and therefore the change in entropy, ΔS, can be directly calculated from the DSC curve by normalizing the change of enthalpy to the respective transition temperature

5 Structural Phase Transition in DIP Crystals

Various organic semiconductors show a temperature dependent structural phase transition in single crystals, e.g. pentacene [128], tetracene [129] etc. Phase transitions affect the electronic transport due to the strong correlation between structural and electronic properties of a semiconductor. In this chapter we shall present a detailed study of the temperature dependent structural phase transition occurring in DIP single crystals.

5.1 X-ray diffraction measurements

Temperature dependent X-ray measurements were performed under vacuum ~ 10^{-3} Torr on crystals with free surfaces (uncapped) as well as on those capped with about 20 nm thick evaporated silver. The latter was performed in order to obtain an adequate comparison between the temperature dependent structural phase transition and the TOF mobilities for which back and front electrodes were prepared by nearly 20 nm thick silver layers. Crystals were attached to a Si (111) wafer by small droplets of silver paste at the edge of the crystals to minimize possible clamping effects by the substrate.

Temperature dependent X-ray diffraction measurements

Figure 5.1 shows the Bragg spectrum at room temperature. Bragg peaks up to the fourth order could be observed with rapidly decreasing intensity. The first order Bragg peak at room temperature corresponds to a lattice spacing of 14.4 Å ($q_z \approx 0.44$ Å^{-1}). Taking into consideration the molecular length of about 18.4 Å, this spacing matches to molecules standing almost upright with their long axis tilted by ~ 40° with respect to the surface normal.

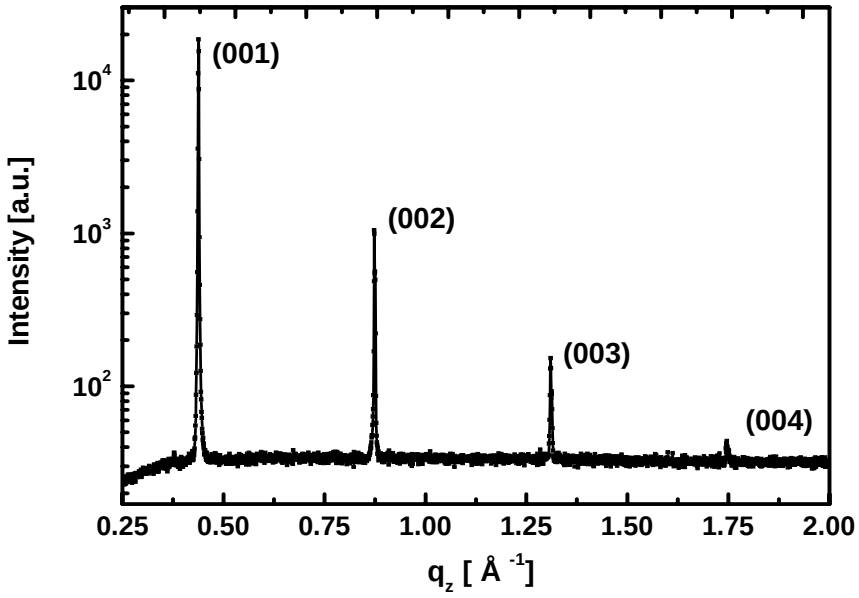

Figure 5.1 *Bragg reflections in DIP crystal along the c'-direction (00l) at 298 K.*

Above 370 K the (*00l*) structural Bragg peaks decrease in intensity and a new peak evolves at $q_z \approx 0.38$ Å^{-1} corresponding to a larger lattice spacing of 16.7 Å. This spacing was observed earlier in layers of DIP grown on weakly interacting substrates such as SiO_2, and is referred to as thin film phase [91] and resembles to almost upright standing DIP molecules.

Figure 5.2 shows the first order Bragg peaks corresponding to the two phases at different temperatures respectively in case of an uncapped crystal. This process of phase transition is reversible and the peak corresponding to the room temperature phase is retrieved upon cooling down the crystals. At temperatures above 400K the room temperature phase has been completely vanished and only the peak attributed to the new phase can be recognized in the X-ray diffraction pattern.

From now on we shall refer to the room temperature phase as *Low-T* phase (or *α-phase*) and the phase at temperatures above 400 K as *High-T* phase (or *β-phase*).

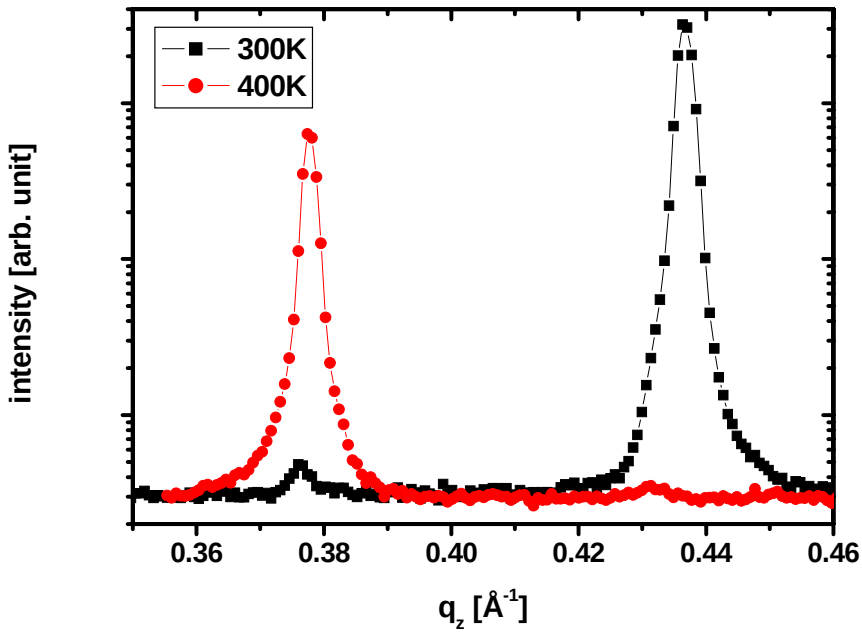

Figure 5.2 *First order Bragg peaks corresponding to the two structural phases measured on an uncapped DIP crystal.*

Figure 5.3 shows the orientation of the DIP molecules along the (*001*) direction, also referred to as *c'*-direction for both *Low-T* and *High-T* phase.

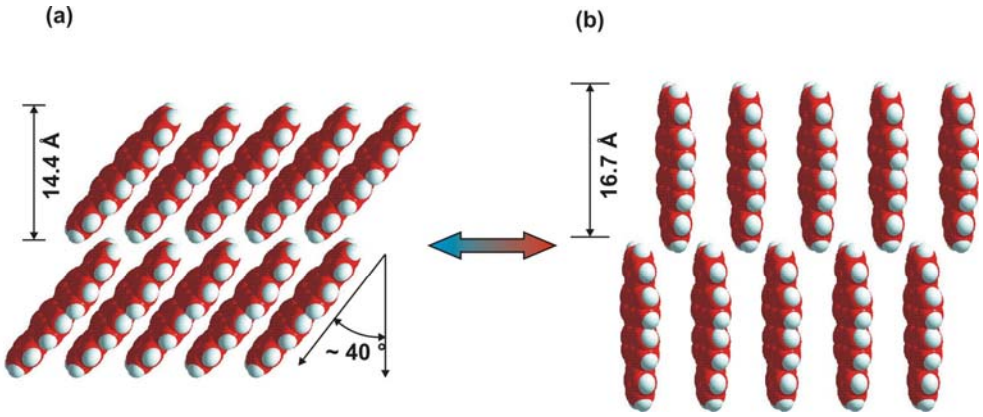

Figure 5.3 *Orientation of DIP molecules along the (001) direction* ***(a)*** *in Low-T phase and* ***(b)*** *in High-T phase.*

In order to get an insight in the underlying microscopic mechanisms of the phase transition we have performed temperature dependent X-ray diffraction measurements on high quality DIP crystals with free surfaces. *Figure 5.4* shows the first order Bragg peaks at various temperatures. The peak corresponding to the *Low-T* phase (*figure 5.4 (a)*)

decreases gradually in intensity and the peak corresponding to the *High-T* phase (*figure 5.4 (b)*) evolves at around 370 K. We shall refer to this temperature of 370 K as on-set of the structural phase transition (T_{ph}).

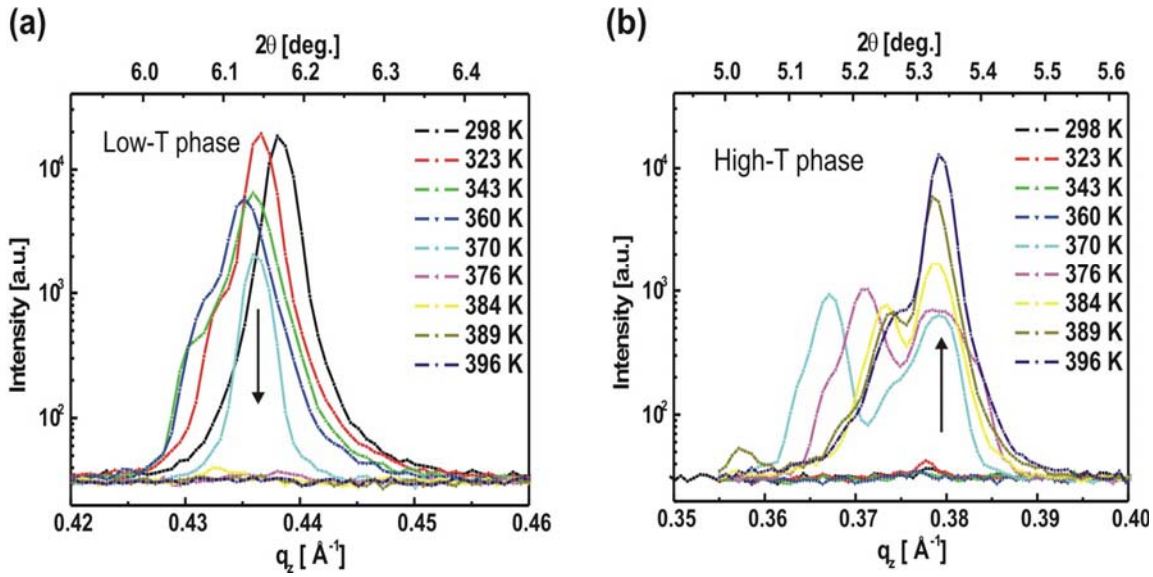

Figure 5.4 *First order Bragg peaks at different temperatures corresponding to* ***(a)*** *Low-T phase and* ***(b)*** *High-T phase.*

The *High-T* phase evolves in an irregular manner as a function of temperature, leading to a well defined peak at elevated temperatures when the phase transition is almost completed. In addition there is a metastable phase, which finally merges into the *High-T* phase.

Crystallite size as a function of temperature

Crystal structure as well as crystallite size strongly affect the electronic properties of a given compound. The crystallite size can be calculated from the width of the Bragg peaks using the Scherrer formula (*equation 4.9*), as mentioned in Chapter 4.

As can be seen in *Figure 5.4 (a)*, the first order Bragg peak corresponding to the *Low-T* phase is almost symmetric at RT (298 K). Upon heating a shoulder appears in the Bragg peak at $q_z \approx 0.43$ Å^{-1} at 323 K, probably due to the local rearrangement of molecules in the metastable phase. At 370 K the peak becomes symmetric again. At this temperature,

Low-T and *High-T* phase co-exist. The *Low-T* phase vanishes upon further heating of the crystal.

The *High-T* phase shows a more complex behavior and there clearly is a well-separated metastable phase, which merges into the stable *High-T* phase when the phase transition is completed. The lattice spacing corresponding to the intermediate phase depends strongly on the temperature and eventually merges into the lattice spacing of the *High-T* phase. This indicates crystalline fractions of intermediate metastable phase formed during the phase transition. Measurements were performed in an interval of ~ 2 hrs and the lattice spacing corresponding to the intermediate phase possibly depends on the measurement time as well.

Figure 5.5 shows the crystallite size corresponding to *Low-T*, *High-T* and intermediate phases as a function of temperature, estimated from the width of the respective first order Bragg peaks.

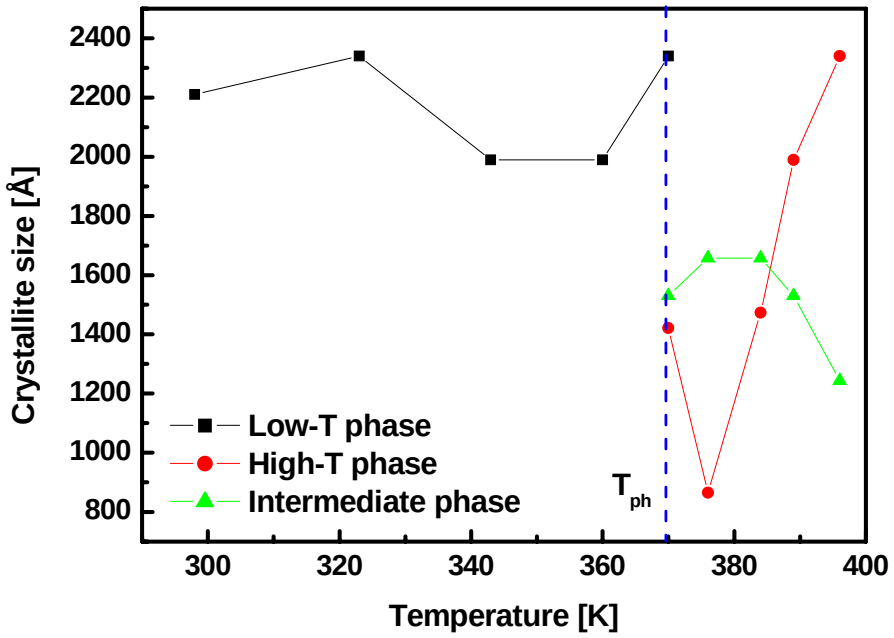

Figure 5.5 *Crystallite size as a function of temperature for Low-T, High-T and intermediate phases in DIP crystals along the c'-direction.* The *dashed blue line indicates the on-set of the phase transition at 370 K.*

The crystallite size corresponding to the *Low-T* phase remains almost constant between 2000 - 2400 Å up to 370 K, i.e. up to the on-set of the phase transition. Slight variations in the crystallite size could be attributed to thermal effects on the granular structure of the crystals, e.g. stress release by annealing. At 370 K we find coexistence of *Low-T*, *High-T* and an intermediate phase with a lower crystallite size of ~ 1500 Å for the *High-T* and intermediate phases whereas the crystallite size corresponding to the *Low-T* phase remains almost constant at around 2400 Å. Crystallites corresponding to the *Low-T* phase vanish upon further heating and the *High-T* phase starts to evolve rapidly. At the same time crystallites corresponding to the intermediate phase decrease in size. At around 400 K the intermediate phase converges into the *High-T* phase and eventually the crystallite size in the *High-T* phase is nearly the same as that in the *Low-T* phase at RT. This indicates that the phase transition proceeds by gradual rearrangement of individual crystallite fractions and the whole crystal transforms from *Low-T* phase to *High-T* phase upon heating without significant loss of structural coherence in the respective crystalline domains along the *c'*-direction.

Structural quality as a function of temperature

Phase transition causes structural defects within the crystals during the cooling down to room temperature after the growth cycle. In order to check the quality of the crystals we performed rocking curve measurements at the first order Bragg peak. *Figure 5.6 (a)* shows the rocking curve at room temperature. There are various sharp peaks in the curve indicated by black arrows which possibly resemble ordered crystalline fractions. However, these fractions themselves are tilted against each other which results in an effective broadening of the rocking curve. Average effective tilting of these crystallites is calculated from the full width at half maxima (FWHM) of a Gaussian fit to the experimental data. The FWHM is around 1.48°, which corresponds to an average tilting of crystallites of about 0.74° around the surface normal. Therefore, the rocking curve indicates a strong tilting of crystallites in the crystals. For highly ordered DIP thin films on SiO_2 this tilting was estimated to be of the order of 0.02°. Therefore while comparing

the electronic properties or DIP crystals with those of thin films one has to keep this in mind as the transport properties depend strongly on the structural order [28].

Rocking curves at individual temperatures were not possible to measure, due to the time constraints and also to minimize the effect of temporal degradation of the sample upon heating. *Figure 5.6 (b)* shows the comparison between rocking curves measured at the room temperature in the beginning and after cooling down the crystal. As can be seen, there is a strong intensity loss due to the shattering of crystals upon crossing the phase transition temperature of ~ 400 K while cooling down.

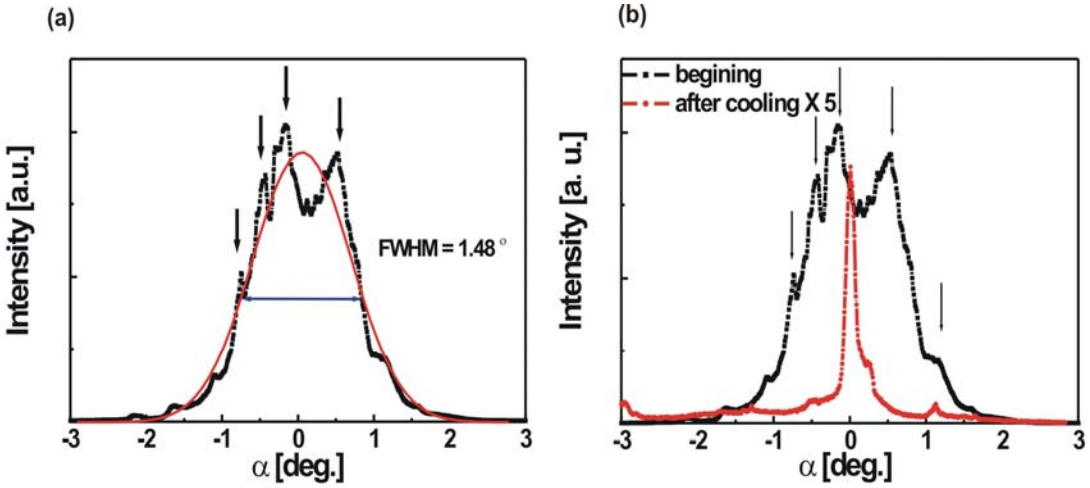

Figure 5.6 (a) *Rocking curve at the first order Bragg peak along the c'-direction in DIP crystal at room temperature. Black arrows indicate peaks corresponding to crystalline fractions and the red curve represents a Gaussian fit to the experimental data.* ***(b)*** *Comparison between rocking curves at room temperature measured in the beginning and after cooling down the crystal. For better illustration, intensity corresponding to the latter has been multiplied by a factor of five.*

The integrated Bragg intensity is influenced by the overall quality of the crystals: that is crystallite size as well as tilting of crystallites. *Figure 5.7* shows the integrated Bragg intensity for *Low-T*, *High-T* and intermediate phase as a function of temperature. Since the effective rocking width is much larger than the width of the Bragg peaks, we have only integrated the Bragg peaks without convoluting it with the rocking curve. The width

of the rocking curve is assumed to be much larger and therefore the relative change with the temperature much smaller than the Bragg peak over the entire temperature range. The integrated Bragg intensities are normalized to estimate the crystalline fractions of the respective phases. At room temperature, only the integrated intensity corresponding to the *Low-T* phase is observed whereas above 370 K, the intermediate phase and the *High-T* phase start to evolve. In agreement, the intensity corresponding to the *Low-T* phase decreases on the expense of the *High-T* and the intermediate phases.

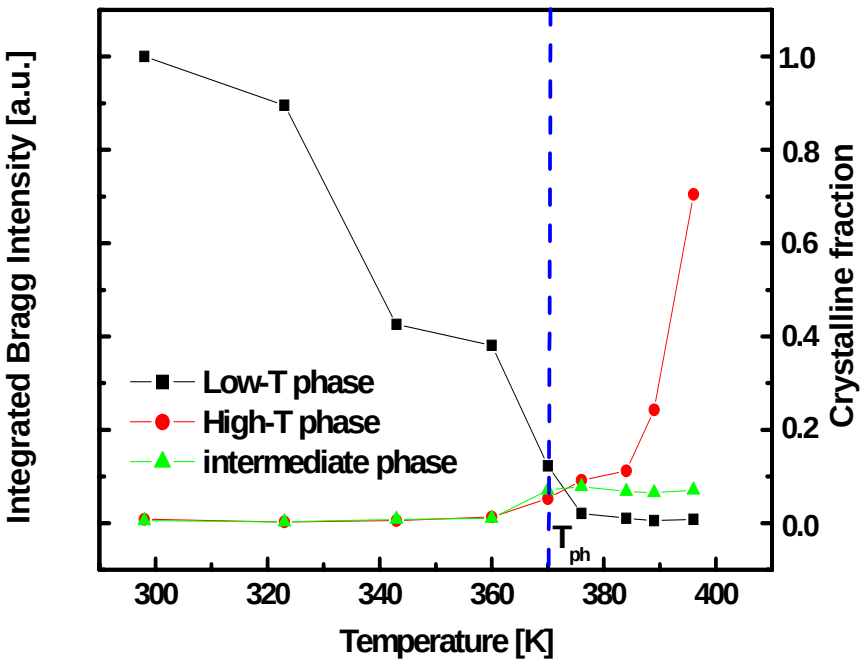

Figure 5.7 *Integrated Bragg intensity at the (001) position as a function of temperature.*

As it can be seen in *figure 5.7*, at 370 K the coexisting crystalline fractions of all three phase measure to only ~ 30% of the initial *Low-T* phase at room temperature. However, at 396 K the combined crystalline fractions amount to nearly 85% of the initial *Low-T* phase. Once the phase transition is almost completed only the *High-T* phase survives and the *Low-T* phase vanishes. We observe a small loss in crystallinity upon phase transition which could be attributed to formation of stress induced structural defects as well as the still incomplete structural phase transition.

5.2 Single Crystal Diffractometry

Out-of-plane X-ray diffraction measurements provide information on the lattice spacing and structural quality along the surface normal of the crystal. However, these measurements are insufficient to provide the complete crystal structure, and the molecular conformations. Single crystal diffractometry is necessary to obtain the crystal structure and to understand phase transition mechanisms on the molecular level. The corresponding measurements were performed at Alcatel-Lucent laboratory as a part of our research collaboration with Dr. T. Siegrist and his group. In this section we shall summarize the results of diffractometry measurements and will make an effort to understand the individual steps defining the structural phase transition in DIP single crystals.

5.2.1 Enantiotropic polymorphism in DIP

Low-T polymorph of DIP (α-phase)

The *Low-T* phase or *α-phase* is consisting of two conformationally different molecules per unit cell with a coordination number $Z = 2$. One DIP molecule is bent and the other one is a twisted isomorph. In the *α-phase*, DIP crystallizes into a triclinic structure with lattice constants of a = 11.58 Å, b = 12.96 Å, c = 14.88 Å, α = 98.14°, β = 98.10°, γ = 114.53°, space group $P\bar{1}$ and a unit cell volume of V = 1963.0 Å^3 at 298 K. *Figure 5.8 (a)* shows two different kinds of molecules within the unit cell: one twisted and the second one bent around it. The DIP molecules form herringbone packed layers within the *(ab)*-plane and within a herringbone-packed layer, the molecules form centrosymmetric quadruples of two twisted and two bent isomorphs, i.e. in total 4 molecules per unit cell. The molecules of a quadruple are slightly misaligned by around 0.7 Å.

High-T polymorph of DIP (β-phase)

The *High-T* or *β-phase* forms a monoclinic structure at temperatures above 403 K with lattice constants of a = 7.17 Å, b = 8.55 Å, c = 16.80 Å, β = 92.42°, space group $P2_1/a$

and a unit cell volume of V = 1028.9 Å^3 at 423 K with 2 molecules per unit cell. The unit cell corresponding to the *β-phase* of DIP is shown in *figure 5.8 (b)*. Unlike in the *α-phase*, the *β-phase* has only one type of planar molecule with a coordination number of Z = 4 in the unit cell. Lattice parameters, symmetry and unit cell volume corresponding to the triclinic *Low-T α-phase* at 298 K and the monoclinic *High-T β-phase* at 423 K are summarized in the *table 5.1*.

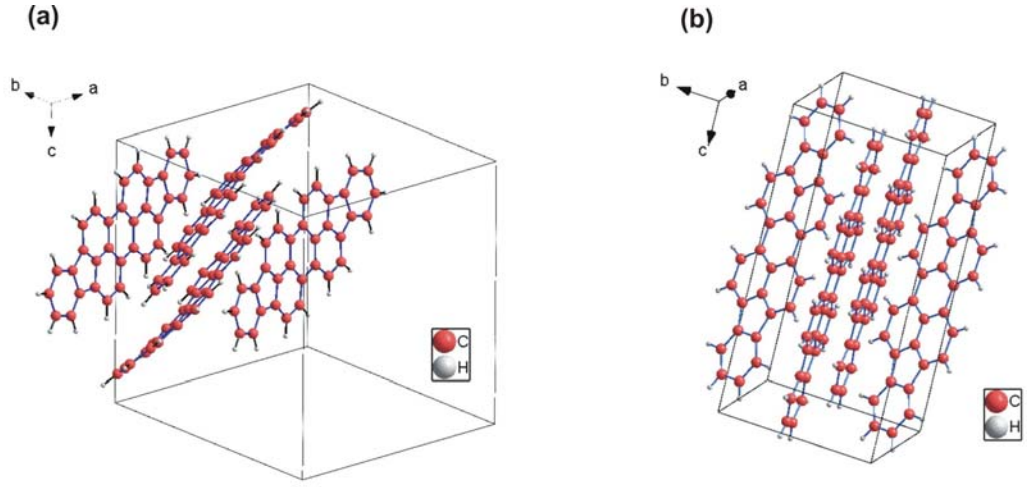

Figure 5.8 (a) *Unit cell corresponding to the triclinic α-phase of DIP crystals at 298 K.*

(b) *Unit cell corresponding to the monoclinic β-phase at 423 K.*

Table 5.1 *Lattice parameters for DIP crystals in the Low-T (298K) and High-T (423K) phases.*

	Low-T (α-phase) (at 298 K)	High-T (β-phase) (at 423K)
Structure	Triclinic	Monoclinic
Coord. No.	2	4
Space group	$P\bar{1}$	$P2_1/a$
a (Å)	11.5848 (6)	7.1709 (8)
b (Å)	12.9624 (7)	8.5496 (9)
c (Å)	14.8847 (7)	16.7981 (2)
α (°)	98.136 (4)	90
β (°)	98.089 (4)	92.416 (11)
γ (°)	114.531 (5)	90
V (Å^3)	1963.0 (2)	1028.9 (2)
# per unit cell	4	2

Figure 5.9 (a) and *(b)* show the herringbone layers corresponding to the *α- and β- phases* respectively. In ordered to illustrate the difference between the two phases, side views of the respective herringbone layers are shown in *figures 5.9 (c)* and *(d)*, indicating the alignment of the rows of molecules in both phases.

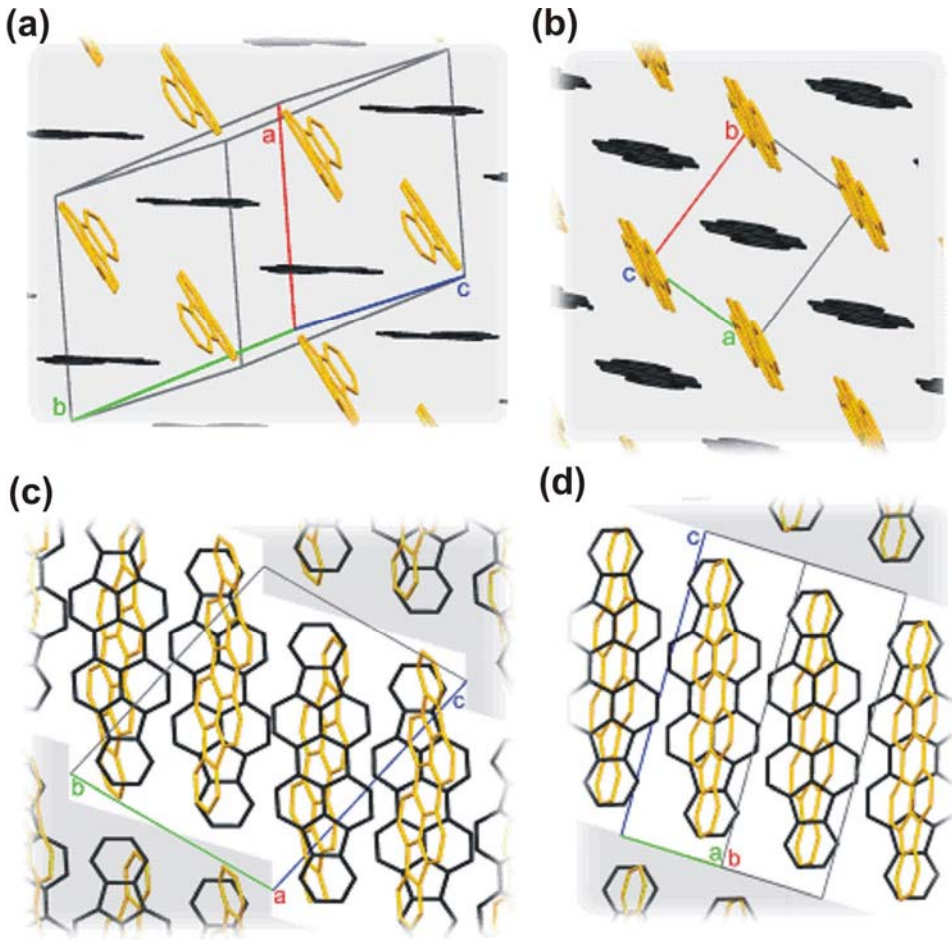

Figure 5.9 *Herringbone layers of the α- phase (at left) and the β-phase (at right). In the lower part, the herringbone layers are depicted from the side.*

As mentioned before, the twisting and the bending of two conformationally different DIP molecules in the *α-phase* is clearly visible. The larger tilt away from the *c'*-axis ((00l)-direction) in the α-phase is reflected in the unit cell. The individual DIP molecules pack in a two-dimensional herringbone-type layered structure, with pseudo-hexagonal order within the layers. The herringbone angle corresponding to the *β- phase* is 53.25º, similar to the value observed for pentacene [128]. Over the measured temperature range, the

herringbone angle of the *α-phase* increases monotonically with temperature from 55.02° at 110 K to 55.65° just below the phase transformation at 403 K. The molecular planes are almost perpendicular to the crystallographic *(ab)*-plane, at a tilt angles of 7.5º with respect to the *c'*-direction.

Conformationally different DIP molecules

Due to the lower, triclinic, space group symmetry in the *α-phase*, the molecules themselves are no longer planar and two differently distorted molecules, one bent and the other one twisted, are observed in the unit cell. In the bent DIP molecule, one terminal indeno group is bent away from the plane of the perylene moiety with respect to the other terminal indeno group by nearly 14° whereas in case of the twisted DIP molecule, one of the terminal indeno group is twisted around the molecular axis by nearly 4.6º. *Figure 5.10* shows a graphic representation of DIP molecules at various temperatures. Ellipsoids are estimated from the Debye-Waller factor and represent the volume in which the carbon atoms can be found with a likelihood of 50 %.

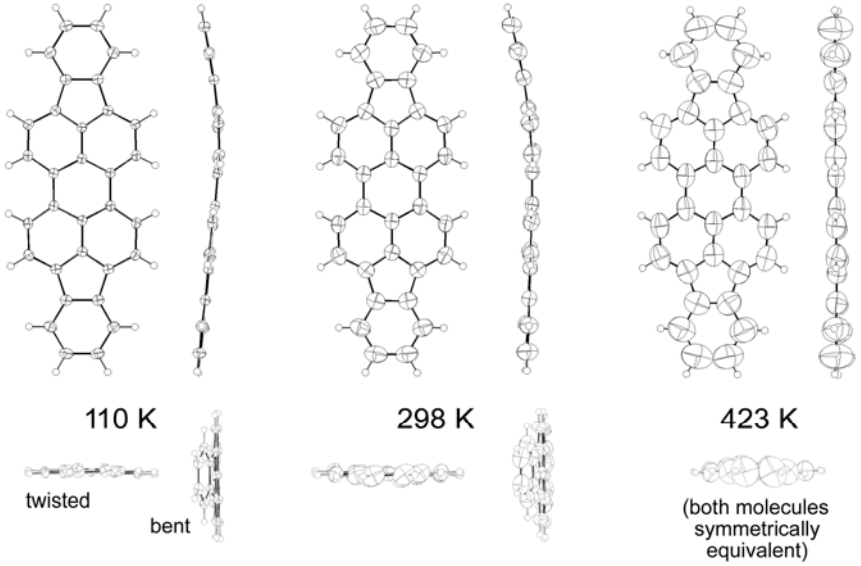

Figure 5.10 *Conformational comparison of the two DIP molecules at 110K, 298K and at 423K. The ellipsoids represent the volume in which the atom is found with a likelihood of 50%.*

At 110 K we have both bend and twisted isomers of DIP with lower thermal motion of carbon atoms, as indicated by smaller ellipsoids. At 298 K, we still have bent and twisted molecules but the bending is reduced and the molecules have a larger thermal motion. At 423 K, i.e. above the phase transition temperature, bending and twisting of the molecules are vanished and we have only one kind of planar DIP molecule in the unit cell with large atomic thermal motion yet small enough to mask the bending of the molecules, as it is shown in the right part of *figure 5.10*.

5.2.2 Phase transition from α- to β- phase

The phase transformation in DIP from the room temperature, triclinic, *α-phase* to the high-temperature, monoclinic, *β-phase* occurs at approximately 403K as estimated from single crystal diffractometry measurements. As mentioned earlier, the *α-phase* has two different kinds of molecules in the unit cell whereas the *β-phase* has a similar type of planar molecules in the unit cell. The transformation involves the halving of the *α-phase* unit cell along with the molecular rearrangements, mainly due to translations. Halving of the unit cell results in two molecules per unit cell in the *β-phase*. The monocrystalline nature in the *β-phase* obtained from transformation of a single crystal from the *α-phase* along with the loss in crystallinity in intermediate temperatures (see *figure5.7*) suggests an epitactic growth mechanism, i.e. phase transition proceeds through nucleation and subsequent growth processes [130]. Structural defects such as grain boundaries and dislocation lines act as possible nucleation sites.

The entire transformation can be subdivided into three hierarchic sub-transformations, which proceed simultaneously through the transformation. The first sub-transformation takes place on the level of the unit cell, and levels the corrugation of the herringbone planes through movement of the molecules along their long molecular axis. The second transformation involves the same direction of movement, but shears a whole herringbone plane. The third transformation on the level of many herringbone planes is a shearing re-alignment of these planes with respect to each other. These sub-transformations establish the structural analogy between the two phases, which is notably a prerequisite for epitactic growth [130].

The transformation involves strong shearing of around 40% of the crystal structure which frequently results in fracturing of the crystal. *Figure 5.11* shows the image of a DIP crystals immersed in a drop of paraffin oil and being heated above the phase transition temperature. Black arrows and lines are drawn along the crystallographically aligned edges before the heating as well as after the fracturing above the phase transition. Crystal fracturing is mainly stress generated due to the shearing of unit cell. It is also noticed that these cracks propagate in the *(ab)*-plane of the crystals. Crystal fracturing causes complications in temperature dependent measurements.

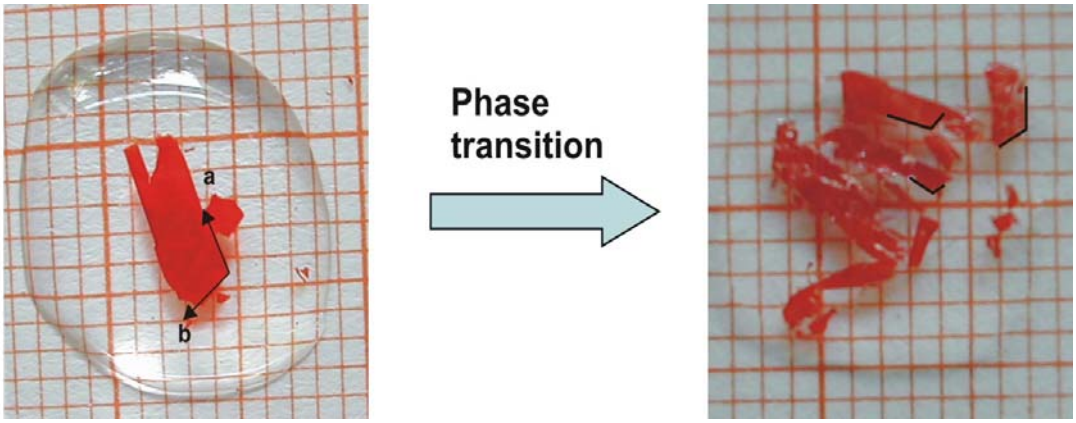

Figure 5.11 *Cracking of the crystals upon phase transition. Black arrows in the left picture represent the crystallographic a- and b- direction. Edges corresponding to the a- and b- directions are represented by black lines in the right picture.*

Heating or cooling rates should be very slow in order to successfully perform temperature dependent measurements without causing severe structural damage to the crystals. Also, during the growth by sublimation, crystals grow above the phase transition temperature and they have to cross the phase transition upon cooling down to room temperature. Most of the crystals shatter in this process and surviving crystals have severe structural defects due to the cracks within the crystals. Therefore, very seldom one can find a crystal good enough for temperature dependent measurements.

Lattice parameters as a function of temperature

Lattice parameters in the DIP crystals change with increasing temperature. This has been seen in the shift of the Bragg peak positions in temperature dependent X-ray diffraction measurements along the *c'*-direction. *Figure 5.12 (a)* shows the change along the three principal crystallographic axes *a*, *b* and *c* obtained by single crystal diffractometry. As one can see, up to 400 K all three parameters increase slightly with increasing temperature. Average increase in all three lattice parameters is ~ 2 % upon heating the sample from 100 K to 400 K. Thermal expansion coefficients of ~ 5.87 (± 0.35)×10^{-5} K^{-1} along the *a*-direction, ~ 3.85 (±0.28) ×10^{-5} K^{-1} along the *b*-direction and ~ 4.69 (± 0.30)×10^{-5} K^{-1} along the *c*-direction were estimated in the *α-phase*.

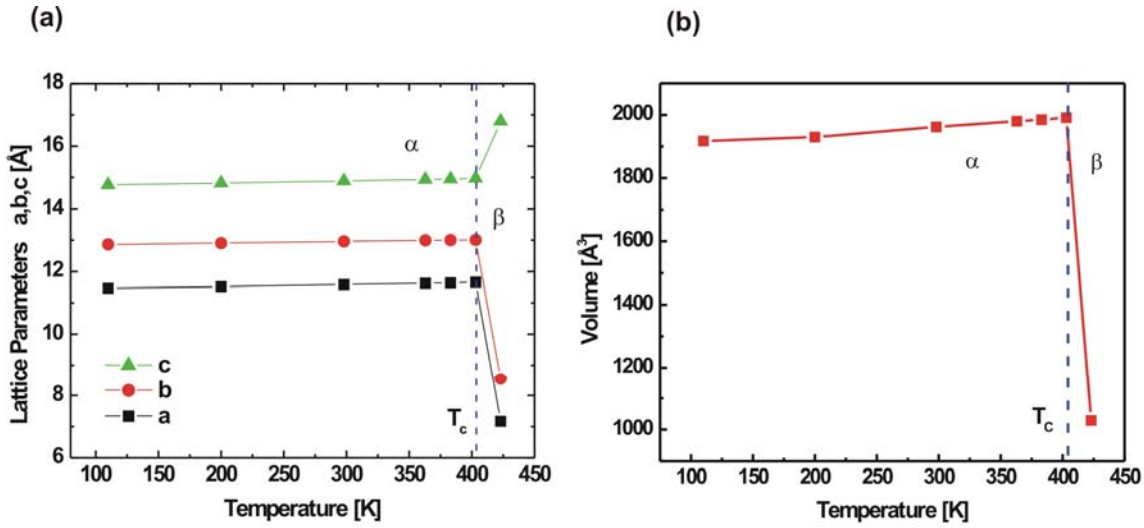

Figure 5.12 (a) *Lattice parameters as a function of temperature.* ***(b)*** *Unit cell volume as a function of temperature. The blue dashed line indicates the phase transition temperature. Sharp decrease in the unit cell volume above the phase transition temperature is due to the halving of the unit cell.*

Thermal expansion coefficients along all crystallographic directions are positive and are almost one order of magnitude lower than those reported on polyacenes e.g. naphthalene [131], anthracene [132], tetracene [133], and pentacene [134]. Lower thermal expansion coefficients in the *α-phase* of DIP crystals are possibly due to the fact that a fraction of

thermal energy is used by the gradual re-orientation of bent and twisted DIP molecules which eventually lead to a planar molecule in the *β-phase*. However, these linear expansion coefficients are comparable to the in-plane thermal expansion coefficient of ~ 7.58×10^{-5} K^{-1} reported for DIP thin films on SiO_2 substrates by A. Dürr [135].

Figure 5.12 (b) shows the corresponding change in the unit cell volume which increases by about 4.5% upon increasing the temperature from 110 K to 400 K. A thermal expansion coefficient of ~ 1.36 (± 0.11)$\times10^{-4}$ K^{-1} is estimated from the linear fit to the volume data.

Above the phase transition temperature the lattice parameters show a clear discontinuity, which is an indication of the first order phase transition. The spacing along the *a*-axis is contracted by about ~ 37 %, along the *b*-axis is contracted by 34 % whereas along the *c*-axis is expanded by ~13.5% which suggests that the DIP has a positive *Poisson's ratio*. The sharp decrease in the unit cell volume is caused by the halving of the unit cell upon the phase transition. These changes in the lattice parameters and the crystal structure from triclinic to monoclinic cause nearly 2.6% increase in the volume and nearly 40% shearing of the crystal structure, the latter of which is mainly attributed for the cracking of crystals, as discussed in the previous section.

Temperature dependent translations and librations in DIP crystals

Figures 5.13 and 5.14 show temperature variations of translations (T_i) and librations (L_i) respectively. Since the unit cell of the room temperature α-phase of DIP contains two crystallographically independent molecules, librational and translational values are given for both of them, together with the values above the phase transition. T_1 is around 1.4 T_2 and 1.9 T_3. Across the phase transition, the average T_1 increases by a factor of 1.4, T_2 also increases slightly by a factor of 1.1, whereas T_3 decreases by a factor of 1.2, thus increasing the anisotropy of the thermal motion of the molecule. The resulting T_1:T_2:T_3 ratio above the phase transition is 3.5:1.9:1 and therefore is comparable to that of tetracene [133]. Similarly, the libration L_1 around the long molecular axis is on average 3.8 times larger than the libration L_3.

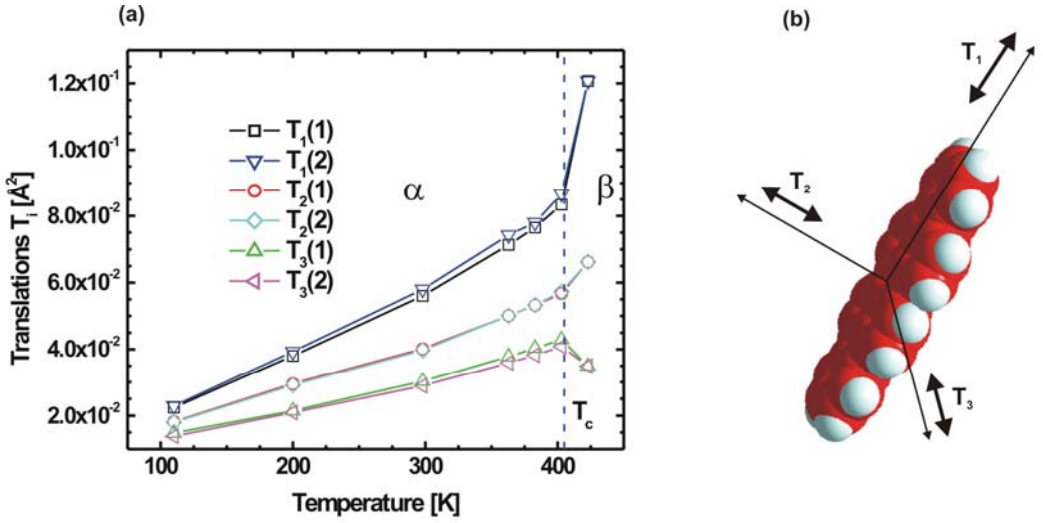

Figure 5.13 (a) *Translations of DIP molecules as a function of temperature.* ***(b)*** *Schematic representation of respective translational axes.*

Similar to the lattice parameters, translations and librations also show the discontinuity at the phase transition. Different libration and translation modes converge to a same value upon transition to the *β-phase* as there is only one type of planar molecule left in the monoclinic *β-phase*.

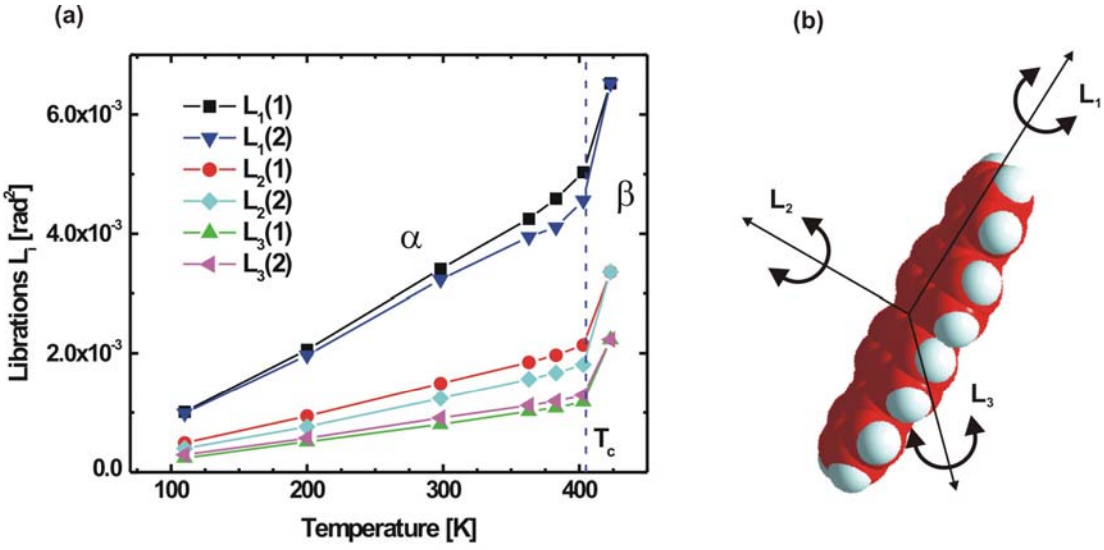

Figure 5.14 (a) *Librations of DIP molecules as a function of temperature.* ***(b)*** *Schematic representation of respective libration axes.*

The temperature dependence of librations and translations plays an important role in the electronic transport in these crystals as they can strongly influence the charge carrier scattering in case of band-like transport or they can enhance the hopping probability by providing additional activation energy. We shall recall these measurements in Chapter 6 to explain the temperature dependent electronic transport in DIP crystals.

5.3 Differential Scanning Calorimetry (DSC) measurements

In order to analyse the thermodynamics of the phase transition, DSC measurements were performed. *Figure 5.15* shows the DSC spectra measured on DIP crystal flakes (black curve) and DIP powder (red curve). To correct for temperature dependent contributions by the sample stage, the background of the spectra was subtracted by a third order polynomial function. We observe series of sharp transformation "spikes" at various temperatures which originate from the coexistence of many small crystallites in both DIP flakes and powder and these crystallites experience different thermal coupling to the sample holder causing a non-homogeneous temperature distribution and hence a distribution of transition peaks in the DSC spectra. Furthermore, due to the presence of metastable phases in the individual grains, the structural transition might be kinetically hindered.

As proposed in the literature [130], the necessity of nucleation frequently leads to large hysteresis of solid-solid transformations, especially at high crystalline perfection. This is assumed to be the cause of the different transition temperatures measured in small-grained DSC samples and in those used for diffraction experiments, and also accounts for the "spikes" visible in the DSC data. These are assumed to represent the (nucleation-dependent) transformation temperatures of individual grains. Peaks in the heating cycle of DSC measurements occur at slightly higher temperature than the phase transition temperature measured by single crystal diffractometry because of the experimental parameters, such as sample quality, history, and heating rate etc.

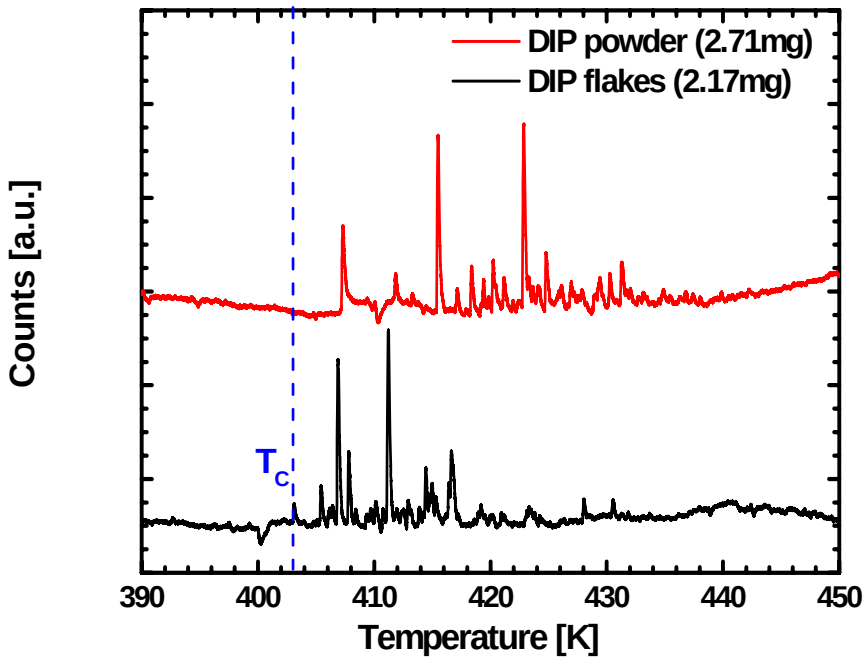

Figure 5.15 *DSC spectra for DIP crystals and powder. The dashed blue line indicates the phase transition temperature T_c at 403 K.*

Latent heat was measured by integrating over all peaks and scaled to an indium standard. Entropies were calculated with respect to the lowest observable phase transition peak of 403 K which is in good accordance with the single crystal diffractometry data. Assuming a first order phase transition, i.e. $\Delta G = 0$, the enthalpy of the phase transition ΔH of 1.0 ± 0.2 kJ/mol converts to an entropy of ΔS of 2.4 ± 0.5 J/(mol K) at 403 K.

From a theoretical approach, just considering the higher symmetry of the *β-phase*, phase transition will result in an entropy change of one bit per unit cell, i.e. ½kln(2) per molecule or 2.88 J/(mol K) as we have only one kind of planar molecule per unit cell in the *β-phase* compared to two conformationlly different molecule per unit cell in the *α-phase*. At 403K, this converts to a latent heat of $\Delta H = T\Delta S = 1.17$ kJ/mol. Interestingly, the theoretical values for entropy change due to symmetry is in good agreement with the entropy change measured from DSC spectra. However, these are preliminary estimation of the thermodynamic quantities and in order to give exact numbers one has to perform

detailed investigations and consider additional contributions from variation in the vibrational energy of the molecules, lattice energy etc., as a result of the phase transition.

5.4 Effect of silver encapsulation on phase transition

The occurring phase transition requires a rearrangement of molecules in the crystal lattice, which could be affected by the encapsulation of the crystal surfaces. Since TOF measurements were performed on crystals with evaporated silver as top and bottom electrodes, X-ray measurements on these crystals are necessary to provide an adequate correlation between structural and electronic properties. In case of encapsulated DIP crystals, the phase transition temperature is shifted towards higher values and the crystallite size corresponding to the *High-T* phase is relatively lower than that of the *Low-T* phase. *Figure 5.16* shows the first order Bragg peaks corresponding to the *High-T* and *Low-T* phases for a silver capped DIP crystal.

As it can be seen in the figure, the phase transition is not fully completed even at 405 K and a small Bragg reflex corresponding to the *Low-T* phase at 405 K can still be detected in contrast to the uncapped crystals. In addition, the peak corresponding to *High-T* phase shows a split, indicating the presence of a metastable or stressed phase. In contrast to uncapped crystals, crystallites in the *High-T* phase are smaller by almost a factor of two compared to the crystallite size in the *Low-T* phase at room temperature which indicates the structural hindrance presumably as a consequence of clamping by the encapsulation.

The exact origin of the deviation in phase transition behavior for capped DIP crystals is not fully understood yet but we will discuss this phenomenon in the framework of two different scenarios as following.

1. The top few monolayers of the crystal surfaces are pinned due to the strong interation between DIP molecules and the metal film and therefore resist any molecular rearrangement. This would hinder molecular rearrangement needed for the phase transition and would cause an additional stress in the material. This stress could be released by the formation of grain boundaries and hence resulting in smaller crystallite sizes compared to that in the *Low-T* phase, as it was experimentally evident. Also, the

phase transition temperature is shifted to higher values because of an increase in the thermal energy needed to overcome the steric hindrance caused by the pinning of top molecular layers.

2. An alternative reason could be the penetration of metal into the organic crystals. As it has been reported in the literature, metal can penetrate up to few monolayers into the organic films [136]. Localized silver particles in the organic layer might hamper the free movement of DIP molecules and hence hindering the phase transition.

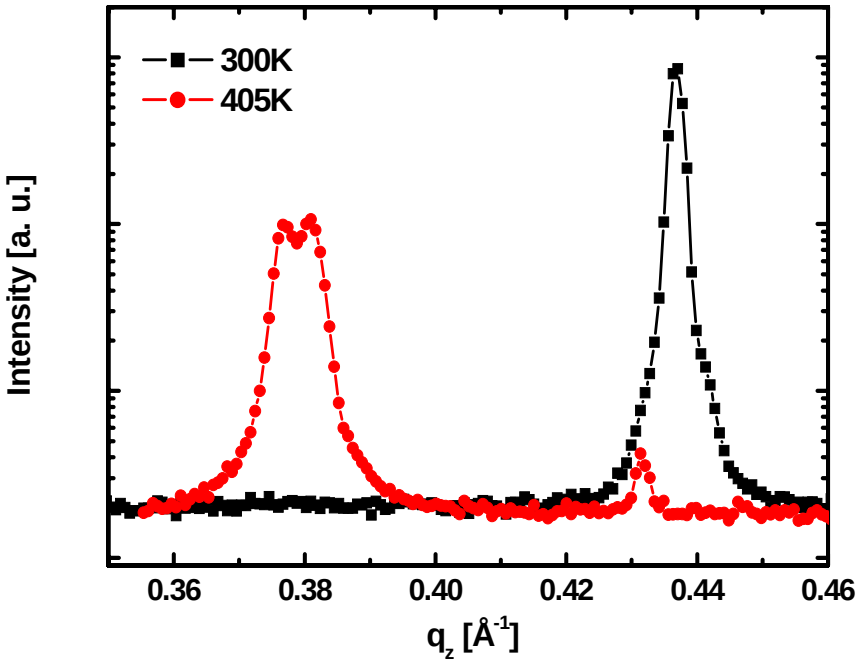

Figure 5.16 *Bragg peaks along the (00l) direction corresponding to the High-T and Low-T phases measured for a DIP crystal with evaporated silver contacts on both surfaces.*

6 Electronic Transport in DIP Crystals

In this chapter we shall study the electronic transport in bulk and on the surface of DIP single crystals by injection-free technique (TOF) and also by injection dependent techniques (SCLC and FET). We will study the effect of trap states, present in the bulk and on the surface of these crystals, on the electronic transport and perform a comparative study of the transport of photo-generated and injected charge carriers.

6.1 TOF measurements

TOF measurements were performed on sublimation grown DIP crystals of different thicknesses, as explained in Chapter 4. Comparable structural qualities of these crystals were ensured by X-ray diffraction measurements performed on crystals from the same growth run. Crystal thicknesses were in the range of 20 μm to 50 μm. An N_2 pulse laser in single shot mode at 337 nm wavelength and 0.76 ns pulse width was used for photo-generation of charge carriers. Measurements were performed on crystals grown under H_2 or forming gas flow and both exhibited similar transport properties.

Electron and hole transport in DIP crystals

Temperature dependent TOF studies were performed on different crystals revealing both hole and electron transits as shown in *Figure 6.1 (a) and (b)*. At room temperature (RT) the highest hole mobility was estimated to be ~0.003 cm^2/Vs whereas the highest electron mobility amounts to ~0.02 cm^2/Vs. Observation of the electron transient is remarkable as it has been shown that compared to zone refinement, organic compounds purified by sublimation only leave beyond a much higher density of oxidation by-products and other contaminants acting as charge carrier traps, especially for electrons [137]. DIP is a rare

organic compound that can be purified by sublimation technique only yet its crystals showed both electron and hole mobility in the bulk.

Comparing the room temperature TOF hole mobility values with those of FET measurements performed by M. Münch [28], we observed that the room temperature hole mobility is lower by about an order of magnitude in *c'*-direction than in the (*ab*)-plane, presumably due to the smaller π-orbital overlap.

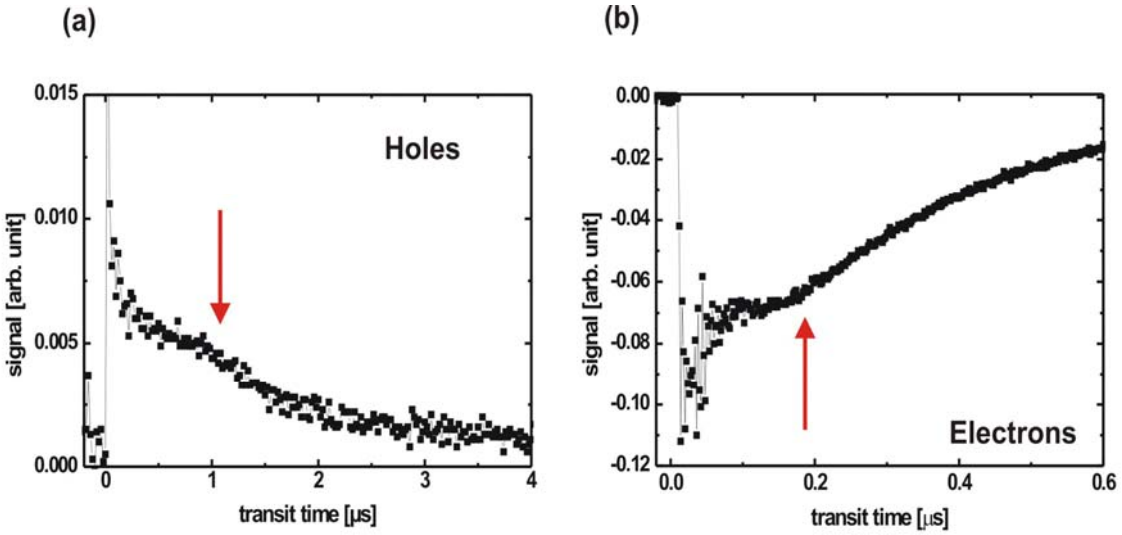

Figure 6.1 (a) *TOF hole signal along the c'-direction in a ~ 50μm thick DIP crystal at 413 K and* ***(b)*** *TOF signal for electron in the same crystal at 413 K. Red arrows indicate the respective transit times.*

As discussed in Chapter 4, DIP crystals undergo a structural phase transition, starting at 370 K. Therefore, in order to investigate the correlation between structural and electronic properties we performed temperature dependent TOF measurements on these crystals.

Temperature dependent TOF mobility

Figure 6.2 (a) and (b) show the temperature dependence of hole and electron mobilities respectively. Both electron and hole mobilities initially increase with increasing temperature followed by a drop around the on-set temperature T_{ph} (370K) of the phase transition estimated from the X-ray data, as indicated by the red arrows in *figure 6.2 (a) and (b)*. In case of holes, the drop occurs at around 380 K whereas for electrons the

mobility drops at around 365 K. Upon further increase in the temperature, both electron and hole mobilities increase up to the phase transition temperature ~400 K. The hole mobility remains almost constant upon heating above the phase transition whereas the electron mobility shows a sharp decrease upon heating above the phase transition. The electron mobility in DIP crystals along the *c'*-direction was found to be higher than the hole mobility by almost an order of magnitude over the entire temperature range.

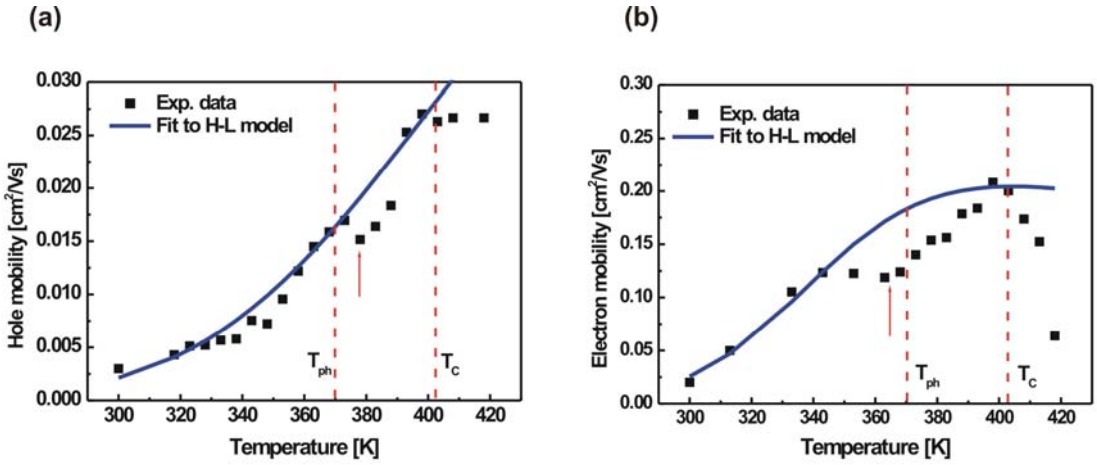

Figure 6.2 *Temperature dependent TOF mobility for* ***(a)*** *holes and* ***(b)*** *for electrons. Blue lines represent the fit to the Hoesterey-Letson model and vertical dashed red lines indicate onset of the phase transition (T_{ph}) and phase transition (T_c) temperatures estimated from the X-ray data respectively. For holes (electrons) a characteristic trap energy E_t of 310 meV (450 meV), relative trap density of 2×10^{-4} (2×10^{-7}) and a room temperature intrinsic mobility of 0.1cm^2/Vs (0.4cm^2/Vs) are attributed to the H-L model.*

The temperature dependent mobilities exhibit a complex behavior, i.e. a general trend of increase with temperatures up to 400 K accompanied by anomalies around 370 K. We do not observe a clear band-like transport, i.e. a defined T^{-n} dependence in these DIP crystals, which might be due to trace amounts of chemical impurities or the structural defects generated by the phase transition during the crystal growth still causing significant trapping of the charge carriers. In the following we will try to describe the

temperature dependent mobility behavior in the framework of multiple-shallow-trapping and release and thermally activated transport models respectively.

Multiple shallow trapping and release model

Guide-to-the-eye curves (blue lines) describing qualitatively a multiple shallow trapping and release behavior (*equation 2.32*), also known as Hoesterey-Letson model, are included in *figures 6.2 (a) and (b)*. In case of holes, a room temperature intrinsic mobility of ~ 0.1 cm^2/Vs, a relative trap density of ~ 2×10^{-4} and a characteristic trap energy of ~ 310 meV is attributed. Whereas for electrons a room temperature intrinsic mobility of 0.4 cm^2/Vs, a relative trap density of 2×10^{-7} and a characteristic trap energy of 450 meV is adjusted. Above parameters are adjusted in order to get the best fit to the experimental data. One can observe a deviation from this standard model, especially at temperatures around ~ 370 K, i.e. the onset of the phase transition.

Although the exact microscopic mechanisms responsible for the observed temperature dependence of the transport can not be directly inferred from the TOF data due to the anomalies caused by the structural phase transition, we will present a correlation between structural and electronic properties as following:

In a dynamic picture i.e. considering the temporal effect of structural changes on moving charge carriers, the onset in the decrease in mobility, indicated by the arrows in figures. *6.2 (a) and (b)*, can be attributed to thermally induced structural fluctuations within crystal lattice accompanying the phase transition [138]. The coherence length of the crystalline solid will strongly depend on the thermal fluctuations, leading to effective scattering of charge carriers at the respective grain boundaries. Also, as we have seen in Chapter 5, various libration modes of DIP molecules change with increasing temperature including a discontinuity at the phase transition temperature of 403 K. Assuming the presence of electronic transport bands, charge carrier mobility would be strongly affected by the symmetry breaking due to the phase transition, polaronic band narrowing [53], and large molecular motions e.g. librations. Considering electron-phonon coupling, theoretical calculations infer that the largest contribution to the lattice relaxation energy comes from the lowest frequency modes due to their stronger coupling to charge carriers

[139,140]. Therefore, temperature dependent librations would cause a deviation to lower mobility values assuming standard band-like or hopping transport models, as observed.
In a static approach, the continuous formation of smaller grains corresponding to a metastable phase, as discussed in Chapter 5, as well as to the *High-T* phase might result in an enhanced trapping of charge carriers at the grain boundaries, resulting in the anomaly in the temperature dependent charge carrier mobility. As shown in the *figure 5.7*, the integrated Bragg peak intensities corresponding to the *Low-T*, *High-T* and the metastable phase around 370 K is only ~ 30% of the integrated Bragg peak intensity corresponding to the *Low-T* phase at room temperature or the *High T* phase at ~ 400 K indicating a temporary loss of crystallinity and therewith increase of domain boundaries and amorphous sample fraction around 370 K, which is reflected in the TOF electron and hole mobilities around this temperature. On completion of the phase transition above 403 K, in case of electrons the mobility decreases by approaching its intrinsic temperature dependence and remains almost temperature independent for holes presumably due to the balance between thermally induced detrapping and intrinsic band-like transport.

Thermally activated transport

As we have seen in the previous section, the temperature dependent mobility behavior exhibits strong deviation from the Hoesterey - Letson model and a qualitative analysis leads to big errors by fitting the experimental data to H-L model. Therefore in this section we shall try to explain the mobility behavior in the framework of thermally activated transport, as explained in Chapter 2.
Figure 6.3 shows the temperature dependence of the hole mobility in the temperature range between 300 K to 410 K. An error bar of 20 % of the mobility value has been attributed, which includes the uncertainty in thickness measurements, change in effective thickness due to the absorption of the laser pulse across the sample, and the uncertainty in the kink position due to the blurring of the signal. As discussed before, mobility behavior in the high temperature regime deviates from the standard thermally activated transport presumably due to the formation of metastable phases during the phase transition. However, the hole mobility shows a monotonic increase up to 370 K, following the

thermally activated behavior. Also, as seen in Chapter 5 (*section 5.1*), orientation of the crystallites in the low temperature phase remains almost constant and well defined up to 370 K and therefore studies of the mobility behavior in this temperature range prove to be more reliable. We have observed a thermally activated behavior over the temperature range of 300 K– 370 K given by *equation 2.24*.

Considering the small crystallite size, estimated from the width of the Bragg peak, thermally activated transport is favored over band-like transport in this system as charge carriers have to frequently overcome the energy barriers caused by grain boundaries and hence distorting the band-like transport. From the fit we have estimated an activation energy (E_a) of 230 (± 20) meV, which could be attributed to the energy barriers caused by grain boundaries. These energy barriers could be realized as increasing of the bandgap at grain boundaries due to the broken translational symmetry. Activation energies close to this value have been observed in several organic thin films, e.g. DIP [28], pentacene, sexithiophene (α-6T), and quarterthiophene (α-4T) [141,142].

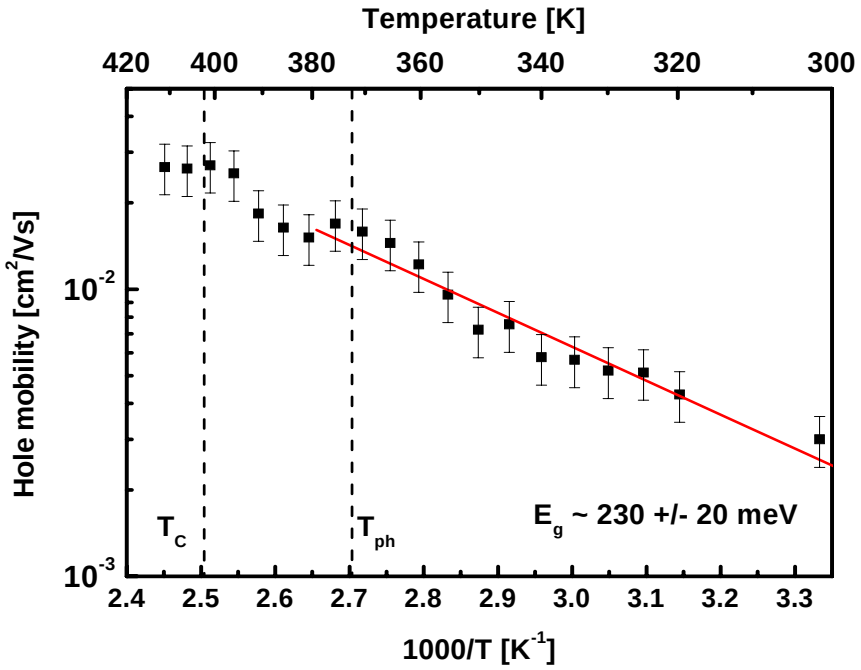

Figure 6.3 *Hole mobility as a function of temperature. Red line indicates the fit to the thermally activated mobility behavior given by equation 2.24.*

The thermally activated model does not fit very well for the electron transport as the transport phenomena for electron might be even more complicated, probably due to the fact that apart from the structural phase transition, coupling of electrons to librations or translations is different compared to holes.

We can conclude that no strong evidence of band-like transport was observed in DIP crystals and the temperature dependent mobilities exhibit a thermally activated behavior, at least for holes.

6.2 SCLC measurements

Charge carrier injection into the organic semiconductor is an important step towards the realization of an organic electronic device such as an FET. In this section we report on the electronic transport along the *c'*-direction studied by current-voltage (*I-V*) measurements in sandwich geometry. Measurements were performed on several crystals of varying thickness between 20 – 50 μm. Extraction of the transport parameters such as the mobility from the *J-V* characteristics is discussed in the Chapter 4 (*section 4.2.2*).

Temperature dependent J-V characteristics

Figure 6.4 shows the current density *J* as a function of the applied voltage *V* obtained on a 50 μm thick sample at 408 K.

The sublinear behavior that occurs at low voltages is the indication of low injection from the electrodes, further increase in the applied voltage results in space charging and the current increases with $\sim V^{2.6}$ (the exponent varies between 2.1 – 2.6 for different temperatures). Once all deep traps corresponding to a given trap level are filled, the current density shows a total jump ΔJ. Further increase in the voltage leads to a trap free SCLC regime with current showing a power law dependence of $V^{2.2}$ (V^2 for ideal SCLC behavior). Also, one can observe two discrete jumps ΔJ_1 and ΔJ_2 in the *J-V* characteristics which presumably indicate two discrete trap levels present in the DIP volume. We observe two trap-filling-voltages $V_{TFL,1}$ and $V_{TFL,2}$ corresponding to these two discrete trap levels, as indicated in *figure 6.4*.

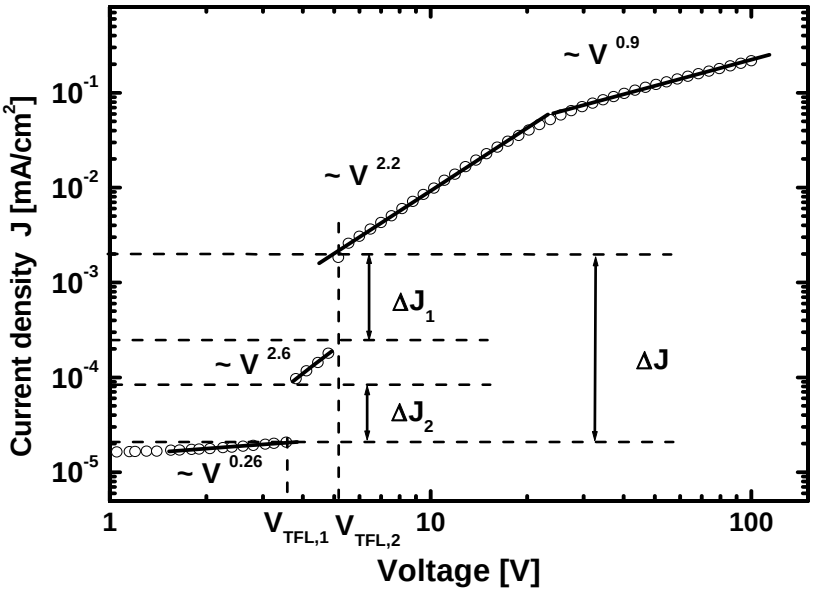

Figure 6.4 *J-V characteristic in DIP crystals at 408 K. ΔJ, V_{TFL} and various regimes with different V dependence have been indicated.*

The onset of trap-free SCLC regime is denoted as $V_{TFL,2}$. In the trap free SCLC regime one can estimate the mobility of charge carriers in the bulk by using the equation [143]

$$\mu_{\min} = \frac{8}{9}\frac{Jd^3}{\varepsilon_0 \varepsilon_r V^2} \quad . \qquad 6.1$$

Where J is the current density through the sample at an applied voltage V, d is the thickness of the sample, and ε_r is the dielectric constant of the semiconductor. Here we have used μ_{min} as lower limit of the mobility because the estimation of mobility by injection dependent methods, especially in case of organic semiconductors, are sample specific because of the individual mismatch between the metal Fermi level and HOMO/LUMO levels of the organic semiconductor. For the same reasons, we could not observe any electron transport in *J-V* characteristics. The trap free SCLC limit may not be reached due to an insufficient amount of charge carriers to fill all trap states and therefore a mobility estimated from *equation 4.18* will always be less than the intrinsic mobility in this transport regime.

Figure 6.5 shows *J-V* characteristics at various temperatures. As can be seen, the current initially follows a sub-linear increase followed by the trap filling and a trap filled SCLC regime with a slope ~ 2 is obtained on further increase of the voltage.

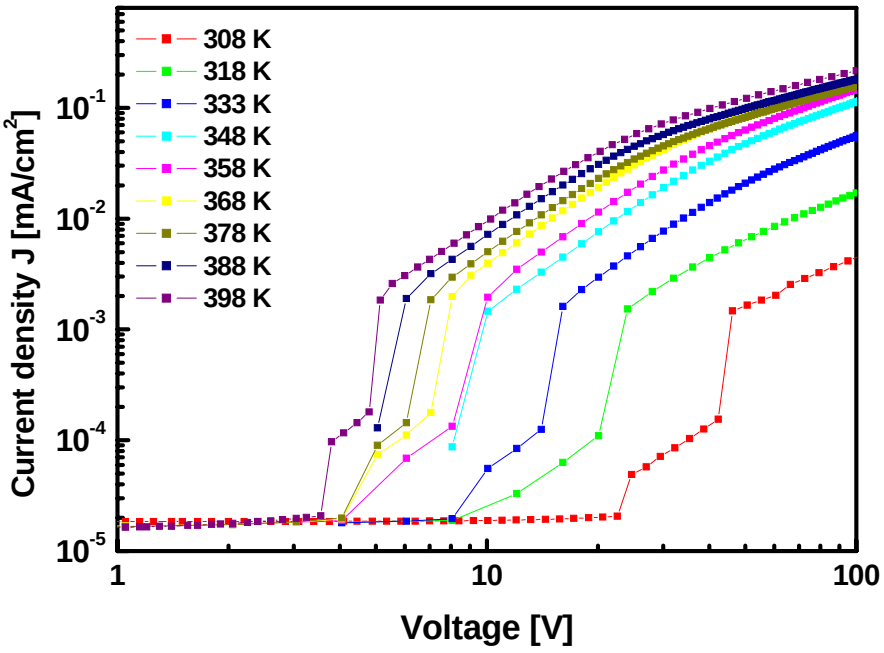

Figure 6.5 *J-V characteristics in a DIP crystal for different temperatures in the range of 300 – 400 K.*

At higher voltages, current shows a change of slope, e.g. deviation from the trap free SCLC behavior. This deviation becomes more prominent with increasing temperatures and it could be attributed to the poor injection of charge carriers. The effective mobility and hence the drift velocity of charge carriers would increase with the temperature which would result in decrease in the built-in potential as number of accumulated charges would decrease at elevated temperature, resulting in deviation from the standard SCLC behavior. The initial jump in current density (ΔJ_1 as indicated in the *figure 6.4*) increases with increasing temperature whereas the net jump (ΔJ) remains almost constant over the entire temperature range.

Temperature dependent SCLC hole mobility

Figure 6.6 shows the hole mobility as a function of temperature measured by the SCLC method. The minimum limit of the hole mobility was estimated using *equation 6.1* from the maximum current corresponding to the maximum voltage at a given temperature. Similar to the temperature dependent TOF hole mobility, SCLC hole mobility shows the signature of the structural phase transition. The mobility increases with the increasing temperature and shows a drop around the onset of the phase transition at 370K, as indicated by the arrow in *figure 6.6*. The mobility increases on further increase in the temperature. A lower limit of the room temperature hole mobility estimated from the trap-free SCLC regime yields to $\mu_h(RT) \sim 2\times10^{-5}$ cm^2/Vs which increases by more than two orders of magnitude to 5.5×10^{-3} cm^2/Vs at ~ 400K.

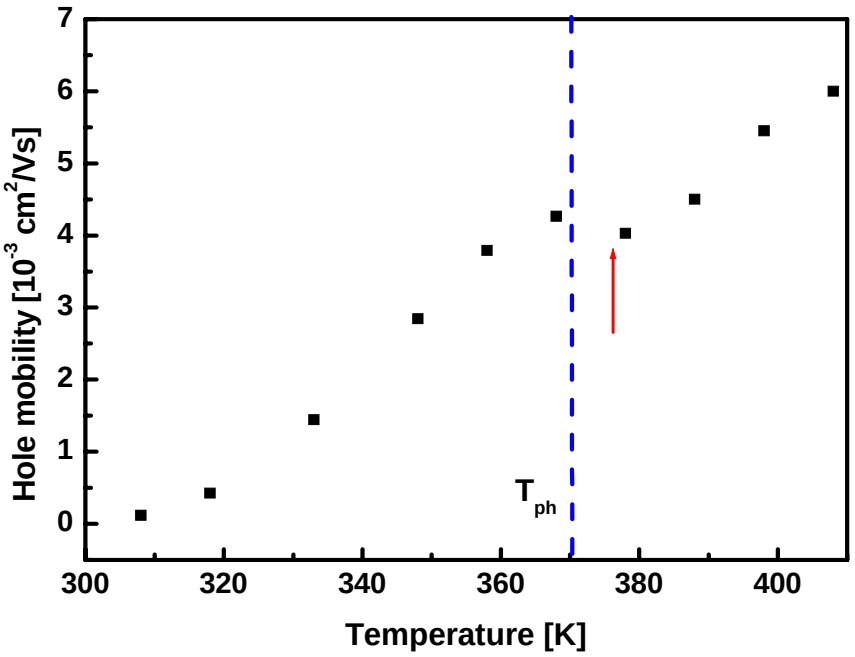

Figure 6.6 *Temperature dependent hole mobility estimated from the SCLC curve. The blue dashed line represents the onset of the phase transition at 370 K.*

Thermally activated SCLC behavior

Monotonic increase of the hole mobility, except the anomalies due to the phase transition, with increasing temperature suggests a thermally activated transport mechanism, similar to the TOF hole mobility as reported in the previous section. *Figure 6.7* shows the hole mobility as function of temperature. The mobility behavior clearly deviates from a thermally activated process described by just one exponent (*equation 2.24*). In a simplistic approach, we can split the temperature dependence of the mobility into two temperature regimes. In the low temperature regime (300 K – 360 K) the mobility exhibits a thermally activated behavior with an activation energy of 820 ± 80 meV whereas at elevated temperatures the activation energy reduces to 120 ± 20 meV.

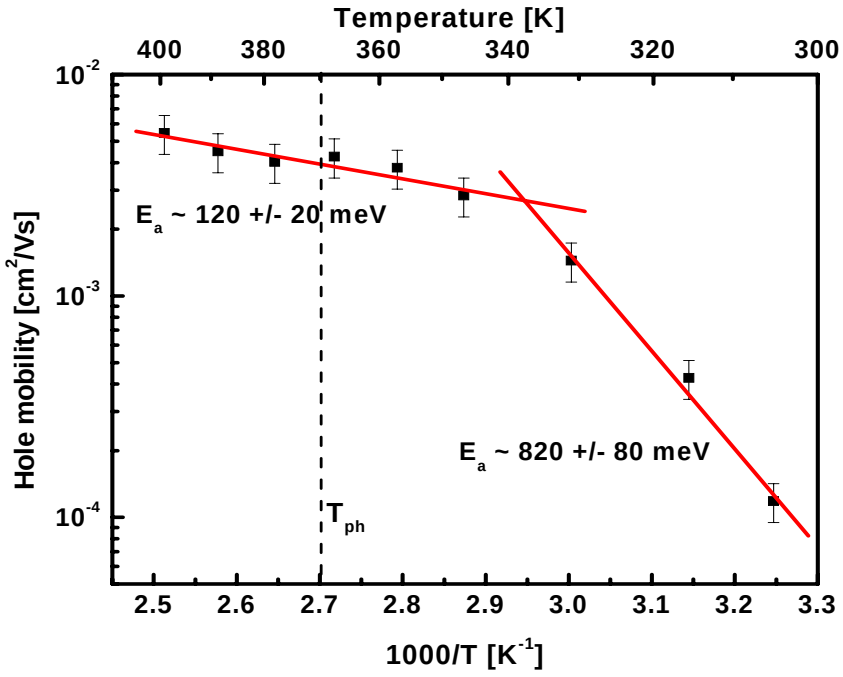

Figure 6.7 *Hole mobility as function of temperature estimated from the SCLC regime. Red lines show the exponential fit to the experimental data and dashed line indicates the onset of the structural phase transition at 370 K.*

Observation of two different activation energies can be attributed either to the phase transition or to the metal-organic interface. We discuss both scenarios in the following:

Activation energy and DIP polymorphs

As we have seen in Chapter 5, DIP undergoes an enantiotropic phase transition from the triclinic *Low-T* phase to the monoclinic *High-T* phase at 403 K with an onset of the phase transition at 370 K. The phase transition can affect the thermally activated transport by the subsequently described mechanism.

The *High-T* monoclinic phase has a more upright molecular orientation along the *c'*-direction compared to the *Low-T* triclinic phase. As shown in the *figure 5.14*, libration L_1 along the long molecular axis is increased by almost 30% compared to the *Low-T* phase. This increased librational amplitude along the *c'*-direction might contribute to the energy of charge carriers localized on the molecules and therefore would reduce the effective energy barrier to hop from one site to another.

However, this argument must be taken critically as it is not well known whether hopping between inter-molecular sites or hopping from one grain to another grain is the limiting factor for the resulting temperature dependence of transport behavior.

Activation energy and metal organic interface

An alternative explanation for the different activation energies can be given by considering the fact that the metal-organic interfaces impose a barrier for charge carrier injection due to the mismatch between the metal Fermi level and the HOMO/LUMO levels of the organic semiconductors. In case of DIP, the mismatch between *Ag* Fermi level and HOMO of DIP could be as large as 1.7 eV (1.5 eV at *Au*-DIP interface on a 30 nm thick film) [144]. Besides this energy barrier, there are interface dipoles and interface trap states, which can further enhance or reduce the injection barrier by up to approximately 1 eV [145] and strongly influence the injection dependent currents in the

SCLC and FET experiments.[†] Therefore, at lower temperatures energy barriers and trap states at the interface might play a dominating role. However, at elevated temperatures, interface trap states might be reduced due to annealing effects [146]. Furthermore, it has been shown that metal (*Au*, *Ag*) diffuses into the crystalline DIP films even at moderate temperatures (~350 K) [136,147]. Diffusion of metal into the organic crystal surface might facilitate the injection of the charge carriers into the crystals via electric field enhancement and hence at elevated temperatures mobility is mainly influenced by bulk states, resulting in lowering of the "effective" activation energy. Diffusion of the metal into the organic layers is an irreversible process and the effect should be observed even after cooling down the sample. However, it was not possible to perform control measurements due to the irreversible structural damage of the DIP crystals caused by the structural phase transition.

The observed changes in the activation energy are most likely combined effects of the above described. In order to understand the effect of interface and bulk traps on the hole mobility, we present the quantitative analysis of traps in DIP crystals extracted from the temperature dependent *J-V* curves.

Quantitative analysis of traps states

The density of traps affecting the electronic transport reduces with the increasing temperature due to the thermal release of charge carriers from the trap states, which lie within the range of the thermal energy. Therefore, $V_{TFL,1}$ and $V_{TFL,2}$ decrease with the increasing temperatures, as it becomes evident from *figure 6.5*.

A quantitative analysis of bulk and interface traps has been performed by measuring the respective V_{TFL} and the corresponding relative jumps at different temperatures. As indicated by *figure 6.5*, there are two discrete jumps in the current densities, possibly resembling two different types of trap states. The density of effective deep traps was estimated by using *equation 4.22*. The trap density according to $V_{TFL,1}$ amounts to ~ 2×10^{12} cm^{-3} and that to $V_{TFL,2}$ amounts to ~ 4×10^{12} cm^{-3}.

[†] In case of DIP, most probably the interface dipoles are enhancing the hole injection and opposing the electron injection.

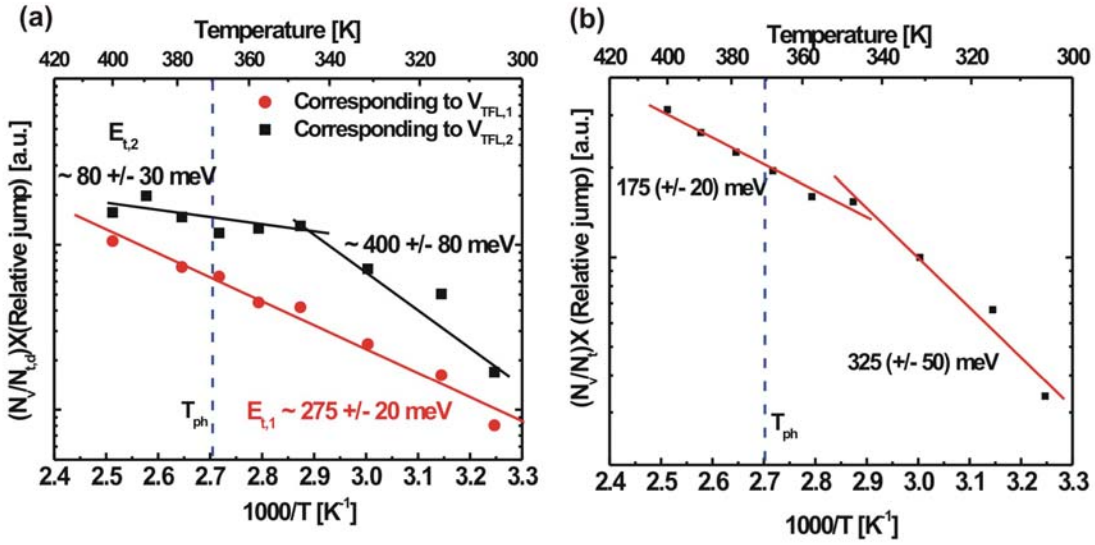

Figure 6.8 *Inverse of relative trap density (N_v/N_t) multiplied by the relative jump in the current density (ΔJ) as function of the inverse temperature.* ***(a)*** *Corresponding to two discrete jumps related to different trap states.* ***(b)*** *Assuming an effective trap density. The trap energy (E_t) is estimated from the slope of the curve. Red and black lines are exponential fits to the data and dashed blue lines indicates the onset of the phase transition at 370 K.*

Figure 6.8 shows the trap energies estimated from the relative jumps in the current as a function of temperature by using *equation 4.23* (see *section 4.2.2*). For that purpose we have plotted the inverse of relative trap density multiplied by the relative jump amplitude as a function of the inverse temperature.

Figure 6.8 (a) shows the trap energy estimated from two discrete jumps. We observe trap states at a characteristic energy of $E_{t,1}$ ~ 275 ± 20 meV corresponding to $V_{TFL,1}$. However, trap energies estimated from the ΔJ_2 at $V_{TFL,2}$ indicates the effect of two trap states with characteristic trap energies $E_{t,2}$ of ~ 80 ± 30 meV in the temperature range of 300 K – 360 K and of ~ 400 ± 80 meV in the temperature range of 360 K – 400 K.

In the above analysis, it has been assumed that the two discrete jumps in the current densities are independent of each other, i.e. these discrete traps are filled sequentially. However, in reality both traps will be filled simultaneously with population rates determined by the Boltzmann distribution. As this would result in an even more complex

analysis and as the estimated trap energies are in somewhat of the similar range, we have in a simplistic approach assumed an effective trap density, indicated by $V_{TFL,2}$ and the corresponding jump in the current density is attributed to the total jump ΔJ. *Figure 6.8 (b)* shows the trap energy corresponding to an effective trap state. We observe a non-linear behavior at lower temperatures followed by a straight line at elevated temperatures (on a semi-logarithmic scale). This could be attributed to the dominant effect of surface traps at lower temperatures, which significantly decrease with increasing temperature and eventually only bulk traps contribute to the *J-V* characteristics.

For temperatures above 360 K the fit results in a trap energy E_t of 175 ± 20 meV which is in reasonable accordance with the activation energy of 230± 20 meV obtained from the temperature dependent TOF data on DIP single crystals in the previous section. This trap energy could be attributed to the energy barriers imposed by grain boundaries in the bulk structure. From the fit to the data below 360 K we estimated an effective trap energy of ~ 325 (± 50) meV which averages over the effect of interface as well as bulk traps. The difference between the activation energy and trap energy (E_a = 820 ± 80 meV, and E_t = 325 ± 50 meV) in the low temperature regime (300 K - 360 K) is presumably due to the fact that in our current analysis we have considered the effective trap density instead of individual surface and bulk trap densities and therefore we estimate an effective trap energy. Comparative activation energies obtained by TOF measurements and trap energies estimated from the high temperature regime (360 K – 400 K) of the SCLC hole mobility indicate that interface states and energy barriers are the two dominant reasons for the lower effective charge carrier mobility, especially at lower temperatures. At high temperature the transport is mainly governed by bulk states and grain boundaries effects and therefore the difference in mobilities estimated from TOF and SCLC methods decreases with increasing temperatures from two orders of magnitude at 300 K to a factor of four at 410 K.

6.3 FET measurements

Temperature dependent FET measurements were performed in high vacuum (~ 10^{-7} Torr) on different DIP crystals. As we have mentioned earlier, phase transition results in

structural damage of these crystals and very rarely we find crystal with sufficient dimensions and smooth surfaces with minimized defects. The mobility varies significantly from sample to sample due to these structural effects and the field effect is diminished further by damage of the crystals upon heating.

Output and transfer characteristics for holes in DIP FET

Figures 6.9 (a) and (b) show the drain and gate sweeps respectively at room temperature. Field effect for holes is clearly visible in the output characteristic. The hysterises occurring in the gate sweep indicates trap charges at the insulator-semiconductor interface [148]. Also, at low gate voltages, the transistors do not exhibit the ideal FET characteristics, i.e. the linear regime and saturation regimes are not very well defined. This could be attributed to surface traps and the energy barriers for the injection of charge carriers (in this case holes) at the metal organic interface.

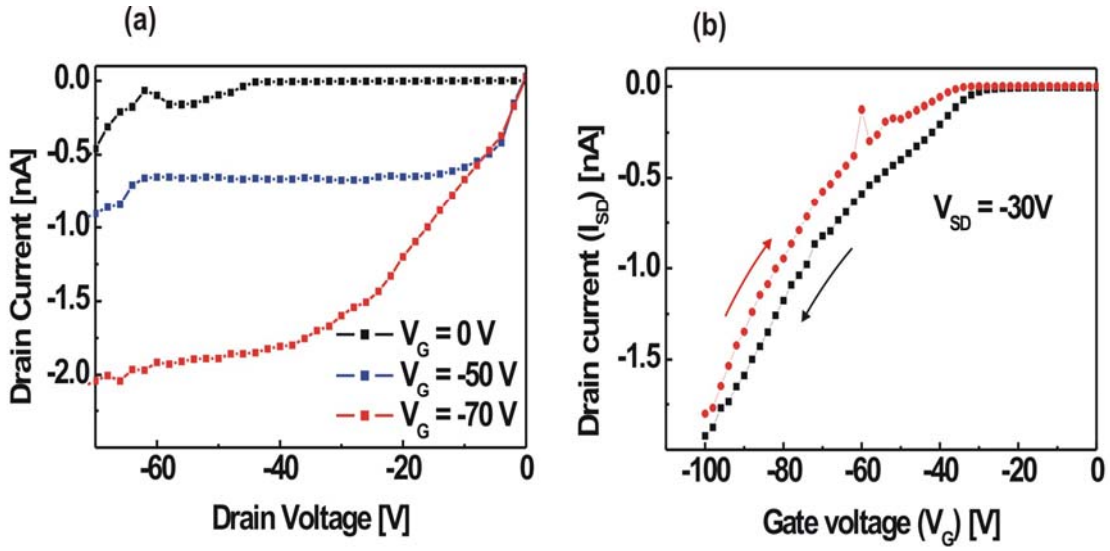

Figure 6.9 (a) *Drain sweep and* ***(b)*** *gate sweep at 300 K measured on a DIP single crystal FET with silver paste contact.*

However, at high gate voltages, the FET behavior becomes more distinct and one can estimate the mobility from the linear as well as from the saturation regimes. *Figure 6.10* shows the transfer characteristic at room temperature at a source-drain voltage of -30 V.

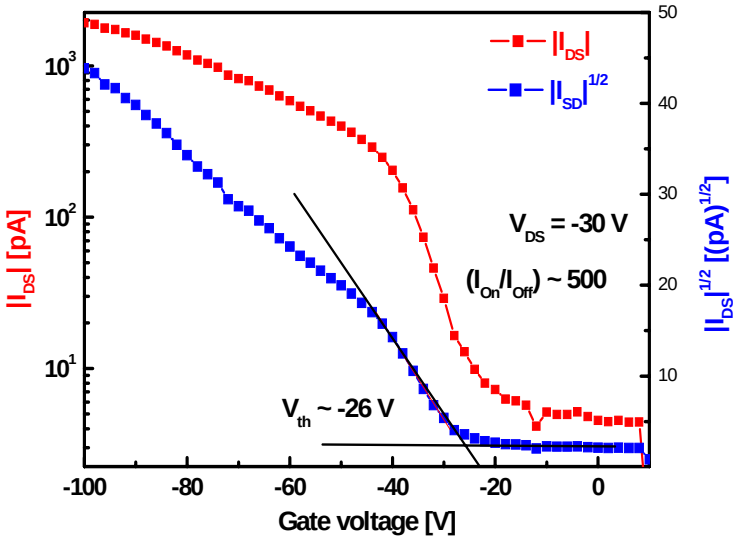

Figure 6.10 *Transfer characteristic at 300 K at a source-drain voltage of -30 V.*

At room temperature a threshold voltage (V_G) of about -26 V and an on/off ratio of ~ 500 are estimated. Also at high gate voltage, the square root of the source-drain current (I_{SD}) deviates and shows a sublinear behavior, which again suggests poor injection of charge carriers into the organic semiconductor.

T-dependent threshold voltage and trap density

The threshold voltage V_{th} is a measure of the amount of induced charges needed to switch on the electrical conduction in the FET. The magnitude of V_{th} depends on several factors such as density of charge traps at the insulator-organic interface, quality of source-drain electrodes etc. [121]. The density of deep traps at the gate insulator-organic interface can be calculated from the threshold voltage by applying *equation 4.25*. *Figure 6.11* shows the temperature dependent threshold voltage and density of deep traps.

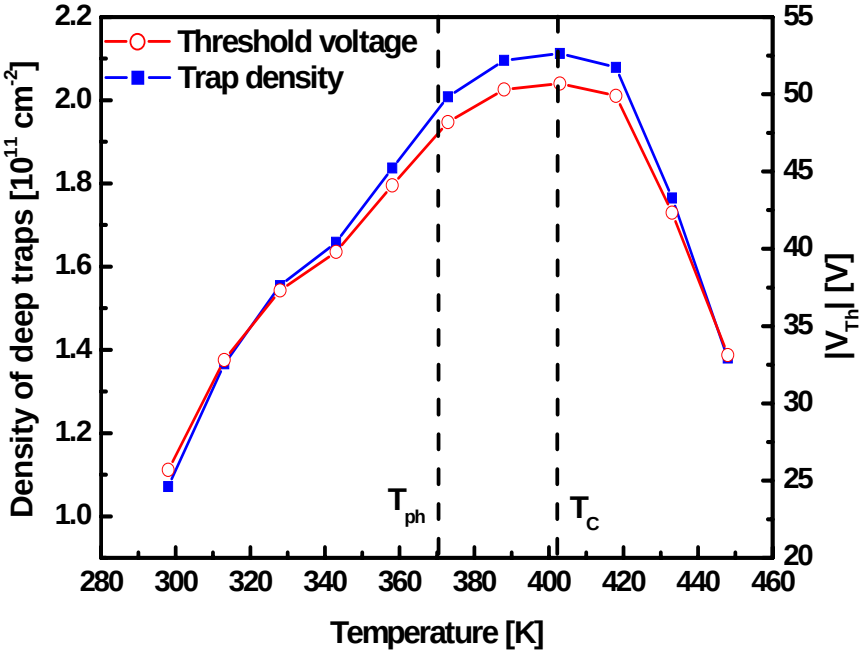

Figure 6.11 *Threshold voltage and interface trap density as a function of temperature. Dashed lines represent T_{ph} and T_c respectively.*

The density of deep traps and also the threshold voltage increase monotonically with increasing temperatures up to the phase transition temperature of ~400 K and afterwards both threshold voltage and density of deep traps show a sharp drop. At room temperature a deep trap density of nearly 10^{11} cm^{-2} is estimated which rises to 2.1×10^{11} cm^{-2} at 400 K and then drops to 1.4×10^{11} cm^{-2} at 450 K. For comparison, at room temperature a gate voltage of -70 V would accumulate ~8×10^{11} holes/cm^2 and nearly 12% of these accumulated holes will get trapped, which indicates the significant effect of deep traps on the electronic transport. The temperature dependent behavior of deep traps in the low temperature regime (330 K – 400 K) is not well understood as one would expect a decrease in the trap density with increasing temperature due to the de-trapping of charge carriers by thermal energy, e.g. as observed in rubrene single crystal OFET [149].

As a possible explanation, irreversible degradation in the device performance due to the leakage current through the gate insulator into the crystal surface results in an increased interface trap density [124] and hence resulting in larger threshold voltages. Also, the trap

density is increased by the occurrence of stress induced structural defects at the structural phase transition in, as mentioned in the Chapter 5. Therefore combined effects of electrically induced degradation and temperature dependent phase transition might cause the increase in the threshold voltage and trap density up to 400 K. Unfortunately, it was not possible to measure the leakage currents due to the restrictions imposed by the experimental set-up.

However, once the phase transition is completed and the thermally stable *High-T* phase is established for temperatures above 400 K, reduction of interface traps due to thermal annealing and enhanced injection of charge carriers into the semiconductor compete against the degradation caused by the leakage current, and finally result in an effective decrease in the threshold voltage as well as the trap density.

Gate voltage dependent hole mobility

Figure 6.12 shows the gate voltage dependence of the hole mobility at different source drain voltages.

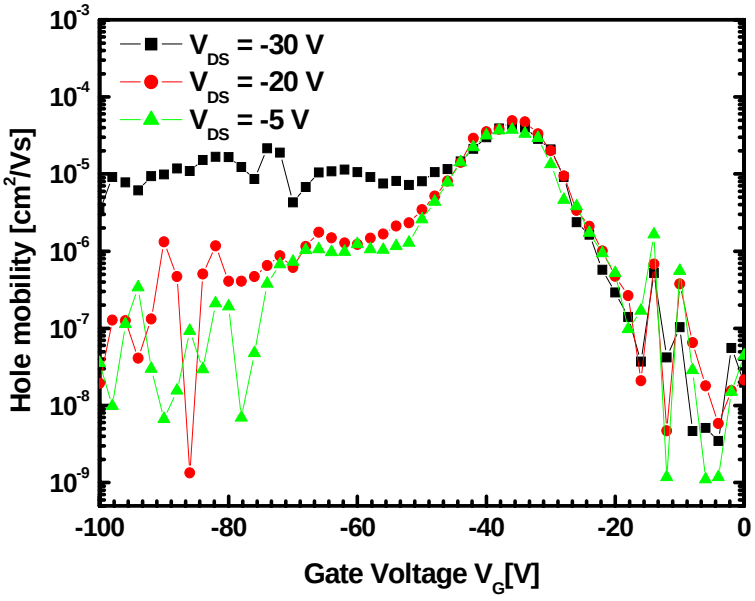

Figure 6.12 *Gate voltage and source-drain voltage dependent hole mobility for different drain-source voltages measured on a DIP single crystal FET at 300 K.*

The hole mobility increases with increasing gate voltage reaching the maxima for a gate voltage around -35 V and then decreases upon further increase of the gate voltage before reaching saturation at fairly negative gate voltages close to -70 V. Maxima in the gate voltage dependent mobility $\mu(V_G)$ and increase in the mobility with increasing source-drain voltage could be attributed to artifacts caused by the strong V_{th} dependence of the contact resistances at source and drain [150]. Therefore, in two probe geometry, the maximum in the mobility is in fact the minimum limit of the mobility (μ_{min}).

Temperature dependent hole mobility

As explained in the Chapter 4, the charge carrier mobility can be estimated from the linear (*equation 4.27*) as well as saturation (*equation 4.29*) regime of the temperature dependent FET characteristics. Temperature dependent hole mobilities estimated from the linear as well as the saturation regime are shown in the *figure 6.13*. The mobilities estimated from the linear regime is higher than those estimated from the saturation regime. However, both exhibit a similar temperature dependent behavior. Lower mobility in the saturation regime suggests that the FET does not reach complete saturation because of the poor injection of charge carriers due to the injection barriers formed at the source and drain electrodes. Therefore we shall focus on the temperature dependent behavior of the hole mobility estimated from the linear FET regime.

Hole mobilities in single crystals of DIP at room temperature are of the order of ~ 2×10^{-4} cm^2/Vs, which is almost three orders of magnitude lower than the hole mobility of 0.1 cm^2/Vs obtained on highly ordered DIP thin films [28]. However, the mobility depends strongly on the structural order and comparing the mobility values for the crystals with an effective rocking width of ~ 1.48° (see *section 5.1*), with that of DIP thin film transistors of similar structural order one finds that hole mobility is of similar order, i.e. ~ 10^{-4} cm^2/Vs to 8×10^{-5} cm^2/Vs for corresponding rocking widths between 1.25° to 1.7°.

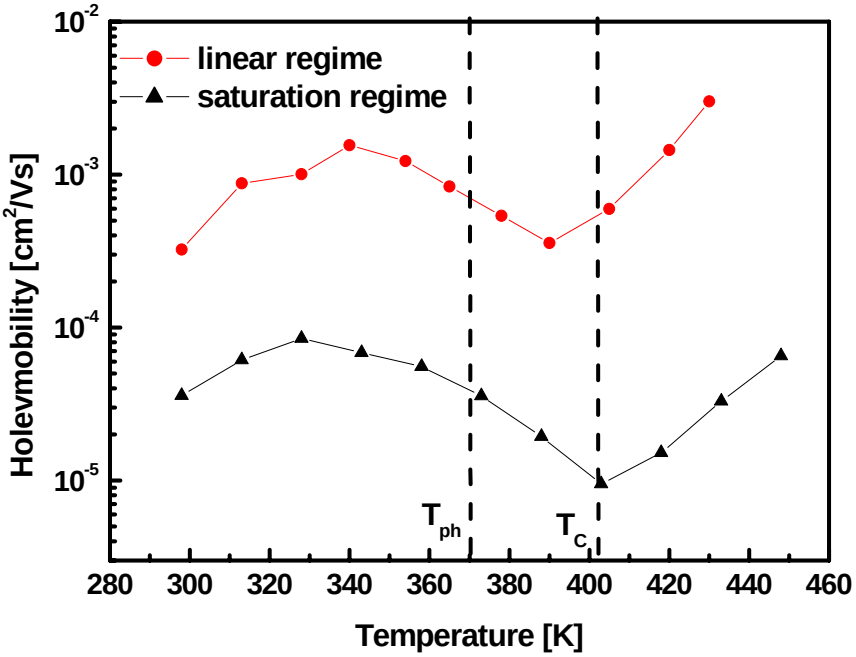

Figure 6.13 *Temperature dependent hole mobility in single crystal DIP FET estimated from the saturation and linear regime respectively. Dashed lines represent T_{ph} and T_c respectively.*

Besides the structural order, thin films of DIP have the similar structure as the *High-T* phase of DIP single crystals. For an adequate comparison, hole mobilities in DIP TFTs at elevated temperatures ($T > T_c = 403$ K) must be compared to that of hole mobilities in DIP single crystal FETs at same temperatures. M. Münch achieved a hole mobility of ~ 10^{-2} cm^2/Vs at ~ 440 K on a high quality DIP TFT with a rocking width of ~ 0.04° [28]. Compare to that we observed a hole mobility of ~ 3×10^{-3} cm^2/Vs at 440 K in DIP single crystal FETs. These values are quite comparable, however, subdued performance of DIP single crystal FETs might be a consequence of the formation of cracks at the crystal surfaces due to the structural phase transition.

The hole mobility increases upon increasing temperature and then shows a decrease around the phase transition, a similar behavior that was observed in TOF and SCLC measurements, as mentioned in *sections 6.1* and *6.2*. This anomalous behavior could be

attributed to thermal disturbance induced by the formation of metastable phases formed during the process of phase transition.

Once the complete phase transition is achieved (T > 403K), mobility shows a relatively steep increase upon further increase of temperature and rises to 3×10^{-3} cm^2/Vs at ~ 440 K. This stronger temperature dependence is related to the better overlap of molecular orbitals due to the change from the triclinic, which has larger in-plane lattice spacing, to the monoclinic crystal structure with shorter in-plane lattice spacing (*Table 5.1*). Also, the coordination number changes from *Z=2* to *Z=4*. The higher coordination number in the *High-T* phase suggests better packing of molecules compared to the *Low-T* phase and hence resulting in improved electronic transport characteristics.

6.4 Comparative study of TOF, SCLC and FET mobilities

Figure 6.14 (a) shows the temperature dependent TOF, SCLC and FET hole mobilities. As can be seen, the hole mobilities estimated from TOF, SCLC and FET method show similar kind of temperature dependence, i.e. thermally activated mobility with anomalies around the phase transition. However, the decrease in the FET mobility starts already at lower temperature (~ 350K) compared to TOF and SCLC measurements where the decrease starts at around 370K. This is possibly due to the fact that the in-plane structure is more sensitive towards the phase transition due to the herringbone packed layers of DIP molecules in the *(ab)*-plane. As it has been already reported in Chapter 5, the change in molecular conformation (libration, translation, twisting etc.) is a gradual process and shows a complete change at the phase transition temperature (403K). In order to illustrate the effects of the phase transition on the electronic transport, normalized hole mobilities with respect to respective room temperature mobilities are shown in the *figure 6.14 (b)*. As can be seen, TOF and SCLC hole mobilities show a monotonic increase with the temperature, except for a small regime (370 K to 385 K) around the on-set of the phase transition at 370 K where the mobility drops down slightly by ~ 20 %. Whereas the FET hole mobility is delicately affected by the phase transition and drops by almost a factor of six upon increasing the temperature from 340 K to 380 K.

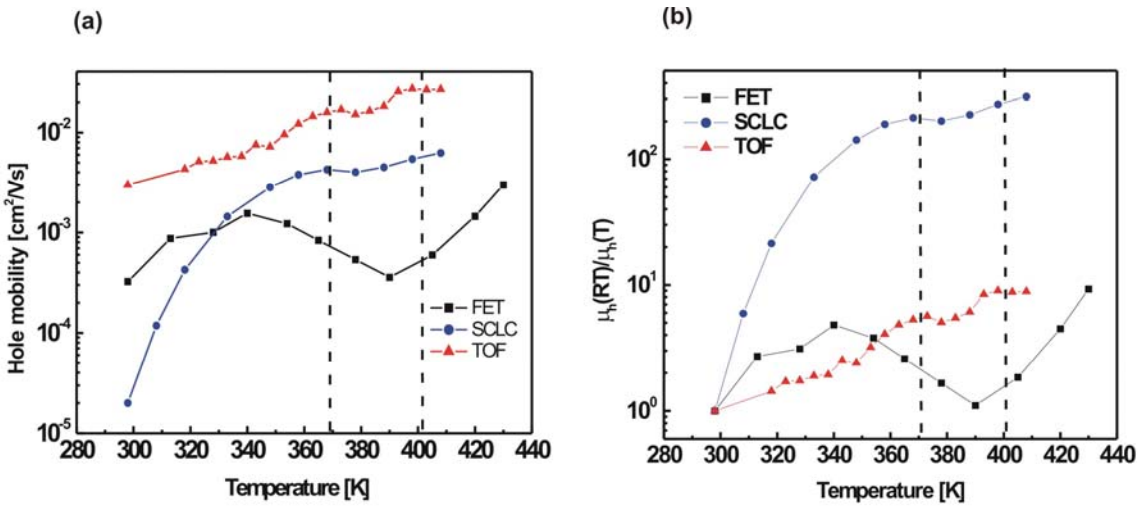

Figure 6.14 *Hole moblities estimated from TOF, SCLC and FET method as function of temperature on DIP single crystals.* ***(a)*** *Measured values, and* ***(b)*** *normalized with respect to the respective room temperature mobilities.*

Effects due to the metal-organic interfaces can be seen in the mobility behavior, as the hole mobility measured by the injection free TOF method is higher than both SCLC and FET mobilities over the entire temperature range. At lower temperatures interface traps play a stronger role and the SCLC mobility is lower than the TOF mobility by almost two orders of magnitude. The influence of interface traps decreases with increasing temperature, probably due to reduction in the effective trap density because of thermal release of the trapped carriers and the SCLC mobility reaches closer to the values estimated from the TOF measurements. The room temperature FET mobility is higher than the SCLC mobility by almost an order by magnitude presumably due to the better overlap of molecular orbitals as well as better packing of molecules in the *(ab)*-plane. Temperature dependent FET mobility shows a stronger correlation with the structural phase transition which is evident by the mobility behavior. Even though the room temperature hole mobility estimated by FET is one order of magnitude higher than the SCLC mobility, it drops down below the SCLC mobility for the temperatures above 350 K. However, once the phase transition is completed, it shows much steeper increase compared to SCLC mobility for T > 400 K.

6.5 Conclusions

Ambipolar transport is observed in DIP single crystals by the TOF method reflecting the chemically stable structure of DIP molecules which resist against photo-oxidation according to Clar's sextet rule. A room temperature electron mobility of 0.02 cm^2/Vs and hole mobility of 0.003 cm^2/Vs are estimated. The electron mobility was found to be higher than the hole mobility over the entire temperature range. Both electron and hole mobilities show anomalies around the on-set of the structural phase transition temperature at 370 K. The hole mobility exhibits a thermally activated behavior with an activation energy of ~ 230 ± 20 meV, which could be attributed preferentially to energy barriers induced at grain boundaries.

SCLC and FET measurements are performed over the temperature range of 300 K – 450K. Only hole transport could be observed in both methods due to the large injection barrier of ~ 1 eV for electrons at the *Ag*-organic interface, possibly along with interface dipoles further opposing the injection. Similar to the TOF measurements, temperature dependent SCLC and FET hole mobilities indicate anomalies around 370 K suggesting the strong correlation between electronic transport and structural phase transition in DIP crystals. The FET mobility shows a stronger correlation due to the better molecular orbital overlap and molecular packing in the *(ab)*-plane compared to the perpendicular *c'*-direction. The room temperature FET hole mobility amounts to ~ 2×10^{-4} cm^2/Vs, i.e. is almost an order of magnitude higher than the SCLC mobility. For temperatures above 403 K, i.e. in the DIP *High-T* phase, hole mobilities are smaller though comparable to those estimated in the DIP thin film transistors by M. Münch [28].

7 Characterization of DPA Crystals

In Chapters 5 and 6 we have studied the correlation between the electronic transport and the structure of DIP crystals. As expected from the UV-Vis spectroscopy, chemical stability of DIP enabled us to observe ambipolar transport by TOF. Motivated by those results, we have extended our studies on 9,10 diphenylanthracene (DPA) crystals, which not only shows the good chemical stability but also has an obvious advantage in comparison to other molecules by its thermal stability, i.e. melting without decomposition and thereby zone refinement and hence ultra-high purification can be achieved. TOF and X-ray measurements were performed on both Bridgman grown and vapor phase grown DPA crystals. First we will discuss the structural characterization by X-ray and single crystal diffractometry on Bridgman grown and vapor phase grown crystals and later we will present the TOF and *I-V* measurements on these crystals. Eventually, we will relate the electronic transport properties with the structural properties of these crystals.

7.1 Structural characterization of DPA crystals

X-ray measurements were performed on DPA crystals to achieve structural information of the electronic transport direction, crystallite size etc. along the out-of- plane direction. Single crystal diffractometry measurements were performed by Dr. T. Siegrist at Alcatel-Lucent to obtain the complete crystal structures of both Bridgman and sublimation grown crystals.

7.1.1 Single crystal diffractometry on DPA crystals

Bridgman grown DPA crystals

Single crystal diffractometry was performed on DPA crystals grown by Bridgman method. Crystals exhibit the monoclinic unit cell with a = 10.7 Å, b = 13.6 Å, c = 12.3 Å,

β = 90.5º, coordination number $Z = 4$, a unit cell volume of V = 1774.4Å^3 and space group *C2/c*, which is similar to the parameters obtained for solution grown DPA crystals [151].

The structural projection of the crystallographic *(bc)*- and *(ac)*-planes of DPA is illustrated in *figures 7.1 (a)* and *(b)* respectively, indicating the molecular packing of DPA molecules and the backbone-phenyl group overlapping. From these data we deduced a smallest C-C contact distance along the *c'*-direction of approximately 3.8 Å. For comparison, the shortest intermolecular distance between molecules along the *c*-direction in pentacene is ~ 3.94 Å and in tetracene it is ~ 3.86 Å [152].

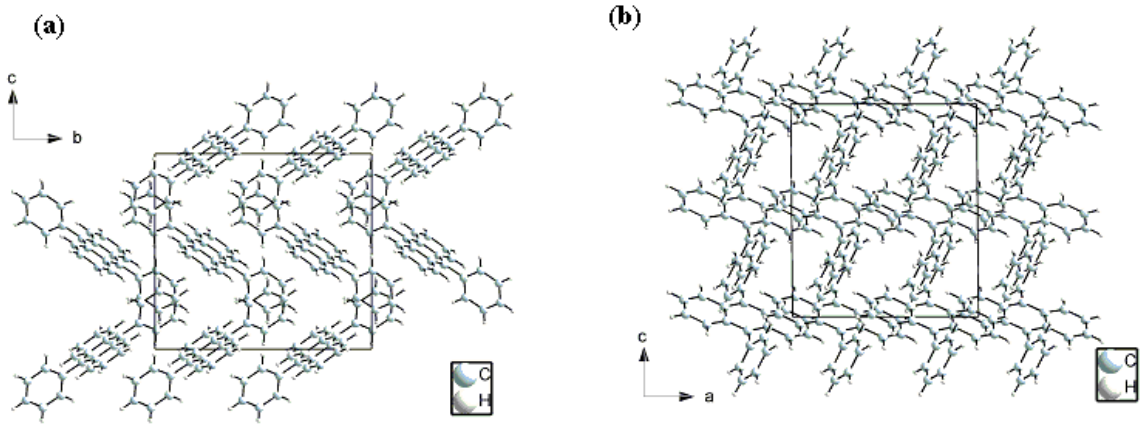

Figure 7.1 (a) *Projection of the (bc)- and* ***(b)*** *(ac)-plane of the DPA unit cell, estimated by single crystal diffractometry on Bridgman grown DPA crystals.*

The short *C-C* contact distance between phenyl groups attached to neighboring DPA molecules along the *c'*-direction is interesting as it might enhance the molecular orbital overlap and hence is expected to support good conduction properties. As can be seen in *figure 7.1* the phenyl-groups at the anthracene-backbone permit an efficient linking between the planes along the *c'*-direction.

Vapor phase grown DPA crystals

Single crystal diffractometry reveals that sublimation grown DPA crystals have a completely different symmetry and lattice parameters compared to that of Bridgman

grown crystals. Sublimation grown crystals form a monoclinic structure with unit cell dimensions a = 9.5 Å, b = 20.4 Å, c = 10.1 Å, β = 112.3°, coordination number Z = 4, a unit cell volume of V = 1808.8 Å^3 and space group *P2/a*. The structural projection of the crystallographic *(ab)*- and *(bc)*-planes of DPA in *figures 7.2 (a)* and *(b)*, respectively, indicate the molecular packing and the backbone-phenyl group contacts along the crystallographic *b*-direction. The nearest C-C contact distance between two phenyl groups of adjacent molecules along the *b*-direction is ~ 4.9 Å, i.e. almost 22% larger than that along *c'*-direction in Bridgman grown DPA crystals. *Table 7.1* summarizes the lattice parameters for Bridgman grown and sublimation grown DPA crystals.

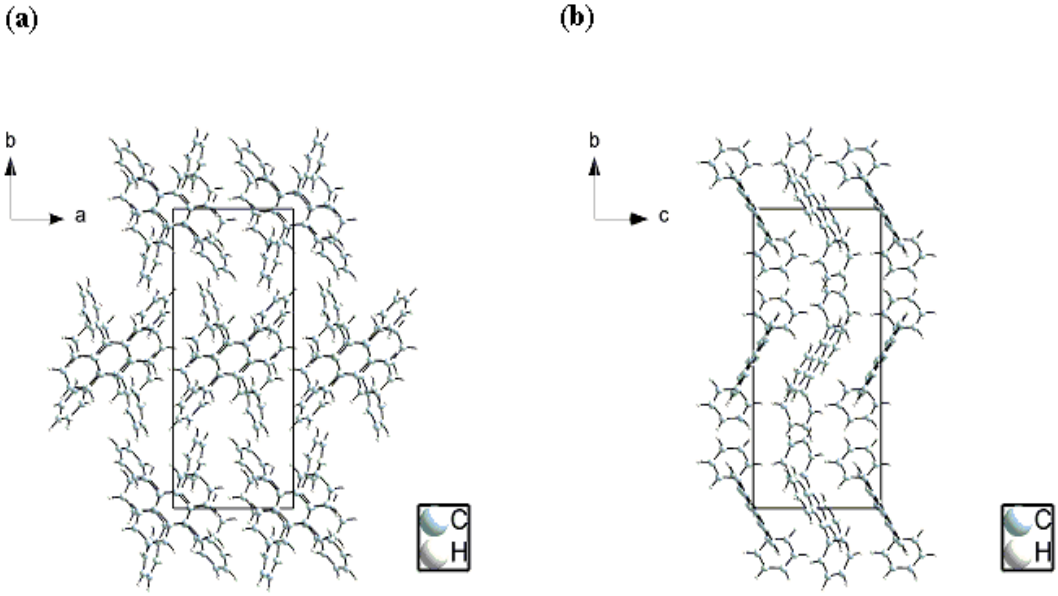

Figure 7.2 (a) *projections of (ab) and* ***(b)*** *(bc) planes of sublimation grown DPA crystals respectively.*

The different crystal structures obtained for sublimation grown and Bridgman grown crystals provide a reference system to correlate the intrinsic transport properties to the structural properties. This will be investigated in the framework of TOF measurements in the *section 7.2*.

Table 7.1 *Lattice parameters corresponding to DPA crystals*

	Bridgman grown DPA crystal	**Sublimation grown DPA crystal**
Structure	Monoclinic	Monoclinic
Space group	C 2/c	P2/a
Coord. No.	4	4
a (Å)	10.683	9.498
b (Å)	13.552	20.413
c (Å)	12.257	10.084
α (°)	90	90
β (°)	90.54	112.307
γ (°)	90	90
V ($Å^3$)	1774.4	1808.8

Monotropic polymorphism in DPA crystals

Monotropic polymorphs are defined by two or more different molecular packings, but with the polymorphs not transformable into each other at any temperature below melting or sublimation. The molecular packing in such polymorphs is often determined by the growth conditions, e.g. phase of the seed crystal, temperature, etc. DPA, therefore, is a monotropic polymorphic system, since there is no temperature dependent solid-to-solid phase transformation observed below the melting temperature of ~ 525 K and the crystal structure depends entirely on the growth conditions.

The irreversibility of monotropic phases of a given compound lies in the fact that the molecules cannot move or rearrange unless the overall motions needed for the phase transition are small, since the thermal energy available enables only small motion of molecules.

Usually in monotropic polymorphs, the molecular packings are significantly different so that small molecular reorientations do not transform one packing into the other. In DPA, the molecule is a cruciform, and the molecular packing allows two relative orientations:

1. Anthracene backbone on anthracene backbone and
2. Anthracene backbone on phenyl groups.

This means that there is a 90° rotation of the molecular entities necessary to transform between the two observed packings. It is therefore conceivable that the thermal energy

needed to rotate the molecules exceeds the melting temperature of any of the solid phases and a solid-to-solid phase transformation will not occur.

7.1.2 X-ray diffraction measurement on DPA crystals

Bridgman grown DPA crystals

Figure 7.3 shows the X-ray diffraction pattern measured on Bridgman-grown DPA crystals. X-ray diffraction measurements were performed in out-of-plane geometry with the momentum transfer along the surface normal, which coincides with the charge transport direction in the TOF experiments, as indicated in *figure 7.3 (a)*. Observed Bragg peaks correspond to the *c'*-direction with a lattice spacing of about 12.3 Å. This is in good agreement with single crystal diffractometry data since the angle $\beta = 90.5^{\circ}$ indicates almost orthorhombic crystal structure. Due to the space group symmetry, (*00l*) peaks are forbidden for odd-numbered *l*.

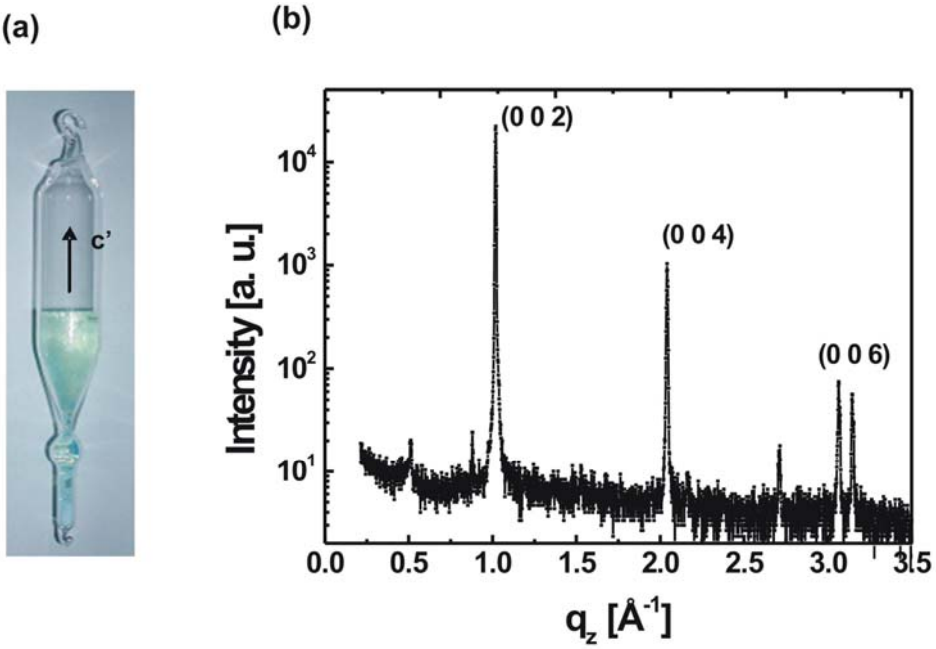

Figure 7.3 (a) *Image of a Bridgman-grown DPA crystal. The arrow indicates the orientation of the c'-direction.* ***(b)*** *Bragg diffraction pattern measured on a slab cut of the crystal in (a) with the surface normal along the c'-direction.*

Crystallite size of about 900 Å was estimated from the width of the second order Bragg peak using Scherrer formula (*equation 4.9*). Smaller crystallite sizes are the consequence of the poor thermal coupling between the crystals and the wall of the Bridgman ampoule, which results in stress fields within the crystals, finally released by the formation of structural defects such as dislocations and grain boundaries. Nevertheless, the high intensity of the Bragg reflexes indicates a good textured structure and a high charge carrier mobility would be expected in these crystals due to the good overlap between adjacent phenyl-phenyl groups along the *c'*-direction.

Sublimation grown DPA crystals

Figure 7.4 (a) represents the out-of- plane Bragg diffraction pattern measured on sublimation grown crystal.

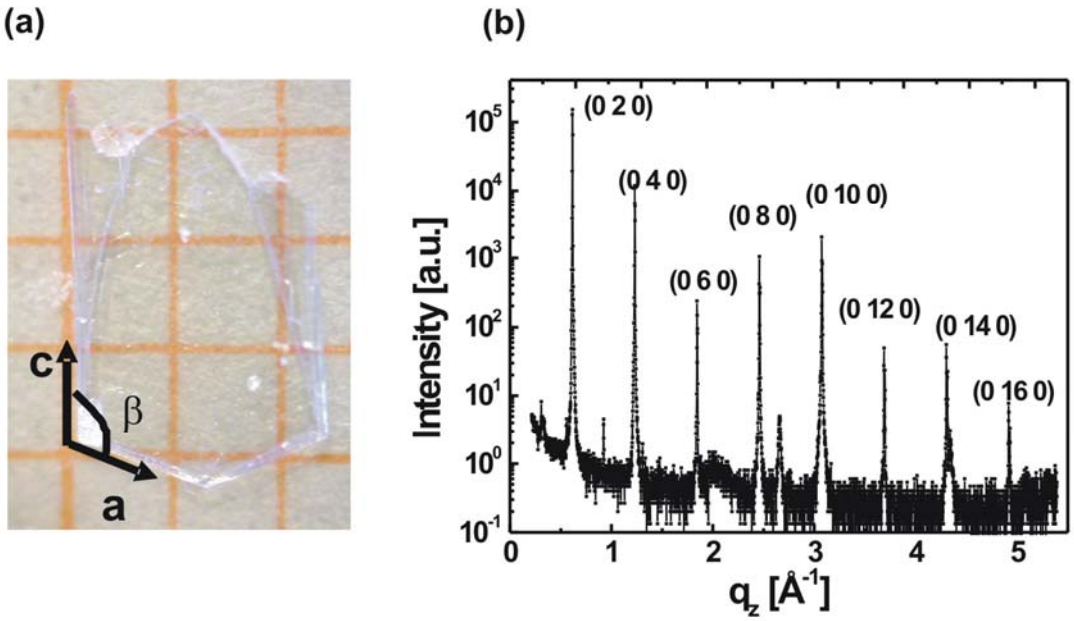

Figure 7.4 (a) *Optical image of a sublimation grown DPA crystal together with the unit cell vectors in the surface (ac)-plane.* ***(b)*** *The out-of-plane Bragg diffraction pattern indicates the crystallographic direction of the surface normal, which corresponds to the charge transport direction in TOF along the (010)-axis.*

The positions of the Bragg peaks correspond to a lattice spacing of ~ 20.4 Å. It is evident that the crystals grow in the crystallographic *(ac)*-plane with the surface normal (transport direction in TOF measurements) along the crystallographic *b*-direction. Only (*0k0*) peaks for even *k* were detected in the Bragg pattern due to the symmetry properties of the monoclinic unit cell.

As it can be seen in the *figure 7.4 (a)*, Bragg reflexes are of much higher intensity compared to the Bridgman grown crystals, and Bragg peaks even up to 16^{th} order could be observed in the diffraction pattern. The low damping of the peak intensities indicates the better quality of the sublimation crystals compared to that prepared by Bridgman growth and hence one can expect a smaller impact of structural defects on the electronic transport in these crystals.

Figure 7.4 (b) shows the optical image of a DPA crystal grown by sublimation from the vapor phase. It can be seen that crystal edges correspond to the crystallographic *a* and *c* directions respectively, that is, the surface normal is along the (*010*) direction, which is approved by the X-ray measurements discussed above.

The size of the crystallites along the *b*-direction was estimated to be 1600 Å, which is larger than the crystallite size in Bridgman grown crystals (~900 Å along *c'*-direction). As mentioned earlier, smaller crystallite size in Bridgman grown crystals is due to the structural defects generated by the interaction between the material and the wall of Bridgman ampoule, whereas in sublimation technique crystal growth proceeds freely in preferential directions, usually with the most dense plane stabilized due to its lower surface energy.

We performed rocking width measurements in order to further characterize the structural quality. *Figure 7.5* shows the rocking curve at the (*020*) Bragg peak. Sharp peaks in the rocking curve represent individual crystallites within the displayed angular range. However, the average distribution of crystallites within the grains results in an effective broadening of the rocking curve. We will refer this broadening as an effective rocking width.

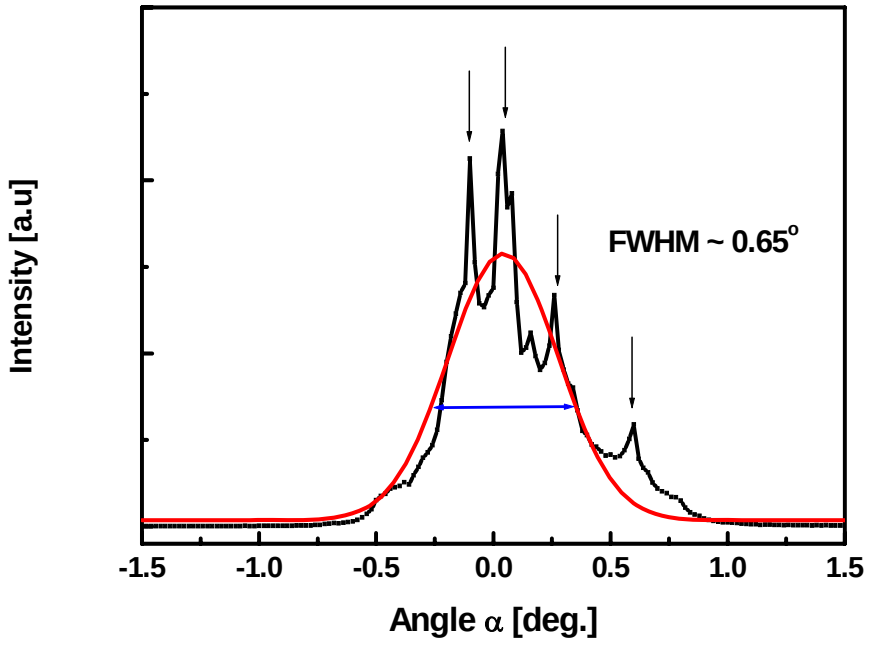

Figure 7.5 *Rocking curve around the (020) Bragg peak in a sublimation grown DPA crystal. Black arrows indicate peaks corresponding to crystallite fractions and red curve is the Gaussian fit to the experimental data.*

An *effective* rocking width of about 0.65° around the second order Bragg peak along *b*-direction was estimated from the FWHM of the Gaussian fit to the crystallite distribution. The effective rocking width is quite narrow compared to other aromatic organic crystals, e.g. DIP (see *section 5.1*) and tetracene [7]. Furthermore, the plane of highest density in the sublimation grown crystals corresponds to the (*ac*)-plane, hence one might expect a high field-effect transport in this plane, provided charge carriers could be injected into the crystals.

7.2 Electronic transport in DPA polymorphs

We have seen in the last sections that DPA posses monotropic polymorphs and that the crystal structure delicately depends on the growth method. In this section we will investigate the charge carrier mobility measured by TOF technique on crystals grown by Bridgman method as well as on those grown by the sublimation technique. Further we

will interpret the temperature dependent mobility behavior in the framework of standard transport models and will establish a correlation between electronic transport and the structural quality of the crystals. Eventually, we will perform a comparative study of the transport in Bridgman grown *vs*. sublimation grown crystals.

7.2.1 TOF on Bridgman grown DPA crystals

As discussed in Chapter 3, Bridgman grown crystals were cut by a thread-saw soaked with xylene to produce slabs of the desired thickness for TOF measurements and structural characterization. The thickness of the crystal slabs for TOF amounts to 0.9 to 1.2 mm at a lateral circular area of about 50 mm^2. The front electrodes for the TOF experiments were prepared by thermal evaporation of a 20 nm thick silver layer. For the TOF experiments the Nd:YAG pulsed laser was tuned to 266 nm wavelength and a pulse width of ~5 ns for the photo-generation of charge carriers at the crystal front was used. DPA has an absorption peak at 277 nm and the excitation at 266 nm is sufficiently absorbed within 10% of the total thickness of the DPA crystals and results in photo-generation of electron-hole pairs near the crystal surface.

As shown in the *figure 7.6 (a)*, we observe both electron and hole transits at room temperature in TOF measurements. The arrows mark the position of the transit kinks indicating the arrival of the charge carrier sheets at the opposite electrode. However, the electron transient kink is not clearly distinguishable over the entire temperature range presumably as residual impurities in the material, i.e. oxidation by-products such as diphenylanthracene-endoperoxide, might act as deep traps for electrons, resulting in blurred or dispersive TOF pulses. The electron mobility of ~13 cm^2/Vs at RT extracted from the observed transit signal is remarkably high for PAHs. The hole mobility estimated from the TOF signal amounts to ~ 3.7 cm^2/Vs at room temperature. Observation of both electron and hole transport at room temperature with relatively high mobilities is another central aspect for the investigation of DPA as a candidate for ambipolar transport in organic materials.

Figure 7.6 (b) shows the inverse of the hole transit time as a function of the applied voltage measured at RT. In agreement with the expected ohmic behavior at low electric

fields, the inverse transit time increases almost linearly with increasing voltage. The hole mobility extracted from the slope of the linear fit is 4.8 ± 0.1 cm^2/Vs and, thereby, shows an average deviation by at most 20% from the value at ~ 3.7 cm^2/Vs measured at 1000 V. These deviations are mainly attributed to spatial charging effects of the organic crystals by excessive photo-generation of charge carriers and/or unintentional injection at the metal-organic contact interfaces.

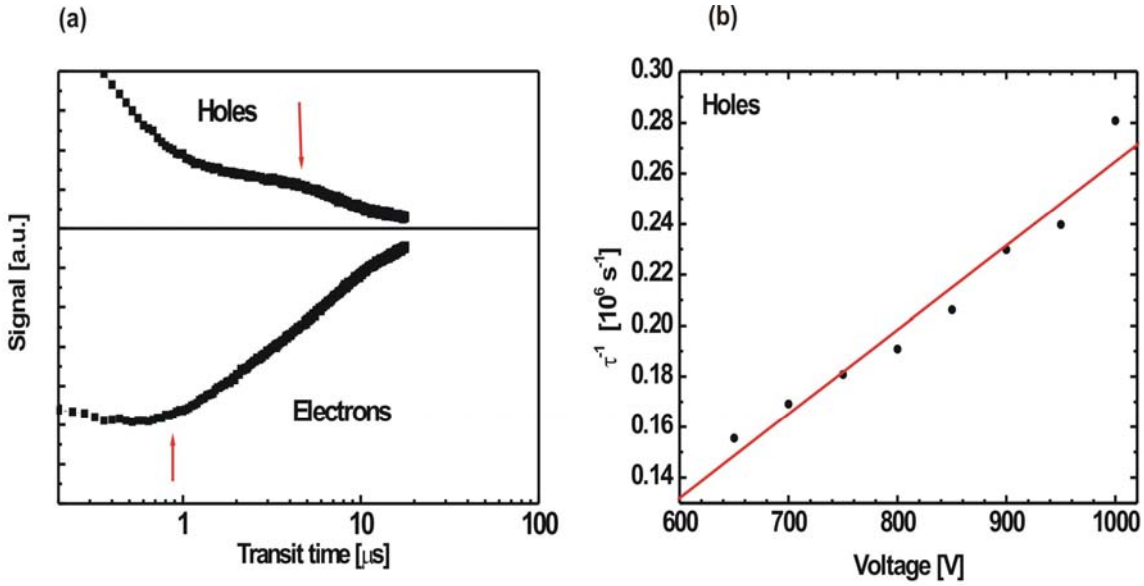

Figure 7.6 (a) *Characteristic electron and hole TOF signals at room temperature in Bridgman grown DPA crystals. Arrows indicate the position of transit kinks.* ***(b)*** *Inverse transit time, τ^{-1}, measured as a function of the applied bias voltage. According to the relation $\tau^{-1} \sim \mu V$ the hole mobility can be extracted from the linear slope of this curve (red line) and amounts to 4.8 ± 0.1 cm^2/Vs.*

T-dependent hole mobility in Bridgman grown DPA crystals

To analyze the underlying transport mechanism for holes in DPA we performed TOF studies at various temperatures between 5 K and 420 K. TOF transit signals for holes could be observed over the whole temperature range with a well-defined kink allowing for a reliable estimate of the mobility. As mentioned in the previous section, TOF pulses

for electrons were mostly blurred therefore it was not possible to achieve temperature dependent mobility data for electrons and to analyze them in detail.

The resulting $\mu(T)$ dependence for holes is shown in *figure 7.7* and is characterized by a monotonous increase of the mobility with decreasing temperature, followed by a saturation behavior starting at around 100 K.

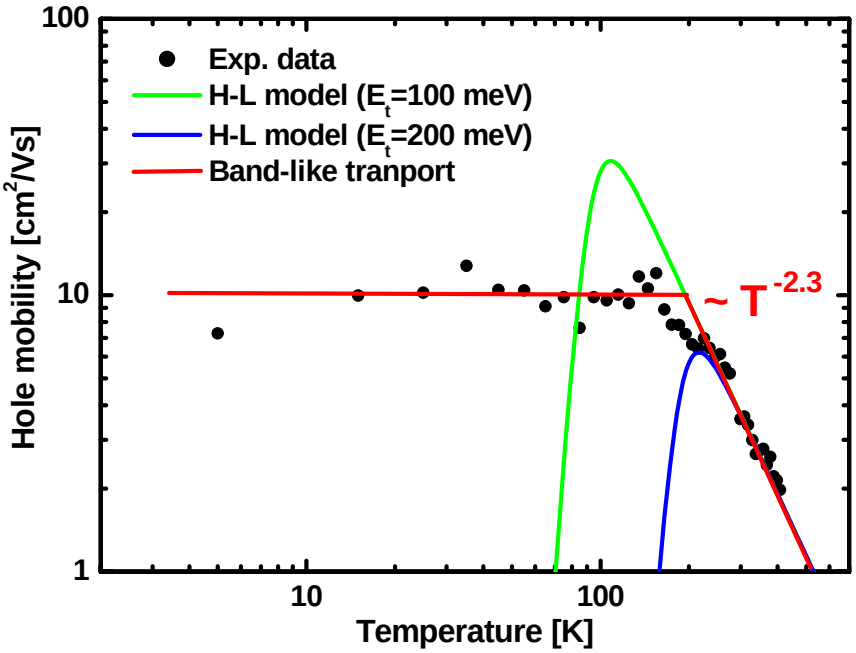

Figure 7.7 *TOF hole mobility as a function of temperature. Black circles are experimental results and the red line represents the mobility according to phonon affected band-like transport with n ~ 2.3. The blue and green lines are Hoesterey-Letson model curves with a relative trap density of ~5×10^{-7} and trap energies of 100 and 200 meV, respectively.*

As discussed in Chapter 2, from the linear decrease of log(μ) in the temperature range from 200 K to 380K we were able to reproduce the predicted T^{-n} dependence for intrinsic transport, yielding an exponent n of ~ 2.3. This exponent is in the range of those previously observed in high purity PAH single crystals, e.g. n = 2.8 for naphthalene, and it has been attributed to band-like transport limited by scattering, preferentially with

acoustic and optical phonons [29,53]. Significantly, RT hole mobility in DPA ($\mu_h(RT)$ ~ 3.7 cm^2/Vs) along the *c'*-direction is higher than that in naphthalene ($\mu_h(RT)$ ~ 1.5 cm^2/Vs) along the shortest crystallographic direction, i.e. the *a*-direction. In case of Bridgman grown DPA crystals, the *a*-direction is the shortest crystallographic direction, therefore we might expect a much higher mobility along this direction in ultra-pure DPA single crystals. However, efforts to cut and polish the Bridgman grown crystals with the surface normal along *a*-direction were not successful.

As we concluded from the X-ray crystal structure analysis, this higher hole mobility might result from an effective intermolecular linking between adjacent DPA (*00l*)-layers via the phenyl groups attached to the anthracene backbone.

The low temperature part of the hole mobility (see *figure 7.7*) is even more significant as it shows the trend to saturate with decreasing temperature, reaching a maximum mobility value of about 10 cm^2/Vs at 100 K.

Interpretation of T-dependent hole mobility behavior

To elucidate the conductivity mechanisms in DPA in more detail, the observed temperature dependence of the mobility will be analyzed in the context of three different scenarios: 1) an effective transport based on multiple-shallow-trapping and release of charge carriers according to the Hoesterey-Letson model, 2) a limitation of mobility by the mean free path determined by the grain size, and 3) an intrinsic band-like transport.

1. Hoesterey-Letson model

Assuming a multiple-shallow-trapping and release model as suggest by Hoestery and Letson [87] and discussed in Chapter 2 (see *section 2.7*), the observed saturation of the hole mobility at low temperature originates from a transition of thermally activated transport to an enhanced carrier trapping transport as the thermal energy is no longer sufficient to release holes from trap states above the DPA valence band. Using a Boltzman-distribution for the thermally activated de-trapping and values of 3.7 cm^2/Vs for the intrinsic hole mobility at 300 K and n = 2.3 for the temperature exponent,

estimated from the linear decrease of log $\mu(T)$ at elevated temperatures, we can rewrite *equation 2.32* as following

$$\mu_{eff}(T) = 3.7\left(\frac{T}{300K}\right)^{-2.3}\left[1+\frac{N_t}{N_0}\left\{\exp\left(\frac{E_t}{k_B T}\right)-1\right\}\right]^{-1} cm^2/Vs \qquad 7.1$$

To obtain a rough measure for the trap density, we adjusted this quantity from the crystallite size measured by the width of the Bragg peaks. Using the Scherrer formula, we estimated the crystalline domain size along the *c'*-direction to be approximately 900 Å. Assuming a cubic shape of the crystallites and a homogenous distribution, the corresponding number of grain boundaries expected to act as primary charge carrier traps is of the order of ~5×10^{14} cm^{-3} which corresponds to a relative trap density of ~5×10^{-7}.

If we attribute the relative trap density to crystal grain boundaries, i.e. $N_t/N_0 = 5\times10^{-7}$, with an energy depth typically in the range of E_t = 100 to 200 meV [28], then the resulting temperature dependence of the hole mobility is given by the green (E_t = 100 meV) and blue (E_t = 200 meV) curves in *figure 7.7*. However, the discrepancy between the data calculated from the H-L model and the experimental TOF mobilities at temperatures below 100K shows that the description of the charge carrier transport by multiple-shallow-trapping and release is not appropriate for holes in DPA. Even variation of the trap density by about two orders of magnitude and of the trap energy by a factor of two will not allow for a suitable fit of the measured $\mu(T)$ dependence in the low temperature regime.

2. Mobility limited by the grain size

An alternative model for the saturated mobility behavior gives forth from the assumption that at sufficiently low temperatures the phonon density and hence the hole-phonon scattering is strongly reduced. As a result, the carrier mean free path might exceed the spatial extension of the crystalline grains and is no longer temperature dependent. However, assuming an effective phonon scattering rate between 10^{11} and 10^{12} s^{-1} [153] and calculating the drift velocity v_d of holes from the transit time of the TOF pulse, which amounts to v_d ~ 400 m/s for temperatures between 5 to 100 K and at an electric field of ~

10^4 V/cm, we estimate the mean free path to be 5 to 50 Å which is shorter by at least one order of magnitude compared to the estimated average grain size of 900 Å. Therefore this model is also unable to explain the experimental mobility behavior.

3. Band-width limited mobility

The third model describes the charge carrier transport in terms of a band-like picture assuming sufficient inter-molecular overlap, at least at low temperatures, with delocalization of the charge carriers exceeding on an average an individual lattice site. In the simplest case, i.e. starting from a cosine-shaped band description, the drift velocity and, therefore, the mobility reaches saturation at low temperatures due to the finite bandwidth. As discussed in Chapter 2, at high electric fields, the drift velocity saturates and can be described by

$$v_{sat} = \frac{0.72Wd}{\pi\hbar} \qquad 7.2$$

which, vice versa allows for an estimation of the bandwidth W, in case of holes that of the valence band, knowing the spatial periodicity d of the potential in which the charge carrier waves propagate. It is important to note, that we assumed the spacing between subsequent phenyl-phenyl links of neighboring DPA molecules to define the effective spatial periodicity along the transport direction, i.e. d = 6.15 Å, which is half the lattice spacing along the *c'*-axis (*figure 7.1*). The bandwidth calculated using *equation 2.11* for DPA along the *c'*-direction is approximately 2 meV and is mainly determined by the small π-systems of the adjacent phenyl-rings. This bandwidth is narrower than that of naphthalene (W = 40 meV), the latter however estimated from the TOF mobilities along the crystallographic *a*-direction of higher inter-molecular overlap [29]. The bandwidth extracted from the experimental data on ultra-pure DPA samples at low temperatures turned out to be much smaller than that predicted from theory and also to be smaller than the thermal energy at 100 K (~ 10 meV) indicating that this model is also not adequate to explain the mobility behavior.

The discussed band-picture for the transport in DPA is a very simplistic approach since the small crystallite size (~ 900 Å) in conjunction with the grain boundaries might play a more complex role in the electronic conduction mechanisms. Furthermore, the thermal energy in the measured temperature range exceeds the calculated valence band-width and therefore, indicates the need of a more extended transport model, including contributions of scattering by low frequency modes, e.g. librations of the molecules which are not frozen off even below 100 K and might still affect the charge carrier transport.

Another possible explanation of the temperature independent hole mobility in the range of 5 to 100 K could be the balance between band-like and hopping transport resulting in a $\sim T^{0}$ dependence. This kind of weak temperature dependence was previously observed in various organic crystals, e.g. for the electron mobility in anthracne [32], and the hole mobility in perylene [33]. However, an exact explanation of the temperature independent mobilities of charge carriers in such high purity organic crystals is still an open question.

7.2.2 TOF on sublimation grown DPA crystals

TOF measurement were performed on sublimation grown DPA crystals with lateral dimensions in the order of ~ 5 mm^2 and the thickness varying between 50 – 100 µm. *Figure 7.8 (a)* shows electron and hole TOF signals observed in sublimation grown DPA crystals. TOF signals for both electrons and holes exhibit a well-defined transit kink unlike in the case of Bridgman grown crystals where the TOF signal for electrons are blurred over most of the temperature range. The room temperature mobility for holes amounts to $\mu_h(RT)$ = 6.6 cm^2/Vs and for electrons to $\mu_e(RT)$ = 4.8 cm^2/Vs.

Interestingly, the room temperature hole mobility measured in sublimation grown DPA crystals along the *b*-direction is higher than that in Bridgman grown DPA crystals (~ 3.7 cm^2/Vs along the *c'*-direction) even though the lattice spacing of ~ 20.4 Å along the *b*-direction in which the transport takes place is much larger in sublimation grown DPA crystals (~12.3 Å along the *c'*-direction in Bridgman grown crystals). Furthermore, the nearest *C-C* contact distance between two phenyl groups of adjacent molecules along the *b*-direction in sublimation grown crystals is ~ 4.9 Å whereas in Bridgman crystals along the *c'*-direction this value is more than 20% shorter (3.8 Å). This excludes an effect due

to the phenyl groups' overlap because Bridgman grown crystals are more likely to have a better overlap compared to the sublimation grown crystals. Therefore the high experimental mobility could be explained by the crystal quality or by different transport mechanisms.

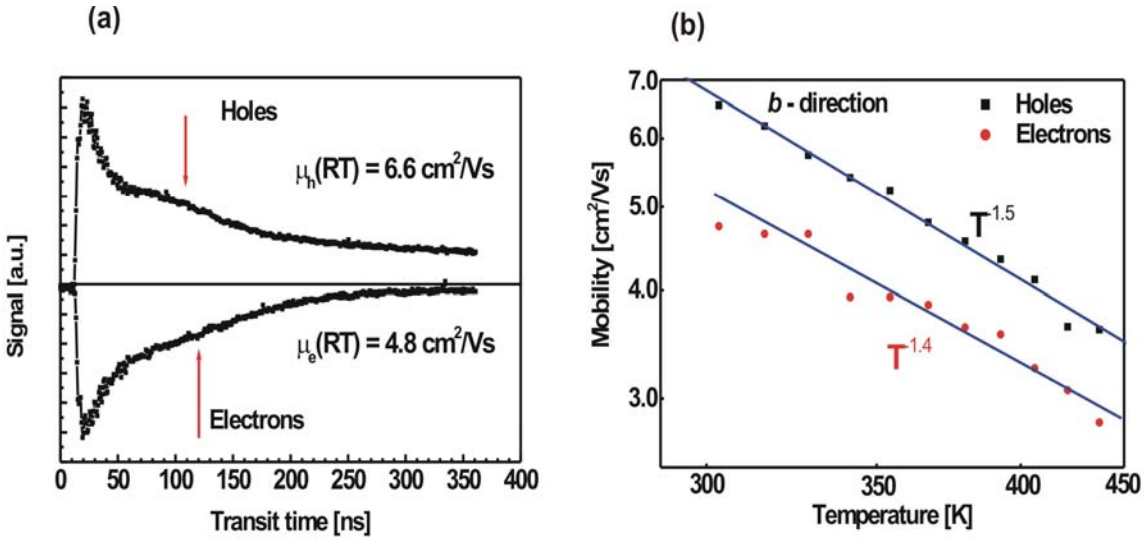

Figure 7.8 (a) *Electron and hole transit signals in sublimation grown DPA crystals. Red arrows indicate the position of the transit kinks.* ***(b)*** *Electron and hole mobilities along the b-direction in sublimation grown DPA crystal. Blue lines represent the T^{-n} dependence.*

As we have already seen, the intensity of Bragg peaks as well as the crystallite size calculated from the width of the peak is much larger in sublimation grown DPA crystals (~ 1600 Å) compared to that in the Bridgman grown crystals (~ 900 Å). The structural quality of the sublimation grown crystals thereby exceeds that of the Bridgman grown crystals. During condensation in the streaming gas reactor, less restrictions are imposed on the DPA crystal, for instance by the glass walls, as in case of melt-grown crystals, resulting in a reduced density of defects such as e.g. dislocation lines. This would be in accordance with previous data reported for anthracene showing a reduction of dislocation lines by two orders of magnitude in comparison with Bridgman grown samples [103]. We tried to estimate the dislocation lines by etching measurements. However, Oleum (also knows as *fuming sulfuric acid*: $H_2SO_4.SO_3$) did not turn out to be a good etchant for DPA

and no etch pits were found even after exposing the DPA crystal surfaces for more than 10 minutes in the acid. Therefore, under the assumption that the transport is limited by the grain boundaries, sublimation-grown crystals are likely to exhibit higher mobility compared to the Bridgman grown crystals.

T-dependent mobility in sublimation grown DPA crystals

To study differences in the underlying transport mechanisms, the mobility was measured as a function of temperature as plotted in *figure 7.8 (b)* for both electrons and holes in the temperature range of 300 – 440 K. Remarkably, electron as well as hole mobility follow the similar temperature dependence of $\sim T^{-n}$ with n = 1.4 and 1.5 respectively. As analyzed on conventional inorganic semiconductors such as silicon the $\mu \sim T^{-1.5}$ dependence indicates the preferential scattering of charge carriers by acoustic phonons in a wide-band transport model [62].

As reported earlier, temperature dependence of the hole mobility in Bridgman grown crystals exhibit a $\sim T^{-2.3}$ dependence which can be related to scattering by optical as well as acoustic phonons [63]. This different scattering mechanism and hence the weaker temperature dependence of the hole mobility in sublimation grown crystals would provide an additional reason for the higher hole mobility in these crystals besides the better long range order of the molecules.

TOF measurements at low temperatures would provide further important information on the transport mechanism but unfortunately we could not observe distinguishable TOF pulses at low temperatures due to the poor signal to noise ratio at temperatures below 300 K, possibly due to the reduced thermal release of charge carriers from the shallow traps. Increasing external electric field would enable to observe the transit kink due to the enhanced drift velocity of charge carriers but the limitations imposed by the crystal thickness result in the dielectric breakdown, and cause an irreversible damage to the crystal. Measurements on thicker crystals would allow higher external fields, but as mentioned in Chapter 3, growth from the sublimation technique does not provide much leverage to tune the crystal thickness which in our case did not exceed 100 μm for good quality crystals.

7.2.3 J-V measurements on sublimation grown DPA crystals

We have seen that observation of balanced transport of electrons and holes with high mobilities indicate the potential of DPA to be used as a model system to study the ambipolar transport, also with respect to organic electronic devices. However, injection of charge carriers into the organic transport layers remains a major challenge for the realization of electronic devices, despite the fact that DPA shows good intrinsic transport of electrons and holes. In order to check the feasibility of DPA crystals we examined the *J-V* characteristics of crystals sandwiched between metal electrodes of evaporated silver. *Figure 7.9 (a)* shows the *J-V* characteristics measured at different temperatures in the range of 298 K to 433 K on a ~ 100 μm thick crystal.

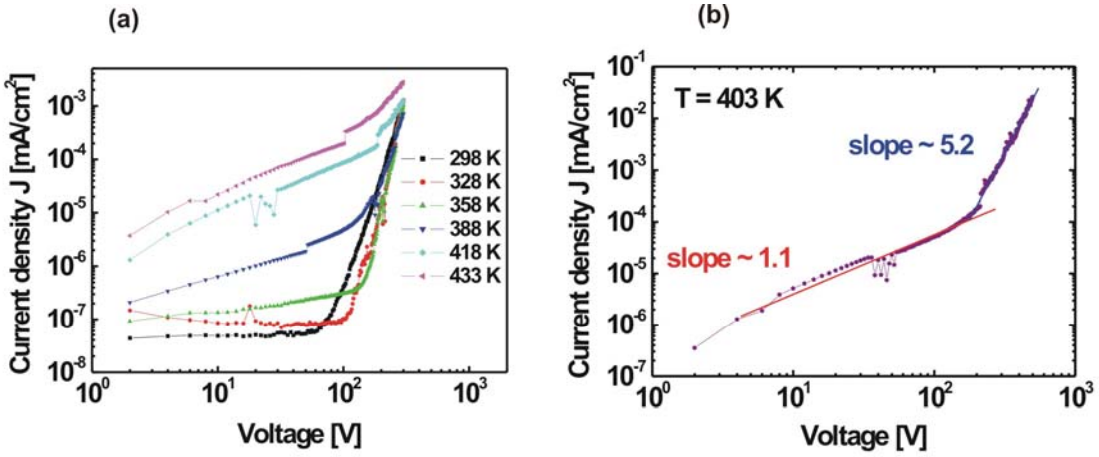

Figure 7.9 (a) *Representative I-V characteristics in DPA crystal measured at various temperatures and* ***(b)*** *I-V characteristic at 403 K on DPA crystal indicating the Ohmic and the trap filling regime.*

As can be seen, we observe a poor injection of charge carriers at room temperature and up to temperatures as high as 358 K, and the current flowing through the crystals is in mere pico-ampere range for an applied voltage of up to 100 Volts, i.e. electric fields up to 10^4 V/cm. Further increase in the applied voltage results in slightly better injection, though still insufficient to realize a good field effect transport.

Figure 7.9 (b) shows a *J-V* curve at 403 K. Initially we observe a linear increase of the current with the increasing voltages followed by steep increase in the current upon increasing the voltage above 200 Volts. The current follows a power law dependence on the applied voltage with $J \sim V^{-5.2}$, this regime of *J-V* characteristic is identified as trap-filling regime in the SCLC theory. However, the trap filled SCLC regime ($J \sim V^{2}$) could not be reached even up to voltages as high as 500 V. Further increase in the applied voltages causes dielectric breakdown of the sample.

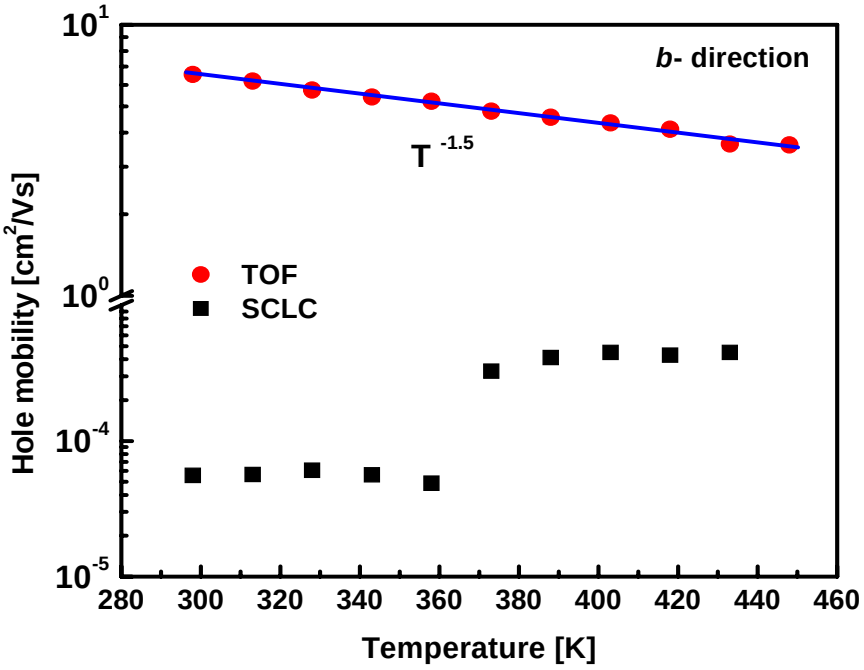

Figure 7.10 *Hole mobilities along the crystallographic b-direction in sublimation grown DPA crystals as a function of temperature estimated from TOF measurements (red circles) and from J-V characteristics (black squares).*

In order to compare injection dependent transport with that of TOF measurements, we estimated a lower limit of the hole mobility from the *J-V* characteristics using the *equation 6.1*. *Figure 7.10* shows the temperature dependent hole mobilities along the crystallographic *b*- direction estimated from TOF as well as SCLC methods.

Poor charge carrier injection, as depicted from *figures 7.9 and 7.10* indicates that standard metal electrodes are not suited for the realization of FETs based on DPA single crystals. Metals such as *Ag*, *Au* etc. can not be used to inject charge carriers into the crystals, due to the large injection barrier formed at the metal-organic interface because of the mismatch between the metal Fermi level and HOMO /LUMO levels of DPA crystal. We could not find any experimental values for HOMO and LUMO levels of DPA in literature. However, assuming that it has almost similar values to that in anthracene, which amounts to ~ 5.8 eV for the HOMO with respect to the vacuum level [154] or as in 9-10-dichloroanthracene, which also has HOMO level at ~ 5.8 eV with respect to vacuum [155], the hole injection barrier at *Ag*-DPA interface would amount to ~ 1.3 eV, which is too large for good injection. Apart from the mismatch between electronic levels, interface dipoles can further enhance or reduce the injection barriers by up to 1 eV.

An alternative would be to use conducting polymers as electrodes. A major advantage that conducting polymers provide is their work function which can be tuned, e.g. by doping [156] or by electrochemical treatments [157]. It has been reported recently that the conducting polymer poly(3,4-ethylenedioxythiophene)/poly(styrenesulfonate) (PEDT:PSS) can have the work function as high as 5.65 eV in vacuum.[158]. Therefore use of PEDT:PSS instead of *Ag* should result in much better hole injection into DPA. However, so far the application of conducting polymer electrodes is limited to polymers and thin films only, as it is a tedious task to apply them on organic crystals in a controlled fashion.

7.3 Conclusions

TOF measurements were performed on both sublimation grown and Bridgman grown DPA crystals. Bridgman grown crystals exhibited hole mobilities over a wide temperature range of 5 K – 420 K, enabling us to investigate the temperature dependent transport mechanism for holes in these crystals. However, TOF signals corresponding to electrons were non-distinguishable for most of the temperatures.

Room temperature mobility for holes of ~ 3.8 cm^2/Vs and for electrons of ~ 13 cm^2/Vs were estimated from the respective TOF signals. The temperature dependent hole

mobility exhibits a band-like transport accompanied by scattering by acoustic and optical phonons in the temperature range between 100 K – 420 K. For temperatures below 100 K, the hole mobility shows a trend of saturation. A preliminary estimation from the saturation regime of TOF mobility results in a band-width of ~ 2 meV. The band-width extracted from the experimental data on ultra-pure samples at low temperatures turned out to be much smaller than the thermal energy at 100 K (~ 10 meV) and therefore indicate a rather limited description of the temperature dependent transport by a band-like approach. A more sophisticated model is needed to theoretically describe the transport phenomenon in these crystals.

Unlike in Bridgman grown crystals, sublimation grown DPA crystals exhibit both electron and hole mobilities over the temperature range of 300 K – 440 K. A room temperature mobility for holes of $\mu_h(RT)$ = 6.6 cm^2/Vs and for electrons of $\mu_e(RT)$ = 4.8 cm^2/Vs were observed. Both electrons and holes indicate band-like transport with scattering by acoustic phonons. Balanced electron and hole transport in sublimation grown DPA crystals indicate the potential of this material to be used for organic ambipolar electronic devices. However, *J-V* measurements show that injection of charge carriers into the DPA crystals is rather poor, mainly due to the mismatch between metal Fermi level and the respective transport levels of DPA.

8 Summary and Outlook

In this thesis, we performed the structural and electronic characterization of single crystals of Diindenoperylene (DIP) and 9,10-Diphenylanthracene (DPA). Both compounds exhibit very good chemical stability, as deduced by the UV-Vis spectroscopy. DIP shows no degradation, even upon the long-term (> 72 hrs.) exposure to the UV light. DPA also shows strong chemical stability and decays at a much slower rate of 0.006 h^{-1} compared to various other PAHs, e.g. rubrene, pentacene, tetracene, and anthracene.

Single crystals were grown by sublimation growth (DIP and DPA) and Bridgman growth (DPA) methods. For the first time, a complete structural characterization using temperature dependent X-ray, and single crystal diffractometry was performed on these crystals. Different polymorphs in these crystals were analytically characterized and the corresponding crystal structures were obtained.

Furthermore, in order to investigate the correlation between structural and electronic properties, temperature dependent TOF, SCLC and FET measurements were performed on these crystals. Effects of bulk traps, crystallite size, metal-organic interface traps and insulator-semiconductor interface traps on the temperature dependent mobility were discussed in the framework of different transport models.

DIP crystals: Enantiotropic polymorphism

Sublimation grown DIP crystals undergo an enantiotropic phase transition from the *α-phase* (*Low-T* phase) to the *β- phase* (*High-T* phase) at 403 K (T_c). In the *α-phase* (T < 403 K), DIP crystallizes into a triclinic structure with lattice constants of a = 11.58 Å, b = 12.96 Å, c = 14.88 Å, α = 98.14°, β = 98.10°, γ = 114.53°, space group $P\bar{1}$ and a unit cell volume of V = 1963.0 $Å^3$ at 298 K whereas *β-phase* (T > 403 K) forms a monoclinic

structure at temperatures with lattice constants of a = 7.17 Å, b = 8.55 Å, c = 16.80 Å, β = 92.42°, space group $P2_1/a$ and a unit cell volume of V = 1028.9 Å^3 at 423 K. The occurring *β- phase* is the same as the thin film phase of DIP on weakly interacting substrates, such as SiO_2.

The crystallite sizes calculated from the width of Bragg peaks vary between 900 Å and 2400 Å depending on the quality of the crystals. X-ray diffraction measurements indicate that the phase transition is accompanied by an intermediate phase, which eventually merges into the *β- phase* upon completion of the phase transition. This intermediate phase evolves at around 370 K (T_{ph}) and corresponds to the on-set of the phase transition. Also, the phase transition temperature for capped crystals of DIP shifts to higher values and does not complete up to at least 405 K. This shift could be attributed to the clamping of the interfacial DIP layers due to the strong metal organic interaction at the interface and hence hindering the phase transition. Another possibility for the shift of the phase transition temperature is that metal diffuses into the organic layers at elevated temperatures and the formed metal clusters sterically hinder the molecular rearrangement. Single crystal diffractometry provides the details of the crystal structure and the phase transition and indicates a first order enantitropic phase transition. Lattice parameters, librations and translations show a discontinuity at T_c, a characteristic of first order phase transitions. The phase transition from the low-symmetry triclinic *α-phase* to the high symmetry monoclinic *β-phase* involves a halving of the unit cell along with a strong shearing of the lattice which results in stress fields in the crystals, often causing a fracturing of the crystals during temperature dependent measurements.

The enthalpy of the phase transition calculated from DSC spectra amounts to ΔH =1.0 ± 0.2 kJ/mol which converts to an entropy change of ΔS = 2.4 ± 0.5 J/(mol K). These values are in good agreement with the theoretical calculations of the entropy ΔS = 2.88 J/(mol K) due to the symmetry change.

DPA crystals: Monotropic polymorphs

DPA crystals grown from the melt (Bridgman growth) and from the vapor (sublimation growth) were structurally analyzed. We have observed that the crystal structure delicately

depends on the route of preparation. The Bridgman grown crystals form a monoclinic structure with lattice parameters : a = 10.7 Å, b = 13.6 Å, c = 12.3 Å, β = 90.5º, similar to the values obtained for solution grown DPA crystals. However, sublimation grown DPA crystals exhibit a completely different molecular arrangement and form a monoclinic crystal structure with unit cell dimensions a = 9.5 Å, b = 20.4 Å, c = 10.1 Å and β = 112.3°. Within the unit cell, the anthracene backbone in sublimation grown DPA crystals is rotated by almost 90° with respect to the anthracene backbone in Bridgman grown DPA crystals. The strong distortion of the molecular rearrangement suggests that DPA has two monotropic polymorphs, which could not be converted into each other by heating or cooling treatments. X-ray diffraction measurements on these crystals show that sublimation grown crystals have a much better quality compared to Bridgman grown crystals. A crystallite size of ~ 1600 Å was estimated in sublimation grown crystals compared to a crystallite size of ~ 900Å in Bridgman grown crystals. Rocking width measurements also suggest a relatively better quality of sublimation grown DPA crystals.

Electronic transport in DIP crystals

Both electron and hole transport is observed in DIP single crystals by the TOF method, reflecting the chemically stable structure of this molecule. The room temperature electron mobility amounts to ~ 0.02 cm^2/Vs and the hole mobility to 0.003 cm^2/Vs. The electron mobility was found to be higher than the hole mobility over the entire temperature range. Both electron and hole mobilities show anomalies around the on-set of the phase transition temperature at ~ 370 K. Temperature dependent TOF measurements reveal that the hole mobility exhibits a thermally activated behavior with an activation energy E_a of ~ 230 ± 20 meV, which could be attributed to energy barriers imposed at grain boundaries due to the translational symmetry breaking and the resulting changes of the local polarization field.

Temperature dependent SCLC and FET measurements are performed over the range of 300 K – 450 K. Only hole transport could be observed in both methods due to the large injection barrier for electrons at the *Ag*-DIP interface. Similar to the TOF measurements, temperature dependent SCLC and FET hole mobilities show anomalies around 370 K,

suggesting the strong correlation between electronic transport and structural phase transition in DIP crystals. In this context, the FET mobility proves to be more sensitive on the phase transition, possibly due to the herringbone structure and the tighter molecular packing of the DIP molecules in the *(ab)*-plane, which result in stronger intermolecular interactions. The room temperature FET hole mobility is ~ 2×10^{-4} cm^2/Vs, which is almost an order of magnitude higher than the SCLC mobility. The SCLC hole mobility shows a thermally activated transport, however, with two different activation energies in different temperature regimes. In the temperature range of 300 K – 360 K, an activation energy of 820 ± 80 meV was estimated, whereas for temperatures above 360 K, the activation energy amounts to 120 ± 20 meV. The two different activation energies could be attributed to the presence of metal-organic interface trap states, which play a dominant role in the low temperature regime. However, at elevated temperatures the effect of metal-organic interface traps is reduced, presumably due to the thermally induced changes resulting in a better injection behavior.
For temperatures above 405 K, i.e. in the *High-T β-phase*, the FET hole mobility in DIP single crystals is comparable to the hole mobility estimated in DIP thin film transistors.

Band-like ambipolar transport in DPA crystals

Bridgman grown DPA crystals exhibited TOF hole mobilities over a wide temperature range of 5 K– 420 K. TOF signals corresponding to electrons were not distinguishable for most of the temperatures, presumably due to the deep trap states for electrons formed by oxidation products, e.g diphenylanthracene endoperoxide. Remarkably high room temperature mobilities of ~ 3.8 cm^2/Vs for holes and of ~ 13 cm^2/Vs for electrons were estimated from the respective TOF signals. The temperature dependent hole mobility exhibits a band like transport, i.e. $\mu(T) \sim T^{-2.3}$, dominated by scattering by optical phonons in the temperature range between 100 K – 420 K. For temperatures below 100 K, the hole mobility saturates and a preliminary estimation from the saturation regime of TOF hole mobility results in a width of the valence band of ~ 2 meV. The respective thermal energy at 100 K exceeds the band-width calculated from the mobility data which indicates the need of a more sophisticate theoretical approach, possibly including effects,

such as that of lower vibrational modes, e.g. molecular librations. Micro-Raman studies being performed on DPA crystals in an ongoing collaboration with Prof. A. Girlando at Parma University, Italy would possibly provide vital information about scattering mechanisms.

Sublimation grown DPA crystals exhibit both electron and hole mobilities over the temperature range of 300 K– 440 K. Room temperature mobilities for holes of $\mu_h(RT)$ = 6.6 cm^2/Vs and for electrons of $\mu_e(RT)$ = 4.8 cm^2/Vs were observed. Both electrons and holes exhibit a *band-like* transport with scattering by acoustic phonons, i.e. $\mu(T) \sim T^{-1.5}$. Balanced electron and hole transport along with high charge carrier mobilities in sublimation grown DPA crystals indicate its potential to be used for organic ambipolar devices. However, the hole mobility extracted from the *J-V* measurements is five orders of magnitude lower than the TOF mobility. It can be concluded that standard metal electrodes are not suited for charge injection into DPA. Conducting polymer electrodes, e.g. of PEDT:PSS might be a better choice compared to *Ag* or *Au*, due to the smaller mismatch between the HOMO level of DPA (~5.8 eV) and the polymer's work function (~5.7 eV) compared to *Ag* or *Au*.

Outlook

Both DIP and DPA exhibit an intrinsic ambipolar transport with balanced electron and hole mobilities in injection-free TOF measurements. This indicates the potential of these compounds for ambipolar device applications. Electronic transport properties (single charge carriers as well as excitonic) of DIP have already been successfully applied in first OPV devices.

DPA in particular is a very interesting compound as it exhibits ambipolar transport with high electron and hole mobilities even at room temperature. However, the charge carrier injection into DPA still remains a hindrance for the realization of FETs based on this compound and further modifications in the metal-organic interface properties, e.g. reducing the injection barrier height by conducting polymers or functionalized metal electrodes, are needed for possible application.

List of Figures

Bibliography

[1] S. M. Sze , in *Physics of Semiconductor Devices* (Wiley, New York, 1981)

[2] Hagen Klauk, Marcus Halik, Ute Zschieschang, Günter Schmid, and Wolfgang Radlik, *J. App. Phys* **92**, 5259(2002)

[3] H. J. Katz_ J. Mater. Chem. **7**, 369 (1997)

[4] Hagen Klauk, Ute Zschieschang, Jens Pflaum, and Marcus Halik, *Nature* **445**, 745 (2007)

[5] D. Berner, H. Houili, W. Leo, and L. Zuppiroli, *Phys. Status Solidi A* **202**, 9 (2005)

[6] P. Peumans, A. Yakimov, S. R. Forrest, *J. App. Phys.* **93**, 3693 (2003)

[7] J. Niemax, PhD thesis, *Universität Stuttgart*, Germany (2005)

[8] A. Vollmer, O.D. Jurchescu, I. Arfaoui, I. Salzmann, T.T.M. Palstra, P. Rudolf, J. Niemax, J. Pflaum, J.P. Rabe, and N. Koch, *Eur. Phys. J.* **E 17**, 349 (2005)

[9] G. Horowitz, *Synth. Metal* **138**, 101(2003)

[10] N. Koch, A. Vollmer, *App. Phys. Lett.* **89**, 162107 (2006)

[11] I. G. Hill and A. Kahn, *J. App. Phys.* **84**, 5583 (1998)

[12] A. Pochettino, *Atti. Reale Accad. Lincei* **1,** 355 (1906),

[13] J. Königsberger and K. Schilling, *Ann. Phys.* **32** , 179 (1910)

[14] M. Volmer, *Ann. Physik* **40**, 775 (1913)

[15] M. Pope, H. P. Kallmann, A. Chen, and P. Gordon, *J. Chem. Phys.* **36**, 2486 (1962)

[16] J. N. Murrell, *Mol. Phys.* **4**, 205 (1961)

[17] L. Friedman, *Phys. Rev.* **133** (6A), 1668 (1964)

[18] G. H. Heilmeier and L. A. Zanoni, *J. Phys. Chem. Solids* **25**, 603 (1964)

[19] M. L. Petrova, L. D. Rozenshtein, *Fiz. Tverd. Tela* **12**, 961 (1970)

[20] J. McGinness, *Science* **183**, 853(1974)

[21] H. Shirakawa, E. J. Louis, A. G. MacDiarmid, C. K. Chiang and A. J. Heeger, *J. Chem. Soc., Chem. Comm.* 578-580 (1977)

[22] Daisuke Kumaki, Masayuki Yahiro, Youji Inoue and Shizuo Tokito, *App. Phys. Lett*. **90**, 133511 (2007)

[23] D. J. Gundlach, J. A. Nichols, L. Zhou, and T. N. Jackson, *Appl. Phys. Lett.* **80**, 2925 (2002)

[24] M. G. Kane, J. Campi, M. S. Hammond, F. P. Cuomo, B. Greening, C. D. Sheraw, J. A. Nichols, D. J. Gundalch, J. R. Huang, C. C. Kuo, L. Jia, H. Klauk, and T. N. Jackson, *IEEE Electron Device Letters* **21**, 534 (2000)

[25] L. Zhou, S. Park, B. Bai, J. Sun, S.-C. Wu, T. N. Jackson, S. Nelson, D. Freeman, and Y. Hong, *IEEE Electron Device Letter* **26**, 640 (2005)

[26] G. H. Gelinck, H. Edzer, A. Huitema, E. van Veenendaal, E. Cantatore, L. Schrijnemakers, J. V. P. H. van der Putten, T. C. T. Geuns, M. Beenhakkers, J. B. Giesbers, B. –H. Huismans, E. J. Meijer, E. M. Benito, F. J. Touwslager, A. W. Marsman, B. J. E. van Rens, and D. M. de Leeuw, *Nature Materials* **3**, 106 (2004)

[27] K. Walzer, B. Maennig, M. Pfeiffer, and K. Leo, *Chem. Rev.* **107**, 1233 (2007)

[28] M. Münch, PhD Thesis, *Universität Stuttgart* (2001)

[29] W. Warta and N. Karl, *Phys. Rev. B* **32**, 1172 (1985)

[30] N. Karl, in *Landolt-Bornstein* (New Series), Group III, Vol. 17, Semiconductor, Subvol. 17i, (Editors: O. Madelung, M. Schulz, H. Weiss), Springer, Berlin-Heidelberg (1985)

[31] T. Dylla, F. Finger, and E. A. Schiff, *Mat. Res. Soc. Symp. Proc.* **808**, A8.10.1 (2004)

[32] N. Karl, and J. Marktanner, *Mol. Cryst. Liq. Cryst.* **355**, 149 (2000)

[33] N. Karl, K. -H. Kraft, J. Marktanner, M. Münch, F. Schatz, R. Stehle, and H. –M. Uhde, *J. Vac. Sci. Technol. A* **17**, 2318 (1999)

[34] V. Podzorov, E. Menard, A. Borissov, V. Kiryukhin, J. A. Rogers and M. E. Gershenson, *Phys. Rev. Lett*. **93**, 086602 (2004)

[35] O. D. Jurchescu, M. Popinciuc, B. J. van Wees, and T. T. M. Palstra, *Adv. Mater.* **19**, 688 (2007)

[36] V. C. Sundar, J. Zaumseil, V. Podzorov, E. Menard, R. L. Willett, T. Someya, M. E. Gershenson, and J. A. Rogers, *Science* **303**, 1644 (2004)

[37] Z. Burshtein, and D. F. Williams, *Phys. Rev.* **B15**, 5769 (1977)

[38] D. Käfer, and G. Witte, *Phys. Chem. Chem. Phys.* **7**, 2850 (2005)

[39] A. Vollmer, O. D. Jurchescu, I. Arfaoui, I. Salzmann, T. T. M. Palstra, P. Rudolf, J. Niemax, J. Pflaum, J. P. Rabe, and N. Koch, *Eur. Phys. J. E* **17**, 349 (2005)

[40] I. Gutman, *Monatchefte für Chemie* **136**, 1055 (2005)

[41] http//:www.orgworld.de

[42] H. E. Katz, Z. Bao, S. J. Gilat, *Acc. Chem. Res.* **34**, 359 (2001)

[43] A. Kekule*, Bulletin de la Societe Chimique de Paris* **3**, 98 (1865)

[44] J. W. Armit, and R. Robinson, *J. Chem. Soc., Trans.* **127**, 1604 (1925)

[45] E. Clar, *The Aromatic Sextet*, Wiley, London (1972)

[46] E. M. Moris, and J. O. Williams, *Mol. Cryst. Liq. Cryst.* **39**, 13 (1977)

[47] J. Niemax, A.K. Tripathi, and J. Pflaum, *Appl. Phys. Lett.* **86**, 122105 (2005)

[48] C. Kittel, in *Introduction to Solid State Physics*, (Wiley, New York, 1963)

[49] W. Warta, PhD Thesis, *Universität Stuttgart* (1985)

[50] J. M. Ziman, *Principles of the Theory of Solids*, *Cambridge U. P., London* (1965)

[51] M. Fischer, M. Dressel, B. Gompf, A. K. Tripathi, and J. Pflaum, *App. Phys. Lett.* **89**, 182103 (2006)

[52] Daniel Faltermeier , PhD Thesis , *Universität Stuttgart* (2007)

[53] K. Hannewald, and P. A. Bobbert, *App. Phys. Lett.* **85**, 1535 (2004)

[54] F. Ortmann, K. Hannewald, and F. Beshstedt, *Phys. Rev. B* **75**, 195219 (2007)

[55] D. C. Singh, and S. C. Mathur, *Mol. Cryst. Liq. Cryst.* **27**, 55 (1974)

[56] V. M. Kenkre, and P. E. Parris, *Phys. Rev. B* **65**, 205104 (2002)

[57] L. B. Schein, *Phys. Rev. B* **15**, 1024 (1977)

[58] H. Frohlich, and S. L. Sewell, *Proc. Phys. Soc. (London)* **74**, 643 (1959)

[59] V. M. Kenkre, *Phys. Lett. A* **305**, 443 (2002)

[60] V. M. Kenkre, P. E. Parris, *Phys. Rev. B* **65**, 245106 (2002)

[61] J. Bardeen, W. Shockley, *Phys. Rev.* **80**, 72 (1950)

[62] W. Shockley, and J. Bardeen, *Phys. Rev.* **77**, 407 (1949)

[63] K. Seeger, *Semiconductor Physics*, 2nd edition (Springer, Berlin, 1982)

[64] L. Friedman, *Phys. Rev.* **140**, A1649 (1965)

[65] H. Frohlich, and S. L. Sewell, *Proc. Phys. Soc. (London)* **74**, 643 (1959)

[66] R. L. Petritz, and W. W. Scanlon, *Phys. Rev.* **97**, 1620 (1955)

[67] E. Conwell, and V. F. Weiskopf, *Phys. Rev.* **77**, 388 (1950)

[68] C. Erginsoy, *Phys. Rev.* **79**, 1013 (1950)

[69] W. T. Reed, *Philos. Mag.* **45**, 775 (1954)

[70] J. –L. Bredas, D. Beljonne, V. Coropceanu, and J. Cornil, *Chem. Rev.* **104**, 4971 (2004)

[71] D. A. da Silva Filho, Eung-Gun Kim, and J.-L. Bredas, *Adv. Mater.* **17**, 1072 (2005)

[72] M. Yamagishi, J. Takeya, Y. Tominari, Y. Nakazawa, T. Kuroda, S. Ikehata, M. Uno, T. Nishikawa, and T. Kawase, *App. Phys. Lett.* **90**, 182117 (2007)

[73] K. Hannewald, V. M. Stojanovic, J. M. T. Schellekens, P. A. Bobbert, G. Kresse, and J. Hafner, *Phys. Rev. B* **69**, 075211 (2004)

[74] A. Troisi, and G. Orlandi, *Phys. Rev. Lett.* **96**, 086601 (2006)

[75] T. Holstein, *Ann. Phys.* **8**, 325 (1959) and *Ann. Phys.* **8**, 343 (1959)

[76] A. Miller, and E. Abrahams, *Phys. Rev.* **120**, 745 (1960)

[77] Arrhenius equation, *IUPAC Compendium of Chemical Tehcnology*, 2nd edition (1997)

[78] V. Kazukauskas, Semicond. *Sci. Technol.* **19** , 1373 (2004)

[79] P. W. M. Blom, M. J. M. de Jong, and M. G. van Munster, *Phys. Rev. B* **55**, R656 (1996)

[80] G. Horowitz, *J. Mater. Chem.* **9**, 2021 (1999)

[81] H. H. Poole, *Philos. Mag.* **32**, 112 (1916)

[82] Frenkel, *J. Phys. Rev.* **54**, 647 (1938)

[83] H. Bässler, *Philos. Mag. B* **50**,347 (1984)

[84] Y. Preezant, Y. Roichman, and N. Tessler, *J. Phys.: Condens. Matter* **14**, 9913 (2002)

[85] I. G. Austin and R. Gamble, in *Conduction in Low Mobility Materials*, Taylor and Francis, London (1971)

[86] I. I. Fishchuk, D. Hertel, H. Bässler, and A. K. Kadashchuk, *Phys. Rev. B.* **65**, 125201 (2002)

[87] D. C. Hoesterey and G. M. Letson, *J. Phys. Chem. Solids* **24**,1609 (1963)

[88] N. Karl, in *Organic Elecrtonic Materials*, Editors: R. Farchioni, and G. Groddo, (Springer, Berlin, 2001)

[89] K. H. Probst , Ph.D. thesis, *Universität Stuttgart* (1974)

[90] K. H. Probst, N. Karl, *Phys. Status Solidi* **a 27**, 499 (1975)

[91] A.C. Duerr, F. Schreiber, M. Münch, N. Karl, B. Krause, V. Kruppa and H. Dosch, *App. Phys. Lett.* **81**, 2276 (2002)

[92] S. Sellner, A. Gerlach, F. Schreiber, M. Kelsch, N. Kasper, H. Dosch, S. Meyer, J. Pflaum, M. Fischer, and B. Gompf, *Adv. Mater.* **16**, 1750 (2004)

[93] S. Sellner, A. Gerlach, F. Schreiber, M. Kelsch, N. Kasper, H. Dosch, S. Meyer, J. Pflaum, M. Fischer, B. Gompf and G. Ulbricht, *J. Mater. Res.*, **21**, 455 (2006)

[94] D. Kurrle, Diplom thesis, *Universität Stuttgart* (2004)

[95] N. Karl, *Synth. Met.* **649**, 133 (2003).

[96] B. G. Huth, and G. I. Farmer, *IEEE J. Quant. Electron* **QE-4**, 427 (1968)

[97] Y.-H. Kim, and S.-K. Kwon, *J. Appl. Polymer Sci.* **100**, 2151 (2006)

[98] W. G. Pfann, *Zone Melting*, Wiley, New York (1958)

[99] N. Karl, in *Crystals, Growth, properties, and Applications*, **Vol. 4**, (Editor: H. C. Freyhardt), Springer, Berlin-Heidelberg (1980)

[100] H. C. Wolf, in *Atomic and Molecular Physics*, **Vol. 3**, Bates and Estermann (eds.) 1967)

[101] P. W. Bridgman, *Proc. Am. Acad. Arts Sci.* **60**, 305 (1925)

[102] J. O. Williams, J. M. Thomas, *Trans. Faraday. Soc.* **63**, 1720 (1967)

[103] P. J. Reucroft, A. R. McGhei, E. E. Hillman, and V. V. Damiano, *J. Cryst. Growth* **11**, 355 (1971)

[104] N. Karl, *Stuttgarter Kristalllabor*, Private communication.

[105] R. A. Laudise, Ch. Kloc, P. G. Simpkins, and T. Siegrist, *J. Cryst. Growth* **187**, 449 (1998)

[106] Jens Als-Nielsen and Des McMorrow, *Elements of Modern X-ray Physics* (John Wiley & Sons, Ltd., ADDRESS, 2000)

[107] Duncan McKie, and Christine McKie, in *Essentials of Crystallography*, (Blackwell Scientific Publications, Oxford, 1986)

[108] B. Cullity, *Elements of X-Ray Diffraction* (Addison Wiley, Reading, MA 1978)

[109] J. R. Hayens and W. Schokley, *Phys. Rev.* **81**, 835 (1951)

[110] R. G. Kepler, *Phys. Rev.* **119**, 1226 (1960)

[111] O. H. LeBlanc, *J. Chem. Phys.* **33**, 626 (1960)

[112] M. Pope and C.E. Swenberg, *Electronic Processes in Organic Crystals and Polymers*, (Oxford University Press, Oxford,1999)

[113] A. Many, M. Simhony, S. Z. Weiss, and J. Lewinson, *J. Phys. Chem. Sol.* **22**, 285 (1961)

[114] A. Many, and P. Rakavy, *Phys. Rev.* **126**, 1980 (1962)

[115] K. C. Kao and K. Hwang, *Electrical Transport in Solids* (Pergamon, New York, 1970)

[116] N. F. Mott and R. W. Gurney, *Electronic Processes in Ionic Crystals* (Oxford University Press, Oxford, 1940)

[117] J. A. Guest, *Phys. Status Solidi* **15**, 107 (1966)

[118] O. D. Jurchescu, J. Baas, and T. T. M. Palstra, *App. Phys. Lett.* **84**, 3061 (2004)

[119] A. Kahn, N. Koch, and W. Y. Gao, *J. Polym. Sci. Part B* **41**, 2529 (2003)

[120] L. Bürgi, T. J. Richards, R. H. Friend, and H. Sirringhaus, *J. App. Phys.* **94**, 6129 (2003)

[121] R. W. I. de Boer, M. E. Gershenson, A. F. Morpurgo, and V. Podzorov, *Phys. Stat. Sol. (a)* **201**, 1302 (2004)

[122] A. L. Briseno, R. J. Tseng, A.-M. Ling, E. H. L. Falcao, Y. Yang, F. Wudl, and Z. Bao, *Adv. Mater.* **18**, 2320 (2006)

[123] E. Menard, V. Podzorov, S.-H. Shur, A. Gaur, M. E. Gershenson, and J. A. Rogers, *Adv. Mater.* **16**, 2097 (2004)

[124] R. W. I. de Boer, PhD Thesis, *Technische Universiteit*, The Netherlands (2005)

[125] M. E. Gershenson, V. Podzorov, A. F. Morpurgo, *Rev. Mod. Phys.* **78**, 973 (2006)

[126] V. Podzorov, V. M. Pudalov, and M. E. Gershenson, *Appl. Phys. Lett.* **82**, 1739 (2003)

[127] L. Libera, and L. Baldauf, in *Wertekatalog dünner Schichten*, (Editors: C. Hamann, M. Starke) Technische Hochschule Karl-Marx-Stadt (1980), 159 -163

[128] T. Siegrist, C. Kloc, J. H. Schön, B. Batlogg, R. C. Haddon, S. Berg, and G. A. Thomas, *Angew. Chem.* **40**, 1732 (2001)

[129] U. Sondermann, A. Kutoglu, and H. Bässler, *J. Phys. Chem.* **89**, 1735 (1985)

[130] F. A. Herbstein, *Acta Crystallogr. B* **62**, 341 (2006)

[131] J. Oddershede, S. Larsen, *J. Phys. Chem. A* **108**, 1057 (2004)

[132] C. P. Brock and J. D. Dunitz, *Acta Crystallogr. B*, **46**, 795 (1990)

[133] S. Haas, C. Kloc, and T. Siegrist, unpublished results

[134] S. Haas, B. Batlogg, C. Besnard, M. Schiltz, C. Kloc, and T. Siegrist, unpublished results

[135] A. C. Dürr , Ph. D. Thesis, *Max-Planck-Institut fur Metallforschung in Stuttgart, Universität Stuttgart* (2002)

[136] A. C. Dürr, F. Schreiber, M. Kelsch, H. D. Carstanjen, H. Dosch, and O. H. Seeck, *J. App. Phys.* **93**, 5201 (2003)

[137] J. Pflaum, J. Niemax, and A. K. Tripathi, *Chem. Phys.* **325**, 152 (2006)

[138] E. Hernandez-Gracia and M. Grant, *J. Phys. A* **25**, L1355 (1992)

[139] A. Girlando, M. Masino, A. Brillante, R. G. D. Valle, E. Venuti, *Materials Science-Poland* **22**, 307 (2004)

[140] F. Ortmann, K. Hannewald, and F. Bechstedt, *Phys. Rev. B* **75**, 195219 (2007)

[141] G. Horowitz, R. Hajlaoui, and P. Delannoy, *J. Phys III* **5**, 355 (1995)

[142] W. A. Schoonveld, J. Wildeman, D. Fichou, P. A. Bobbert, B. J. van Wees, and T. M. Klapwijk, *Nature* **404**, 977 (2000)

[143] R.W.I. de Boer, M. Jochesmsen, T. M. Klapwijk, A. Morpurgo, J. Niemax, A. K. Tripathi, and J. Pflaum, *J. App. Phys.* **95**, 1196 (2004)

[144] A.C. Dürr, N. Koch, M. Kelsch, A. Rühm, J. Ghijsen, R. L. Johnson, J.-J. Pireaux, J. Schwartz, F. Schreiber, H. Dosch, and A. Kahn, *Phys. Rev. B* **68**, 115428 (2003)

[145] M. Grobosch and M. Knupfer, *Adv. Mater.* **19**, 754 (2007)

[146] Shou-Zheng Weng, Chin-Tsou Kuo, and Shune-Long Wu, *Journal of Polymer Research* **10**, 211 (2003)

[147] M. Scharnberg, J. Kanzow, K. Rätzke, R. Adelung, F. Faupel, S. Meyer, and J. Pflaum, *Mater. Res. Soc. Symp. Proc.* **871E**, 16.31.1 (2005)

[148] Th. Lindner, G. Paasch, and S. Scheinert, *J. App. Phys.* **98**, 114506 (2006)

[149] V. Podzorov, E. Menard, A. Borissov, V. Kirukhin, J. A. Rogers, and M. E. Gershenson*, Phys. Rev. Lett.* **93**, 086602 (2004)

[150] J. Zaumseil, K. W. Baldwin, and J. A. Rogers, *J. App. Phys.* **93**, 6117 (2003)

[151] J. M. Adams, and S. Ramdas, *Acta. Cryst. B* **35**, 679 (1979)

[152] R. B. Campbell, J. M. Robertson, and J. Trotter, *Acta. Cryst.* **14**, 705 (1961)

[153] E. A. Sillinsh, *Organic Molecular Crystals*, Springer, Berlin (1980)

[154] R. Williams, and J. Dresner, *J. Chem. Phys.* **46**, 692 (1967)

[155] S. Hino, T. Hirooka, and H. Inokuchi, *Bull. Chem. Soc. Jpn.* **50**, 620 (1977)

[156] M. Gross, D. C. Müller, H.-G. Nothofer, U Scherf, D. Neher, C. Bräuchle, and K. Meerholz, *Nature* **405**, 661 (2000)

[157] A. Petr, F. Zhang, H. Peisert, M. Knupfer, and L. Dunsch, *Chem. Phys. Lett.* **385**, 140 (2004)

[158] N. Koch, A. Vollmer, and A. Elschner, *App. Phys. Lett.* **90**, 043512 (2007)

List of Publications

1. "*Growth and electronic transport in 9,10-diphenylanthracene single crystals- a high mobility ambipolar organic semiconductor"*
A.K. Tripathi, M. Heinrich, T. Siegrist, and J. Pflaum, *Adv. Mater.* **19**, 2097 (2007)

2. "*Effect of Structural Phase Transition on Thermally Activated Time-of-Flight Charge Carrier Mobility and Field Effect Transport in Diindenoperylene Single Crystals"*
A. K. Tripathi and J. Pflaum, *Mater. Res. Symp. Proc.* ***Vol.* 965** (2007)

3. "*Enantiotropic Polymorphism in Di-indenoperylene"*
M. A. Heinrich, J. Pflaum, A. K. Tripathi, W. Fray, M. L. Steigerwald and T. Siegrist, *J. Phys. Chem.* **111**, 18878 (2007)

4. "*Correlation between ambipolar transport and structural phase transition in diindenoperylene single crystals"*
A. K. Tripathi and J. Pflaum, *App. Phys. Lett.* **89**, 082103 (2006)

5. "*Optical properties of pentacene thin films and single crystals"*
D. Faltermeier, B. Gompf, M. Dressel, A. K. Tripathi and J. Pflaum, *Phys. Rev. B* **74**, 125416 (2006)

6. "*Infrared spectroscopy on the charge accumulation layer in rubrene single crystals*"
M. Fischer, M. Dressel, B. Gompf, A. K. Tripathi and J. Pflaum, *App. Phys. Lett.* **89**, 182103 (2006)

7. "*Effect of impurities on electronic transport in organic single crystals*"
J. Pflaum, J. Niemax, and A. K. Tripathi, *Chem. Phys.*, **325**, 152 (2006).

8. "*Comparison of the electronic properties of sublimation- and vapor-Bridgman-grown crystals of tetracene"*
J. Niemax, A.K. Tripathi, and J. Pflaum, *Appl. Phys. Lett.* **86**, 122105 (2005)

9. "*Charge Carrier Mobility Measurements In Tetracene Single Crystals"*
J. Pflaum, J.Niemax, and A.K. Tripathi, *Mater. Res. Soc. Symp. Proc.* **Vol. 871E** (2005)

10. "*Ellipsometric investigations on the light induced effects on tris(8-hydroxyquinoline) aluminum (Alq3)*"
Satyendra Kumar, Vivek Shukla and Ashutosh Tripathi, *Thin solid films* **477**, 240 (2005)

11. "*Space charge limited transport and time of flight measurements in tetracene single crystals: a comparative study*"
R.W.I. de Boer, M. Jochemsen, T.M. Klapwijk, A.F. Morpurgo, J. Niemax, A. K. Tripathi, and J. Pflaum, *J. Appl. Phys.* **95**, 1196 (2004)

Ackowledgement

Finally, at the completion of my Ph.D. thesis I am obliged to acknowledge the scientific, technical and moral support provided by colleagues, friends, and family, without which it would have been impossible to conclude this work

First of all I would like to thank my supervisor, Prof. Dr. J. Wrachtrup, for allowing me to do my research in the university and also for occasional but useful scientific and non-scientific discussions.

I would like to thanks Prof. Dr. H. Dosch for finding time from his busy schedule to co-supervising my thesis.

My gratitudes towards Prof. Dr. Norbert Karl who first invited me to work as a student researcher in his world famous organic single crystal research group.

My special thanks to Jens (Dr. J. Pflaum), the leaders of Organic Semiconductor group at our institute, for providing useful scientific and analytical input and also for a constant motivation through out this research work. The informal atmosphere, freedom to imply ideas, and helping with the experiments is highly appreciated.

I would like to thank my colleagues: Stephan Meyer, Tobias Roller, Maximilian Nothaft, Jens Niemax, Peter Nill, Rainer Stöhr, Bernhard Grotz, Dieter Kurrle, Philip Neumann, Tobias Schuon, Christoph Arndt, Gopalkrishnan Balasubhramanian and Dr. F. Jelezko for scientific discussions and also for providing a friendly atmosphere to work with.

Our technicians from Crystal Lab: Mr. S. Hirschmann and Mr. C. M. Herb are acknowledged from their technical assistance. Special thanks to Mr. Hirschmann for his expertise in material purification, Bridgman growth and for his help in the DSC and X-ray measurements.

I am thankful to Dr. T. Siegrist and M. Heinrich (Alcatel-Lucent Technologies) for the scientific collaboration and single crystal diffractometry measurements.

I would also like to thank M. Fischer (1. Physikalisches Institut, Uni. Stuttgart) and G. Ulbricht (Max-Planck Institute, Stuttgart) for useful scientific discussions.

Employees of mechanical workshop, glass technique, and photo lab are acknowledged for their technical assistance.

Last but not least, I thank my parents and brothers for the never-ending moral support and encouragement they provided whenever I needed it. I also thank my friends in India, Germany and elsewhere in the world for their optimism about my work and also for a nice off-work atmosphere.

It is very likely that I have missed certain names, which deserved to be acknowledged here. I am thankful to all of them.